MASTER

Nonlinear JOREK simulations of the Greenwald density limit with a thermo-resistive radiation model

van Overveld, Timo J.J.M.

Award date:
2019

Eindhoven University of Technology
Department of Applied Physics

Applied Physics
&
Science and Technology of Nuclear Fusion

Nonlinear JOREK simulations of the Greenwald density limit with a thermo-resistive radiation model

Timo Jacobus Johannes Maria van Overveld
0851456

Supervisors:
prof. dr. ir. Guido Huijsmans
dr. ir. Leon Kamp
ir. Daan van Vugt

Eindhoven, July 2019

Abstract

High densities in fusion plasmas are beneficial for increasing power production, but are restricted by the Greenwald density limit. Exceeding the limit triggers a thermal quench leading to disruptions. This empirical limit is found in all tokamak experiments and shows only dependence on the total current and poloidal plasma area. Scientific consensus has not been reached on the underlying physical mechanism nor on the formulation.

In this thesis, the enhanced magnetic island growth due to net cooling by impurity radiation is investigated as responsible mechanism of triggering density limit disruptions. Using MHD simulations of the fully nonlinear, finite elements code `JOREK`, the evolution of the tearing mode and island growth is studied for varying electron densities, temperatures, impurity fractions and types.

A distinct transition is observed in the tearing mode evolution when the electron density exceeds a critical value. The $2/1$-islands grow to normalized widths of 0.2-0.5 within a few milliseconds when radiative cooling dominates the Ohmic heating inside. Magnetic field lines show ergodic behavior as the temperature profile collapses. The transition is found to be strongly dependent on electron temperature, impurity density and impurity type and is thus incompatible with the Greenwald density limit.

An analytical stability boundary is derived from a local heat balance and shown to predict the island cooling and enhanced nonlinear growth. For specific impurity mixtures, the temperature dependence is absent for an order of magnitude. Moreover, the dependence on the impurity fraction is weak for sufficiently large values. Under these circumstances a direct formulation of the global limit is found in terms of local electron and current densities. Localized heating around and inside the $2/1$-islands suppresses island growth, while for central heating this effect is less efficient.

Using the Furth-Rutherford-Selberg equilibria profiles, the radial locations where local electron density and current density match their globally averaged values are calculated. Their distance to the $q = 2$ surface is smaller than a typical island width for a range of profile shapes and different devices. In combination with the weak dependencies in the local power balance, a full explanation of the formulation of the Greenwald density limit is proposed.

Two possibilities for exceeding the limit are suggested: additional heating around the $q = 2$ surface and the removal of specific impurity species, even at the cost of higher fractions of other species. Recommendations for future studies include full disruption simulations using increased toroidal resolution and verification of the proposed explanation using experimental reviews of physics parameters around magnetic islands in combination with present impurity fractions.

Table of Contents

1. Introduction

1.1 The need for fusion energy

Ever since the formation of the first stars, the nuclear fusion reaction has provided them with the energy to let them burn fiercely. Our own sun forms no exception and it is thanks its power that life could emerge and flourish on earth. The human race is one of the flourishing species on the earth's surface with a rapidly increasing population during the last centuries. This growth will continue in the coming decades with expected world populations of more than 10 billion people [1]. With the ongoing population growth the demand for energy increases, as every individual person has an energy footprint dependent on their standard of living. As developing countries constantly get access to new (technological) advancements, the average energy usage per person increases as it stimulates and is correlated with economic growth [2, 3].

At present, the majority of the consumed energy is still generated by fossil fuels, see figure 1.1. At the predicted usage rate, estimates are that all of them will get significantly depleted, while oil and gas may even run out completely before the turn of the next century [4]. With the burning of fossil fuels, a tremendous amount of greenhouse gasses is emitted, of which CO_2 is the most prevailing and well-known [5]. These gasses are the most important contributors to global warming and the resulting increase in severity and frequency of climatological disasters such as increases of droughts, floods, ocean acidification and tropical storms. The consequences form a direct danger to both man and nature, and affect public health by negatively impacting ecosystems and food supplies [6, 7].

In order to tackle these phenomena, the political leaders of 195 countries signed an agreement in 2015 which is commonly known as the Paris agreement [9]. One of its points sets an upper bound of $2\,^{\circ}\mathrm{C}$ on the average global temperature rise. Another point restricts the emission of greenhouse gasses with the goal of having no net emissions in the second half of this century [10]. Global energy production should be emission neutral by this time. The achievement of these goals proves to be challenging: it requires a transformation in our energy consumption and production. The energy mix will have to undergo a transition from fossil fuel to alternative sources, preferably renewable. The list of sources that will be able to significantly contribute in this century is limited to those that are currently already available. This is based on historical data for energy sources, in which any new energy source will first have to go through a development time, which typically last several decades before it can start to built up a contributing capacity [11]. The eligible group includes (photo-voltaic) solar, wind, hydropower, tidal and nuclear fission sources.

As can be seen form figure 1.1, solar and wind energy have started to make a significant contribution to the global consumption only since the beginning of this decade. While this is a positive development, these sources are most likely not sufficient to replace all fossil sources. One reason is their relatively low power density, resulting in large land or sea area usage. Besides this, their output is inherently fluctuating with the day-night cycle, seasons and local weather conditions. The times at which the most power is generated are generally not coinciding with the times of most consumption. To remedy this issue, enormous storage capacities should be build alongside the production units. Constructing such large batteries is costly, requires many resources and the technology is not at this readiness level yet. It is in fact more beneficial to include a dense energy source in the mix, which can provide a steady baseline regardless of external conditions [12].

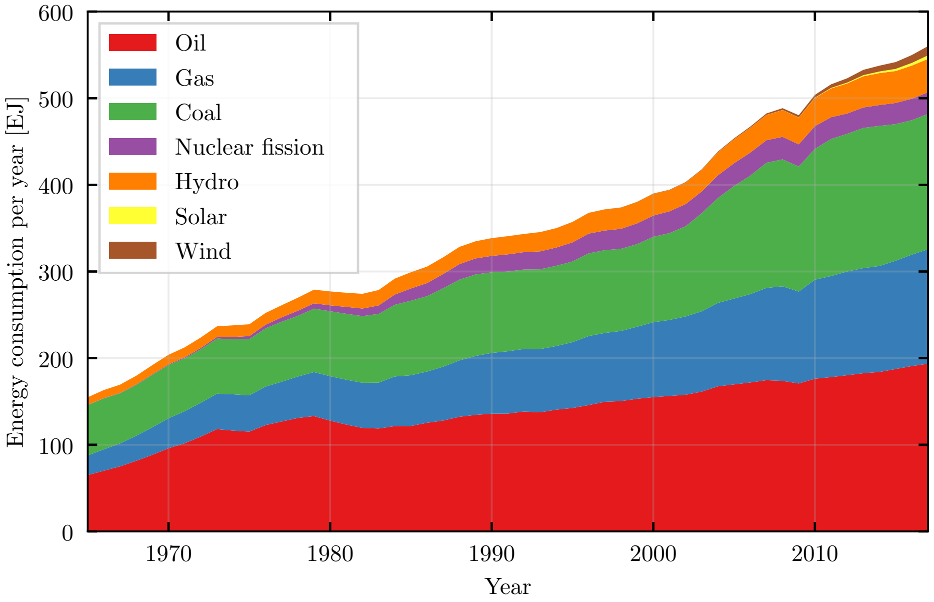

Figure 1.1: The majority of the total energy consumption during the past 50 years originates from a handful of energy sources, with the largest contribution coming from fossil fuels. Renewable sources such as solar and wind are just starting to make a significant contribution [8].

In the first decades of the energy transition, fossil fuel plants can be replaced by fission plants to provide this base production level. However, nuclear fission has a bad public image regarding reactor safety with several disasters in the past causing regions to become inhabitable. Then there is the production of long-lived radioactive waste, for which no definite processing method exists (yet). Lastly, the current generation reactors rely on uranium as a fuel source. While there is still plenty of it, there is a limited amount available on earth.

Now consider a power plant driven by nuclear fusion. Reactors powered by it would be similar in size and power output to present-day coal or nuclear fission plants, which is beneficial for the energy-mix. The fuel for the fusion reactor is available in virtually limitless amounts, as it is partly retrieved from seawater (deuterium) and partly created in the reactor itself (tritium). The reaction-products are not long-lived radioactive species as in the case of fission, but is harmless helium gas. On the other hand, the reactor vessel will become radioactive through neutron irradiation, but effort is put into the development of materials that can tackle this, such as EUROFER [13]. Lastly, the fusion reactor has no risk to have a meltdown, as only limited amounts of fuel will be inside the reactor at a time and requiring tight control to keep the reaction going. The main issue for fusion reactors is that it is not available yet. The first reactor with a net energy output is currently being built as an international collaboration in France, under the name ITER. Its construction should be a proof of concept as well as a way to detect and solve yet unencountered problems.

Now that the economical and environmental needs to switch to reliable energy sources are discussed, the focus can be shifted to a different aspect. Creating a working fusion reactor is one of the greatest technological challenges mankind has encountered, but not yet overcome. It kindles mankind's curiosity to what is technologically possible by trying to capture energy from one of nature's most potent sources. The present-day fusion reactors are regarded as some of the most complex devices in the world. Similar to many other technological challenges in the past decades, the development of a new technology boosts our scientific understanding and show what we as a species are capable of.

1.2 Fusion, how does it work?

In principle, the term *fusion reaction* may refer to any reaction in which multiple atomic nuclei are combined into larger, heavier ones. Differences in nuclear binding energy result in energy getting released in the form of kinetic energy, for reaction products with atomic number smaller or equal to iron. A fusion reaction can occur when two nuclei can come sufficiently close together, after overcoming the Coulomb barrier with which they repel each other. Once their spatial distance is sufficiently small, the merging of the atomic cores occurs under influence of the strong interaction, which is the dominant attractive force at sub-atomic length scales. In practice this close proximity can be reached if the particles have a sufficiently high velocity relative to each other. For a collection of particles a high velocity relates directly to the temperature. So heating a gas will result in a higher average particle velocity, while also causing ionization of the gas, such that a mixture of atomic nuclei and free electrons is created: a plasma.

The probability that a reaction will occur is characterized by the reaction rate (or velocity averaged cross section), derived from the cross section. It is highly temperature-dependent function, as can be seen in figure 1.2. This figure provides information on the most beneficial fusion reaction and its optimal temperature regime. For a fusion reactor on earth, a reaction with the highest possible rate at the lowest temperature is desirable. The reaction between the hydrogen isotopes deuterium and tritium satisfies this requirement, so is considered as the primary option for generating fusion energy on earth.

In the deuterium-tritium (D-T) reaction a helium nucleus and a neutron are formed, according to

$$\mathrm{D}^+ + \mathrm{T}^+ \longrightarrow \mathrm{He}^+ + \mathrm{n} + 17.6\ \mathrm{MeV},$$

which is shown schematically in figure 1.3. Per fusion reaction an energy of $E_{\mathrm{fusion}} = 17.6\,\mathrm{MeV}^1$ is released, which is distributed over the products according to their mass ratio. If a plasma with equal amounts of deuterium and tritium is considered, charge neutrality gives $n_{\mathrm{D}} = n_{\mathrm{T}} = \frac{1}{2}n_{\mathrm{e}}$ with n_e the electron density. The total fusion power density is then given by

$$P_{\mathrm{fusion}} = E_{\mathrm{fusion}} \left\langle \sigma v \right\rangle n_{\mathrm{D}} n_{\mathrm{T}} = \frac{1}{4} E_{\mathrm{fusion}} \left\langle \sigma v \right\rangle n_{\mathrm{e}}^2., \tag{1.1}$$

in which $\langle \sigma v \rangle$ is the velocity averaged cross section, as in figure 1.2 [16].

Now that the physics of fusion at the atomic scale are introduced, we can zoom out to the macroscopic scale: the device or reactor in which the process can be realized and energy harvested. Although there are many concepts and designs available, this thesis focuses on one of the most conventional confinement methods and designs: the tokamak, which uses magnetic fields in a torus-like configuration.

---

[1] $1\mathrm{eV} \approx 1.602 \cdot 10^{-19}\mathrm{J}$

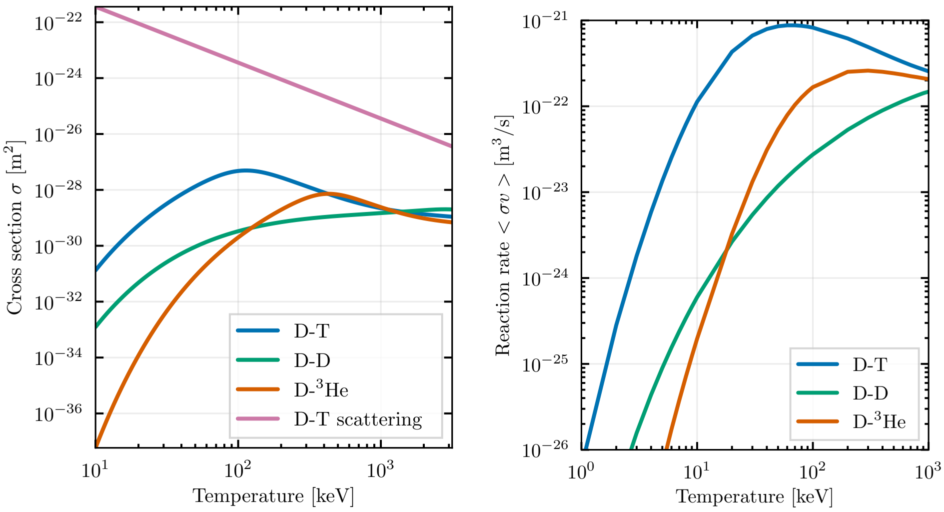

Figure 1.2: The reaction rate for different fusion reactions (right) can be derived from the cross sections (left) as a velocity averaged cross section $\langle \sigma v \rangle$, here given as a function of temperature. At too low temperatures particles will not have sufficient energy to overcome the Coulomb barrier, while at high temperatures the particles' high velocities will decrease their interaction time and thereby the fusion rate. The scattering cross section (collision angle = 5°) exceeds the fusion cross sections by several order of magnitude. Data is obtained from [14] and [15].

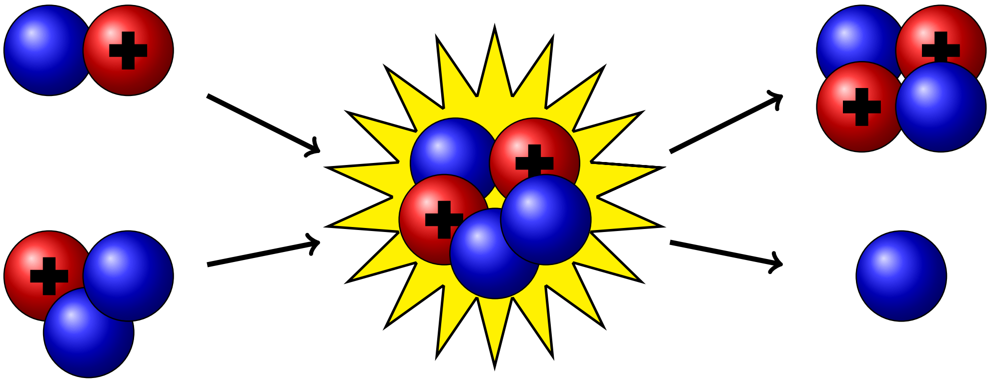

Figure 1.3: A schematic representation of the atomic nuclei (protons in red, neutrons in blue) involved in the deuterium-tritium fusion reaction. When the two nuclei fuse, a helium nucleus and a free neutron are formed.

1.3 The tokamak

Looking back to figure 1.2, it can be seen that the D-T elastic scattering cross section exceeds the fusion cross section for the whole temperature range. So for every successful reaction, there are multiple failed (scattered) in which the energy would be lost. Luckily this does not have to be a showstopper if there is a way to confine the particles and their energy inside a closed system. In this way they can undergo multiple elastic scattering events before fusion occurs. This is possible with magnetic confinement: large magnetic fields that trap the charged plasma particles in a gyrating motion around its field lines.

Because the magnetic field is divergence free, written as $\nabla \cdot \mathbf{B} = 0$, no magnetic sources or sinks can exist. As a consequence, magnetic field lines have no start or end points [17]. One method of keeping both the magnetic field and the particles following its lines contained in a reactor of finite size, is to loop the field back on itself. A toroidal configuration allows for an infinite number of encirclements encirclement. This is the principle idea behind the tokamak, schematically sketched in figure 1.4.

The toroidal magnetic field in the tokamak is created by placing (superconducting) coils around the plasma vessel. Because these coils are closer together on the inner side of the reactor, the magnetic field is higher here compared to the outer side. Without going into much details, this causes charge separation of ions and electrons and subsequently in particle drifts[2] directed radially outwards. Without any correction, the charged species in the plasma would be lost effectively immediately. The tokamak design solves this issue by addition of a poloidal component to the magnetic field, generated by a current. This is inductively driven in the toroidal direction by the transformer effect, with a central solenoid as the primary coil and the plasma itself acting as the secondary. Besides providing a stability to the plasma, the current heats the plasma as well through resistive or Ohmic heating, on which will be readdressed later.

The resulting magnetic field in the tokamak has a helical shape, with the field lines confined to nested surfaces in the shape of tori, called flux surfaces. This is illustrated clearly in figure 1.5. If the field line is followed for many toroidal rotations, it would generally densely cover such a surface. Because transport of heat and particles parallel to the field lines is typically orders of magnitude faster than perpendicular, quantities such as temperature and density are in good approximation constant on a flux surface [16].

The poloidal component of the magnetic field on a flux surface is related to the total enclosed current, which increases when moving radially outwards. With the toroidal component roughly constant over a poloidal cross-section, the helical field on each surface has a different pitch angle. Now a ratio is assigned to the number of toroidal and poloidal rotations a field line makes, which is called the safety factor

$$q = \frac{rB_{\text{tor}}}{RB_{\text{pol}}}, \tag{1.2}$$

with r the distance to the magnetic axis in the poloidal plane, R the major radius and B_{X} the magnetic field component in the indicated direction. The safety factor

---

[2] The charge separation causes a vertical electric field, which in combination with the toroidal magnetic field causes an $\mathbf{E} \times \mathbf{B}$-drift. See chapter 8.4 of [16] for a clear description.

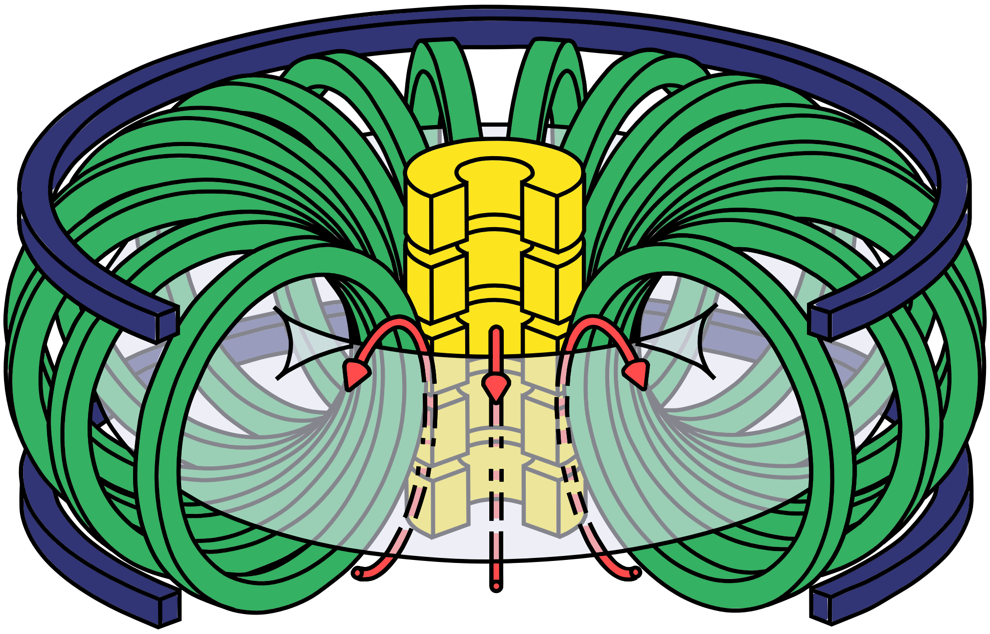

Figure 1.4: A schematic representation of the tokamak showing the plasma (white) confined by the magnetic field created by the toroidal magnetic field coils (green). A toroidal current is induced by the central solenoid (yellow), which in turn creates the poloidal magnetic field (red). The vertical magnetic field coils (blue) are used for plasma shaping and stability, but have no relevance in this thesis. With permission adapted from [18].

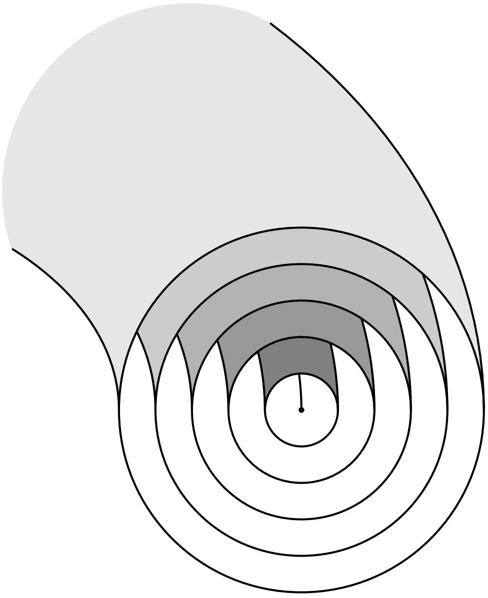

Figure 1.5: The magnetic field in a tokamak consists of nested torus-shaped flux surfaces. Quantities such as density or temperature are considered to be constant on such a surface due to fast transport along field lines.

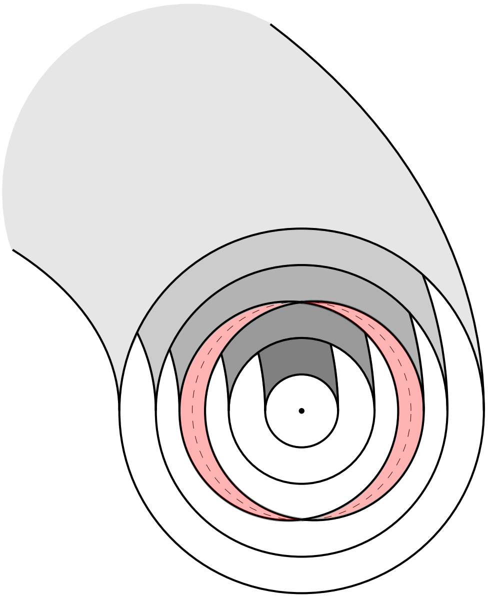

Figure 1.6: Magnetic islands, such as the $^{2}/_{1}$-island in this figure, are formed when the original flux surface (dashed) tears apart into a volume (red) that is topologically separated from the rest of the structure. The left half of the island connects to the right half after one toroidal round and vice versa, such that it makes up a single helical structure.

is a smooth function and thus has infinitely many rational and irrational values. An irrational value means that a field line will densely cover its flux surface, never returning to a position it has visited before. Flux surfaces with rational q-values are written as $^{m}/_{n}$ with the number of toroidal rotations m and number of poloidal rotations n both integers. A magnetic field line starting on such a rational surface bites itself in the tail after m toroidal and n poloidal rounds. On these rational surfaces the magnetic field can reorganize itself through a process called magnetic reconnection: The surface tears and forms a closed volume which reconnects back on itself after m rounds. Such a volume is called a magnetic island, because it is a topologically separated region. Islands are usually referred to by their ratio of indices $^{m}/_{n}$. A visualization is shown in figure 1.6. More details on the behavior of islands will be given further on.

In this section other magnetic confinement methods such as stellarators, magnetic mirrors, field pinches and completely different concepts such as inertial and electrostatic confinement have been completely disregarded. This is because the density limit investigated in this thesis is initially reported as a limit for tokamak experiments [19]. Even though other devices can show similar limits [20], in this thesis the limit will only be investigated for the devices where it was first encountered. Moreover, a restriction to (roughly) axisymmetric devices in our numerical methods is given later on.

1.4 Operational limits in fusion devices

Operation of tokamaks is bound by limits on the operating space of the fusion plasma inside, or operational limits for short. Exceeding a limit generally triggers unwanted behavior in the form of instabilities. If an instability is triggered and allowed to grow it can affect the macroscopic plasma parameters, leading to termination of the fusion plasma in a disruption, of which the temporal behavior is schematically given in figure 1.7. A disruption can manifest itself in different ways, but in all cases a significant amount of energy is lost from the plasma. Depending on the specific situation, several phenomena may occur: the energy confinement is decreased, causing the plasma to cool and through a change of the temperature-dependent resistivity the current profile is altered [21, 22]. Generally the current inside the plasma decreases, with the possibility of runaway electrons entering the reactor's vessel and damaging either diagnostics or the reactor itself [23]. Other types of damage can be due to massive heat loads on plasma facing components or high mechanical loads on the structure as the currents induce forces on the magnetic coils [24]. To prevent damage on the reactor, it is of importance to stay within the operational limits during operation.

The operating window for a fusion reactor can be derived from the global energy balance. In the D-T reaction from (1.1), the neutrons carry 80% of the freed energy per reactions and are used for power generation outside the plasma. The helium carries the other 20% of which a part is deposited in the plasma, therefore heating it. In a steady state burning plasma, the helium ions are used to sustain reaction and carry 20% of the total fusion power, so $P_{\mathrm{He}} = \frac{1}{5}P_{\mathrm{fusion}}$. This heat source is balanced by two loss terms: radial heat transport P_κ (diffusion) due to gradients in temperature and bremsstrahlung P_{brem} from the acceleration of high energy particles. With no external power applied to the plasma, the global heat balance becomes

$$P_{\mathrm{He}} = P_\kappa + P_{\mathrm{brem}}, \tag{1.3}$$

with corresponding formulas

$$\begin{aligned} P_{\mathrm{He}} &= \frac{1}{4}E_\alpha \langle\sigma v\rangle n_{\mathrm{e}}^2 = \frac{1}{16}E_\alpha p^2 \frac{\langle\sigma v\rangle}{T^2} \\ P_\kappa &= \frac{3}{2}\frac{p}{\tau_{\mathrm{E}}} \\ P_{\mathrm{brem}} &= \frac{1}{4}C_{\mathrm{B}} Z_{\mathrm{eff}} \frac{p^2}{T^{3/2}}. \end{aligned} \tag{1.4}$$

adapted from [16]. Here the T is the temperature, the total pressure is $p = 2n_eT$, $E_\alpha = E_{\mathrm{fusion}}/5$, C_B is a constant, Z_{eff} is the effective charge of the plasma (1 for hydrogen isotopes, but higher if helium ash or impurities are present) and τ_{E} is the energy confinement time. This time resembles the typical timescale on which energy is conserved in the reactor and is defined by the ratio between the total energy in the system and the input power required for steady state operation: $\tau_{\mathrm{E}} = E_{\mathrm{stored}}/P_{\mathrm{input}}$.

The result of the balance is a restriction on the triple product

$$n_e\tau_{\mathrm{E}}T \geq \frac{24T^2}{E_\alpha \langle\sigma v\rangle - 4C_B T^{1/2}}, \tag{1.5}$$

required to achieve ignition [16, 26]. This quantity is informative to determine the required temperatures and densities for a net energy producing fusion plasma. Rewrit-

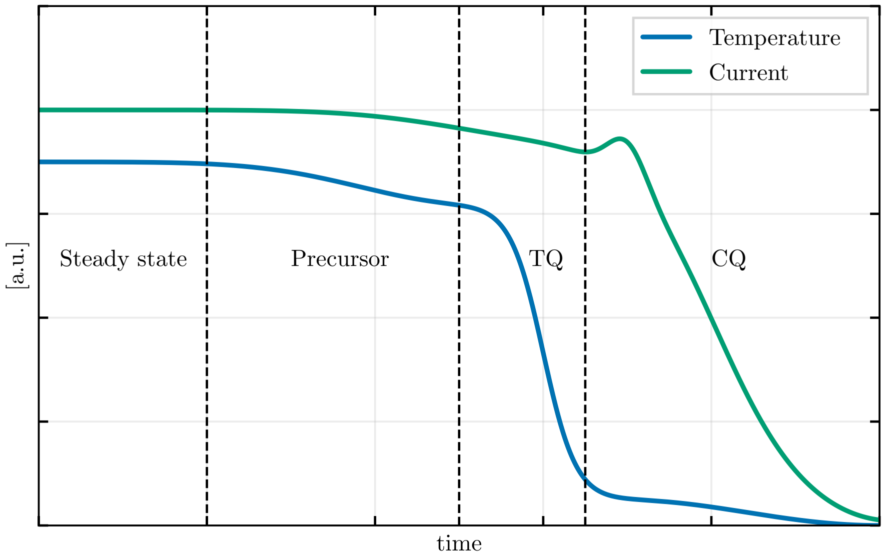

Figure 1.7: A precursor in the form of growing plasma instabilities can trigger a disruption in which the energy is lost from the plasma in a thermal quench (TQ), within typically a few milliseconds. The change in resistivity then causes the current profile to decay in a current quench (CQ) which lasts typically a few tens of milliseconds [25].

ing it to a restriction on the density as

$$n_e \geq \frac{12T}{\tau_\mathrm{E}\left(E_\alpha \left\langle \sigma v \right\rangle - 4C_B T^{1/2}\right)}, \tag{1.6}$$

gives additional insight and is shown in figure 1.8 for $\tau_\mathrm{E} = 10\,\mathrm{s}$. Besides the dependency of fusion power on density squared from equation (1.1), a condition is obtained for a minimum density below which fusion will not work. Moreover, this formulation allows for comparison with two important operational limits. The total kinetic pressure in a fusion reactor is limited to a fraction of the magnetic pressure $\frac{1}{2}B^2/\mu_0$ imposed by the magnetic field coils. This is the β-limit or Troyon limit [27]. The second is the Greenwald density limit, which limits the maximum allowable density, independent of the temperature. Both are shown in figure 1.8, from which it becomes clear that increasing the density for a higher fusion power output or to get into the operating regime is not always possible.

1.4.1 The Greenwald density limit

In the analysis of experiments in multiple tokamak devices, several processes are identified that limit the maximum attainable density. The most important ones are radiation from light impurities at the edge, radiation in the plasma core, low particle confinement in the core and insufficient fuelling [19]. In the more recent TEXTOR device, there are actually two distinct types of density limits distinguished. The first one occurs when there is a high concentration of impurities, the total radiated power may exceed the total (auxiliary) input power and the plasma quickly loses its stored energy [28, 29].

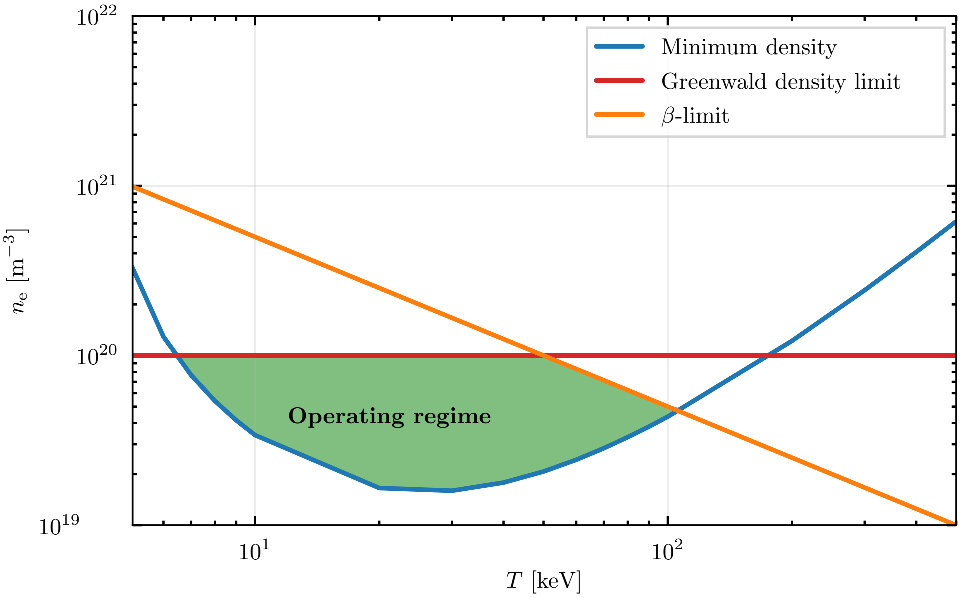

Figure 1.8: A minimal density is needed in a fusion reactor to achieve net energy production. The operating space (green) is further bound by the β-limit restricting the kinetic pressure and the Greenwald density limit. If the Greenwald limit could be exceeded, then higher densities at lower temperatures could be reached, thereby increasing the net fusion power.

The second type is distinctly different as it is also encountered in relatively clean plasmas with less radiation. As soon as a certain density is exceeded, a significant part of the stored energy is lost in a thermal quench. The resistivity of the cooling plasma increases and the current is transferred to the surrounding structures through induction in a current quench [30]. The onset for such disruption happens at a strict limit, which is effectively described by Greenwald et al. in 1988 in an attempt to describe at which density such a disruption takes place [19]. This work resulted in an empirical limit, which in its most well-known form states that the electron density n_e, averaged over a sight-line through the device, can not exceed the value of the Greenwald density n_G, which is clearly indicated in figure 1.9. In mathematical terms this means

$$\bar{n}_\mathrm{e}\left[10^{20}\mathrm{m}^{-3}\right] \leq n_\mathrm{G}\left[10^{20}\mathrm{m}^{-3}\right] = \frac{I_\mathrm{p}\,[\mathrm{MA}]}{\pi a^2[\mathrm{m}]}, \tag{1.7}$$

in which I_p is the total current and a the plasma's minor radius, i.e. the distance from magnetic axis to the plasma edge. A careful reader will notice that the units of the left- and right hand-sides do not match and that there are seemingly arbitrary magnitudes included along with the units in the square brackets. Furthermore, the presented relation between electron density and average current density is derived from empirical scaling studies such as in [19]. To present date, there is no fully accepted explanation to why the relation has this form or why specifically these quantities are in the scaling. Moreover, if the density limit would be related to a power balance, a strong dependency on external heating would be expected, but is absent.

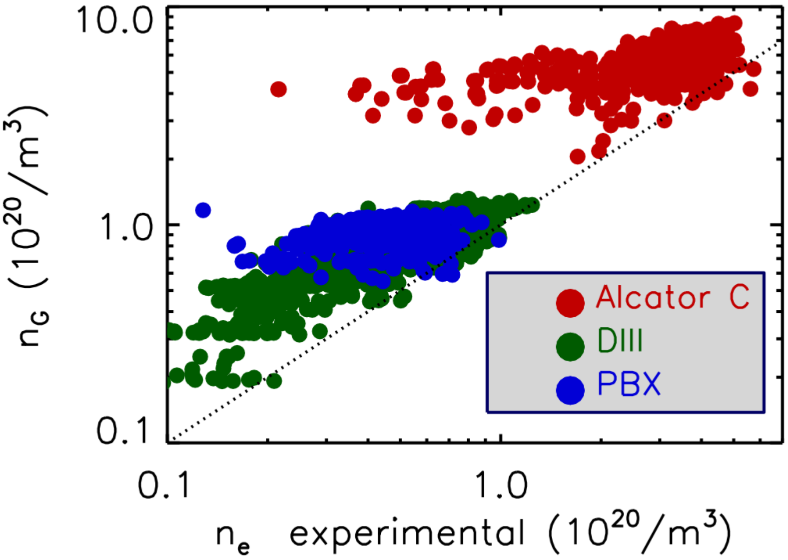

Figure 1.9: The empirical Greenwald density scaling (dotted line) is used to quantify the maximum attainable electron density before a disruption. Here it is shown that the experimental electron density is always lower or approximately equal to the Greenwald density at a disruption, for three tokamak devices (colored dots) over a wide range of densities [20].

Moreover, any effect of impurity density or type is not present in equation (1.7).

While gaining insight in the mechanism that triggers the sudden disruptions at the Greenwald density is interesting from a fundamental physical standpoint, the new knowledge can be used for more than solely that. Disruptions at the density limit are destructive and cause large forces on structural components and high currents in the reactor vessel, possibly leading to damaged diagnostics or components crucial to operation. These large disruptions get more intense for large devices and should be avoided at all costs for ITER, which will be equipped with disruption mitigation systems. [31, 32].

The density limit is in principle well described by the empirical scaling, but is unable to describe all experimental results. Experiments in TEXTOR have been able to surpass the limit by a factor 2 by controlling the impurity concentrations and providing external heating [28]. In DIII-D, operation in the high confinement mode (H-mode) reproducibly allows for densities 40% above n_G [33]. These results lead to questions about the completeness of the law in its current formulation and its validity regime. Operating an experiment above the Greenwald density should presently still be done with high uncertainty as there is no theory for the onset of the limiting factor present. A theory on the underlying physics would give fusion experiments a more solid, hopefully measurable, figure of merit to characterize disruption-free regimes. Prevention and prediction of the onset of the limit is only one side of the coin once the mechanism would be understood. It will open possibilities to explore pathways, operation modes or mechanisms to surpass the limit. This in turn may lead to a higher fusion power production as discussed with relation to figure 1.8 and hence being one step closer to net fusion energy production in a commercial reactor.

1.5 Current state of research

As a long-standing problem in tokamak physics, the Greenwald density limit has already been subject to multiple researches, trying to find its origin [30]. Multiple plausible mechanisms are proposed as part of the explanation: radiation from the edge, turbulence or radiation-driven (neoclassical) tearing modes [34, 30, 35]. The explanation focused on in this thesis is presented in a series of papers by the Princeton Plasma Physics Laboratories [35, 36, 37, 38, 39, 40]. The work consists mostly of a theoretical framework accompanied by semi-analytical and numerical analyses on the thermo-resistive tearing mode and radiation-driven islands. From here on the term *Gates-model* will be used to describe their collective work.

The Gates-model uses the resistive hydrodynamic (MHD) framework to describe magnetic islands as an instability therein. The plasma is described as a continuous, conducting fluid, so that equations for the flow as well as Maxwell's equations for electromagnetism need to be solved. The resistivity allows for formation and evolution of magnetic islands at rational flux surfaces, which evolve into topologically separated regions with a finite width. The formation and growth of islands involves the so-called tearing mode. The inner and outer boundary of a magnetic island, together called the separatrix, are connected by the same magnetic field lines. Combined with the transport along these lines that is typically many orders of magnitude faster than across, the separatrix can be seen as a flux surface. The boundary of the island has a uniform temperature and heat transport experiences a shortcut over the width of the island. A larger island directly leads to worse energy confinement. If the island grows substantially large this can possibly cause enough energy to be lost to trigger a disruption.

The tearing mode evolution is dependent on the resistivity, which scales with the temperature as $\eta_{\mathrm{Sp}} \sim T^{-3/2}$ according to Spitzer [41]. Net cooling or heating thus has an effect on the growth of the islands. It is already shown that islands with a saturated size can grow when cooled internally and shrink under influence of internal heating [40]. Further in the model, the interior of the islands is approximated as a thermally isolated region, with heat transport directed mainly around the island through its X-points, especially when it has a substantial width. Any external heating mechanisms (such as Neutral Beam Injection or Electron Cycloctron Resonance Heating) deposit their energy mainly outside the islands, for instance in the core of the plasma during normal operation, so that they do not affect the energy balance in the islands. The two energy sources that do contribute to the local energy balance inside are the Ohmic heating

$$P_\Omega = \eta_{\mathrm{Sp}} j^2, \tag{1.8}$$

with j the current density and radiative cooling due to the presence of impurities

$$P_{\mathrm{rad}} = n_{\mathrm{e}} n_{\mathrm{imp}} L_{\mathrm{rad}} \left(n_{\mathrm{e}}, T_{\mathrm{e}}\right), \tag{1.9}$$

with $L_{\mathrm{rad}} \left(n_{\mathrm{e}}, T_{\mathrm{e}}\right)$ the radiation power density. The energy balance between these terms forms the core of the Gates-model, which is schematically represented in figure 1.10.

The presence of impurities with a high atomic number Z in a plasma is detrimental for fusion performance due to this radiative cooling, even at high fusion temperatures of several keV. The reason for this is that atomic species with a high Z value take more energy than hydrogen isotopes or helium to become fully ionized, because they have more bound electrons. As long as electrons are bound to the atom, there are discrete

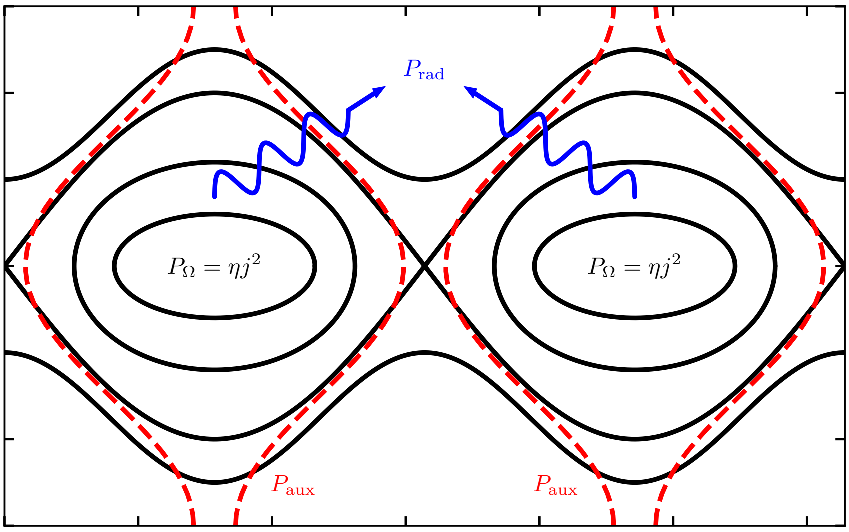

Figure 1.10: Schematic representation of the Gates model in which islands are heated by Ohmic heating P_Ω and cooled by radiation P_{rad} (blue). The majority of the heat from auxiliary sources P_{aux} is transported around the magnetic islands (red), so that in the internal power balance its contribution can be neglected.

energy levels for it to be in, hence it can transition between those under absorption and emission of line radiation. For example, the foreseen plasma-facing material for ITER is tungsten ($Z = 74$), which has around 20 bound electrons left around relevant fusion temperatures. Besides radiation, large concentrations of impurities are to be avoided because of their surplus of electrons, which cause the total electron density to increase. With the maximum number of electrons limited by the Greenwald density limit (1.7), this restricts the number of fusion fuel particles in a reactor.

The literature in which aspects of the Greenwald density limit are described using the Gates-model rely on analytical work in [35, 36]. After introduction of the mechanisms (local energy balance, Ohmic heating, radiative losses), the width of the magnetic islands in the poloidal plane is introduced as figure of merit [38]. The model including island width is then tested against the empirical formulation (1.7) using semi-analytical work in combination with nonlinear MHD simulations [39, 40].

1.6 Motivation for this research

The presented work on the Gates-model up until now is not complete yet. First and foremost, the set of situations for which the Greenwald density limit is specific and restricted to the Furth-Rutherford-Selberg equilibria, which act as model profiles when the profile's peakedness is a key parameter [42]. They are not necessarily representative for modern fusion reactors. Besides this, if radiation is such a crucial aspect for the density limit explanation, then one would expect a strong dependence on impurity density and temperature in the model and possibly in the empirical limit as well. A strong dependence of the Greenwald limit on impurity density is actually found in a parameter scan (figure 14 of [39]). This scaling is not consistent with the robust and universally encountered Greenwald limit. The authors of the paper solve this inconsistency by fixing the resistivity, which is not physically realistic. This means that the influence the different impurity concentrations have on the Ohmic heating is negated. However, the radiated power is allowed to change freely, which would result in an overestimation of the effectiveness of the mechanism. The presented work in this thesis aims to tweak parameters as consistently and physically accurate as possible. Another remark can be made about the cooling rate used in the literature. In reality this would be heavily dependent on impurity type, concentration and temperature, but strong dependencies are surprisingly absent. It is unlikely that this is the full picture, so that is why in this thesis an attempt will be made to explore a larger (impurity) density and temperature spectrum.

For this research the fully non-linear 3D MHD code `JOREK` will be used. This is a state-of-the art code, based on the Finite Element Method (FEM). In recent versions (model 501), it is able to solve for the main plasma parameters (introduced in 3) as well as a second particle population: the impurity density including its effects on radiation, the energy balance and flows. Also, the Ohmic heat source is implemented as a result, which provides `JOREK` with the last ingredient to properly test the Gates-model. The benefit of using `JOREK` is its non-linearity, making it possible to run deep into non-linear regimes of for instance disruptions. Simulations are possible where localized impurity radiation triggers a thermal quench and parts of the subsequent current quench [43]. This opens the possibility to not only look for large magnetic islands as a criterion, but also the subsequent phenomenology associated with density limit disruptions. In other words, there is an opportunity to see how large magnetic islands may cause loss of confinement and trigger a disruption. Moreover, `JOREK` is not limited to checking one phenomena at a time, but can handle complex physical situations with multiple mechanisms influencing each other. At last, at the boundary of this research, it is possible to run `JOREK` simulations in realistic experimental conditions, with correct geometry, X-point and plasma parameters. While only the physical mechanism for the density limit will be looked at, it is in principle possible to see this mechanism in future devices such as ITER and make predictions based upon that.

With this powerful computational tool in mind, the focus lies on the following aspects in this research:

- the validation of the island width as figure of merit in the Greenwald density limit problem,
- the mechanisms in the growth of radiating magnetic islands, which will be partly a verification of the work done in [40] where the relation between heating, cooling and island width is explained qualitatively,
- other equilibria than the self-consistent Furth-Rutherford-Selberg equilibria used in the Gates-model,
- the influence of electron density, electron temperature, impurity density and impurity type on the island growth with the aim to try to independently investigate the role of these quantities,
- the search for additional parameter dependencies in the Greenwald limit or explanations for their absence.

1.7 Research Question

Now that the problem statement, present state of research and new possibilities are clear, the research question for this project can be stated:

How does the semi-analytical model of radiative growth of magnetic islands relate to the empirical Greenwald density limit?

The following sub-questions will need to be answered in order to comment on the global research question:

- Can the mechanism presented by the Gates-model be observed in JOREK simulations?
- For which conditions is there an agreement with theory and experiments, and how accurate is it?
- Can the (lack of) dependencies in the empirical Greenwald limit be explained?
- What are the implications for future experiments?

The presented research in this thesis is the result of a combined graduation project at the Eindhoven University of Technology (TU/e) in the groups Science & Technology of Nuclear Fusion and Turbulence and Vortex Dynamics. This project has been supervised by Guido Huijsmans, Leon Kamp and Daan van Vugt. Under their supervision, the use of the MHD code `JOREK` in combination with High Performance Computation at MARCONI [3] has been possible. The recent addition impurities, Ohmic heating and radiative cooling to `JOREK` allows this research to be possible and investigate if new physics can be found with the added components.

1.8 Outline of this thesis

This thesis is structured in the following way. A theoretical overview of the relevant MHD quantities, along with a better look at the tearing mode and impurity radiation will be given in Chapter 2. The quantities and equations used by JOREK are shown in the first half of Chapter 3. The second half entails the general approach to this research, including which parameters to track, which knobs to turn and which additions or alterations to the code are done. Chapter 4 then shows the main results on the various aspects of the simulations, including tearing modes, impurity radiation and heat balances. These results are discussed and placed in context in Chapter 5. In Chapter 6 conclusions are drawn based on the presented results and an outlook is given for future experiments based on extrapolations of the current work. This is paired with recommendations for future work on this subject. The appendices present the convergence and validation studies of the simulations in Appendix A, details on the magnetic island finding and tracing routines in Appendix B and the `JOREK` normalization in Appendix C.

---

[3] ranked as 19th most powerful, commercially available HPC as per November 2019

2. Theoretical Background

This chapter is meant to briefly introduce the theoretical background needed to understand the numerical methods and results in the next chapters. The focus lies on the applicability and validity, hence no full derivations are given. A more thorough description on magnetohydrodynamics (MHD) or tearing modes can be found in [16, 44, 45].

2.1 Magnetohydrodynamics

The magnetohydrodynamic framework is used to describe a collection of many ionized particles as a magnetized fluid using balances from hydrodynamic theory in combination with electromagnetic contributions. The set of equations that are used to describe a plasma consists of a mass continuity equation, a momentum equation similar to Navier-Stokes and an energy equation. Electric and magnetic components are added by including Maxwell's equations to the set. The explicit form of the equations used in this research is given in Chapter 3.

Because the set of MHD equations uses only continuous descriptions, validity restrictions on time and length scales are inevitable. In figure 2.1 the MHD model is placed in perspective along with approximate scales of typical quantities and phenomena. An ideal description would solve the equations of motion for every individual particle, but this is simply not feasible for large systems with particle densities of the order 10^{20} m^{-3}, because of the computational costs required. The Vlasov model reduces the problem to distribution functions and the gyrokinetic model eliminates the gyration of charged particles around magnetic field lines. Each step reduces the computational cost of the system in exchange for not being able to resolve an increasing number of physics phenomena. The MHD model is used for describing macroscopic processes on relatively long timescales, such as edge localized modes (ELMs) and tearing modes in tokamak plasmas.

Typical timescales

One of the typical timescales in resistive MHD is the resistive time

$$\tau_{\mathrm{R}} = \frac{\mu_0 a^2}{\eta}, \tag{2.1}$$

with μ_0 the magnetic permeability, a a typical length scale (plasma minor radius) and η the resistivity. It can be used to directly compare timescales of the growth of resistive phenomena such as magnetic island growth, when resistivity or temperature differ [40].

A typically much shorter timescale is the Alfvén time

$$\tau_{\mathrm{A}} = \frac{a\sqrt{\mu_0 \rho_0}}{B_0} \tag{2.2}$$

with ρ_0 the equilibrium density and B_0 the unperturbed magnetic field. The time normalization used by `JOREK`, introduced in chapter 3, will show similarities to this time scale.

The ratio between these times is the Lundquist number

$$S = \frac{\tau_{\mathrm{R}}}{\tau_{\mathrm{A}}} = \frac{B_0 a}{\eta}\sqrt{\frac{\mu_0}{\rho_0}}, \tag{2.3}$$

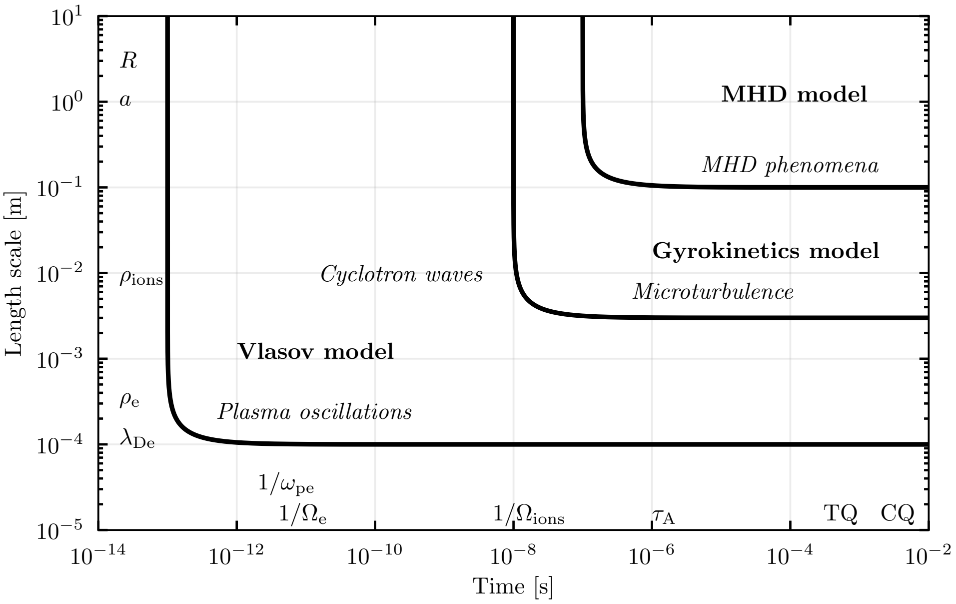

Figure 2.1: A plasma is characterized by a cascade of length and time scales: from experiment dimensions R, a via Larmor radii $\rho_\mathrm{ions/e}$ to the Debye length λ_De and from plasma oscillations ω_pe and cyclotron frequencies $\Omega_\mathrm{ions/e}$ via Alfvén time τ_A to typical time scales for the thermal quench (TQ) and current quench (CQ). Approximate regimes for phenomena and applicable models to describe them are indicated. Adapted from [46].

which can be seen as a magnetic Reynolds number for the case that the Alfvén velocity is used as the typical velocity. As the ratio between a resistive and a plasma timescale, it is proportional to the typical time it takes for a tearing mode to grow and saturate, discussed hereafter [40].

2.2 Tearing modes

The instability that lies at the core of the formation and growth of magnetic islands is the tearing mode. In a plasma with a finite resistivity, magnetic field lines may tear apart and reconnect, hence the name for this mode. This causes a change in topology, and subsequent magnetic island may grow as illustrated in figure 2.2. It can be shown that the resistivity is only important around rational q-surfaces [47]. So at these locations in tokamak plasmas the magnetic islands will form and grow, conceptually shown in figure 1.6.

2.2.1 Linear perturbation theory

The aim of this section is not to give a full derivation of the growth of the tearing mode, since that is already done excellently in [48]. Only the for this research relevant time scales and general dependencies of the tearing mode are written here.

In a plasma the tearing mode may grow on interfaces where there is magnetic shear: a change in parallel field strength across it. Then, from an equilibrium situation a

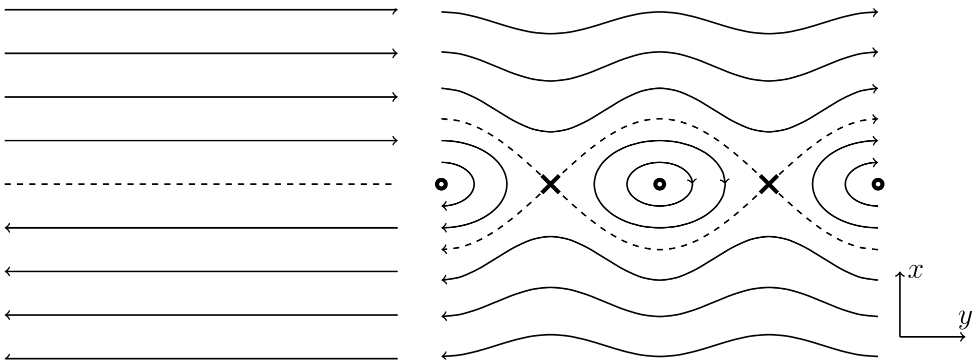

Figure 2.2: Left: The magnetic field lines with a sudden jump in direction or strength can be unstable for the tearing mode. Right: After reconnection the topology is changed and magnetic islands can grow, seperated from the main magnetic field by the separatrix (dashed). The X-points, where the separatrix legs meet, and the O-points in the center of the islands are indicated with crosses and circles respectively.

slight perturbation of the form $A\left(\mathbf{x},t\right)=A\left(x\right)e^{iky+\gamma t}$ is added to the magnetic field, density and velocity. Linear stability analysis of the MHD equations results in an instability growth rate for the magnetic perturbation of

$$\gamma \sim \frac{\left(\Delta'\right)^{4/5}}{\tau_H^{2/5}\tau_R^{3/5}}. \tag{2.4}$$

Here, Δ' is the tearing stability index, which determines if the tearing mode is stable ($\Delta' < 0$) or unstable ($\Delta' > 0$) and is depending on plasma equilibrium and position in the plasma [49, 38]. The hydromagnetic time-scale is defined by

$$\tau_{\mathrm{H}} \sim \frac{\tau_{\mathrm{A}}}{ka} \tag{2.5}$$

and depends on the wave number k of the specific mode.

The tearing mode then grows on a hybrid timescale

$$\tau_{\mathrm{TM}} \sim \frac{1}{\gamma} \sim \tau_H^{2/5}\tau_R^{3/5} \sim \left(\frac{\mu_0^4\rho_0 a^6}{k^2\eta^3}\right)^{1/5} \sim \eta^{-3/5}, \tag{2.6}$$

as is consistent with findings of Wesson [50] and Rutherford [49]. This also implies that the typical growth rate of the tearing mode scales as $\gamma \sim \eta^{3/5} \sim T_{\mathrm{e}}^{-9/10}$ if the Spitzer scaling is assumed for the resistivity [41].

2.2.2 Nonlinear phenomena

The linear perturbation theory can only be used as an accurate description during the first moments of the growing instability, when the perturbations do not affect the equilibrium quantities. As soon as the tearing mode grows substantially and the formed magnetic islands have a non-negligible width, nonlinear theory is necessary for an accurate description.

During the nonlinear phase the islands grow until a saturated, steady state is reached.

Heat transport

Magnetic field lines on the edge of magnetic islands, the separatrix, travel helically around the island itself, similar to the magnetic island itself winding around the torus. This means that such a field line creates a connection between different radii in the poloidal plane, which acts like a shortcut for energy transfer as the heat conductivity along field lines is typically much larger than across: $\chi_\parallel/\chi_\perp \approx 10^8$. Here χ is the heat transfer coefficient which appears in the calculation of heat flux: $\mathbf{q} = n\chi\nabla T$, with n the particle density and T the temperature. However, as field lines near the X-point of the separatrix, stagnation occurs by which the number of toroidal windings to cross the X-point increases drastically and thereby reducing the efficiency of the parallel heat transport [45]. In regions where this parallel transport dominates, the temperature profile is flattened, which is seen first around the O-point of islands. Fitzpartrick found that this flattening occurs when the island's width is approximately larger or equal than a critical width given by

$$w_c = \left(\frac{\chi_\parallel}{\chi_\perp}\right)^{-1/4} \left(\frac{8Rq}{n\frac{\partial q}{\partial r}}\right)^{1/2}, \tag{2.7}$$

[51].

For sufficiently large islands at different radial locations, interaction will produce stochastic regions in the magnetic field around them. In comparison to a non-ergodic situation, radial transport is enhanced by the magnetic field lines connecting the islands [45, 52].

Neoclassical tearing modes

The presented theory on tearing modes in this section should not be confused with the neoclassical tearing mode (NTM), which is the result of nonlinear excitation of the regular tearing mode. In this scenario, the flattened pressure inside an already existing seed island lowers the bootstrap current and drives the island more unstable, if the seed islands have an initial minimum critical width [53]. NTMs are outside the scope of this research and will not be included in the numerical methods.

3. Numerical Methods

3.1 Nonlinear MHD code `JOREK`

`JOREK` is a fully non-linear MHD code capable of calculating the temporal evolution of a fusion plasma in realistic configurations including the plasma core, X-point and scrape-off layer until the divertor. The code is initially developed for stability studies on Edge Localized Modes (ELMs) [54], but has since been used to simulate various onsets of disruptions including tearing mode growth [55] and rapid cooling due to impurity injections [43].

`JOREK` internally consists of a collection of different models, each solving a set of equations for the same quantities, but also introducing different specialized additions to the code. In this project model 501 is used, which adds a continuity equation for the impurity density, compared to the core set of equations [43]. Additional alterations are realistic Ohmic heating based on Spitzer resistivity and impurity radiation assuming Coronal equilibrium. When covering the quantities and their equations in this chapter, extra attention will be given to aspects unique to model 501.

3.1.1 Coordinate systems

The coordinate system in `JOREK` is left-handed and cylindrical, defined by (R, Z, ϕ) according to figure 1.5. In a poloidal plane it is possible to additionally use a polar coordinate system with (r, θ).

In tokamaks the magnetic field is nearly uniform in the toroidal direction, or *almost potential*, which allows us to use reduced MHD in `JOREK` [56]. This allows the full set of MHD equations to be reduced by 1 parameter and 1 equation, thereby making it more computational friendly. In reduced MHD a divergence-free magnetic field can be written as

$$\mathbf{B} = \nabla\psi \times \nabla\phi + F\nabla\phi \tag{3.1}$$

in which ψ is the poloidal magnetic flux, labeling the flux surfaces in a tokamak, and $F = F(R, Z, t)$ a general function independent of toroidal angle ϕ. In `JOREK`, the factor scaling the toroidal magnetic field is $F = F_0 = \text{constant}$, such that B_ϕ scales with $\frac{1}{R}$. This means that the toroidal magnetic field is axisymmetric and effects as magnetic ripples due to a finite number of coils are discarded. This is acceptable for (theoretical) studies in which the poloidal plane is mostly looked at. In this coordinate system, The total velocity vector is written as

$$\mathbf{v} = v_{||}\mathbf{B} - R^2\nabla u \times \nabla\phi, \tag{3.2}$$

with u as a flow function and $v_{||}$ the component parallel to the magnetic field.

3.1.2 Discretization

Full information on the `JOREK` discretization is given in [57], of which a brief overview is given here. The poloidal plane is discretized in both the radial and poloidal direction, as shown in figure 3.2. Each of the resulting elements has local coordinates (s, t) which range between 0 and 1. Inside an element, a quantity Y can continuously be expressed with

$$Y(s, t) = \sum_{i=0}^{3}\sum_{j=0}^{3} P_{i,j} B_i^3(s) B_j^3(t), \tag{3.3}$$

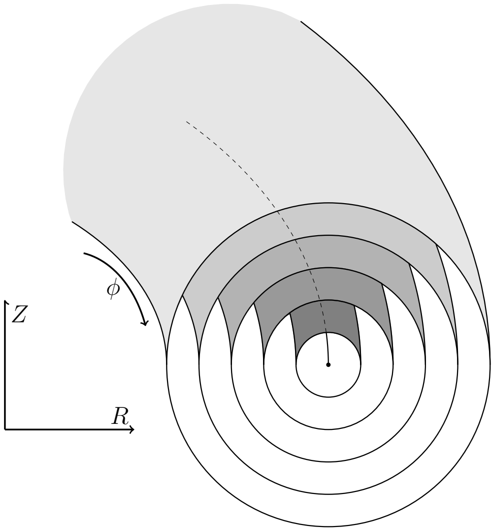

Figure 3.1: `JOREK` uses a left-handed cylindrical coordinate system to specify spatial positions in the plasma. R is the radial distance measured from the symmetry axis, Z the vertical displacement relative to the midplane and ϕ the toroidal angle in counter-clockwise direction when looked at from above.

Table 3.1: Fourier series for the toroidal discretization in `JOREK` for a device with periodicity of 2π.

`JOREK` harmonics	Basis function
1	1
2	$\cos(\phi)$
3	$\sin(\phi)$
4	$\cos(2\phi)$
5	$\sin(2\phi)$
...	...
`n_tor-1`	$\cos((\texttt{n\_tor}-1)\,\phi/2)$
`n_tor`	$\sin((\texttt{n\_tor}-1)\,\phi/2)$

i.e. a linear combination of functions in which information about the quantity is stored in $P_{i,j}$. $B_i^3(s)$ are a third-order Bernstein polynomials defined by

$$B_i^3(s) = \frac{3!}{i!\,(3-i)!} s^i \,(1-s)^{3-i} \tag{3.4}$$

and shown in figure 3.3. The requirement that the function values and first-order derivatives are continuous on the intersection between elements, only specific combinations of $P_{i,j}$ are valid, leaving four free parameters for each combination in $(i,j) = (0,0), (0,3), (3,0), (3,3)$ per quantity. The function for Y is then projected on the elements where it is used on the Gaussian points.

For the toroidal direction, the real part of a Fourier series is used: sines and cosines. For set of 2 `JOREK` harmonics added to the simulation, an additional sine and cosine are included, as can be seen in table 3.1.

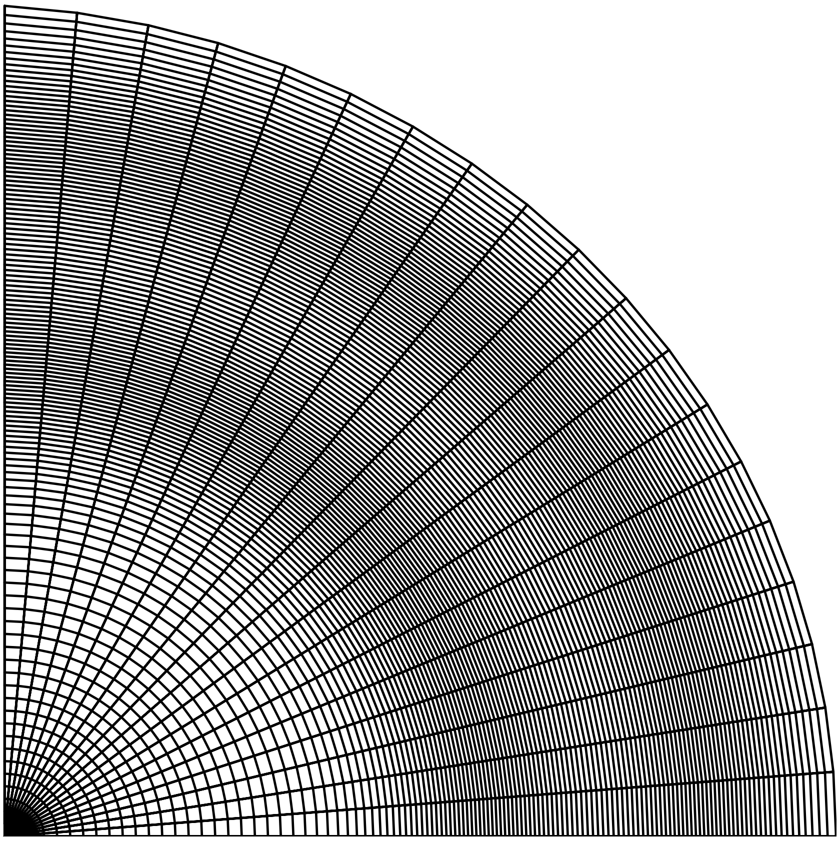

Figure 3.2: A quarter of the poloidal grid used in the `JOREK` simulations is shown with 126 and 76 elements in radial and poloidal directions respectively. Each element has local coordinates (s, t). The radial size of the elements is varied to increase the resolution around the $q = 2$ and $q = 3$ surfaces.

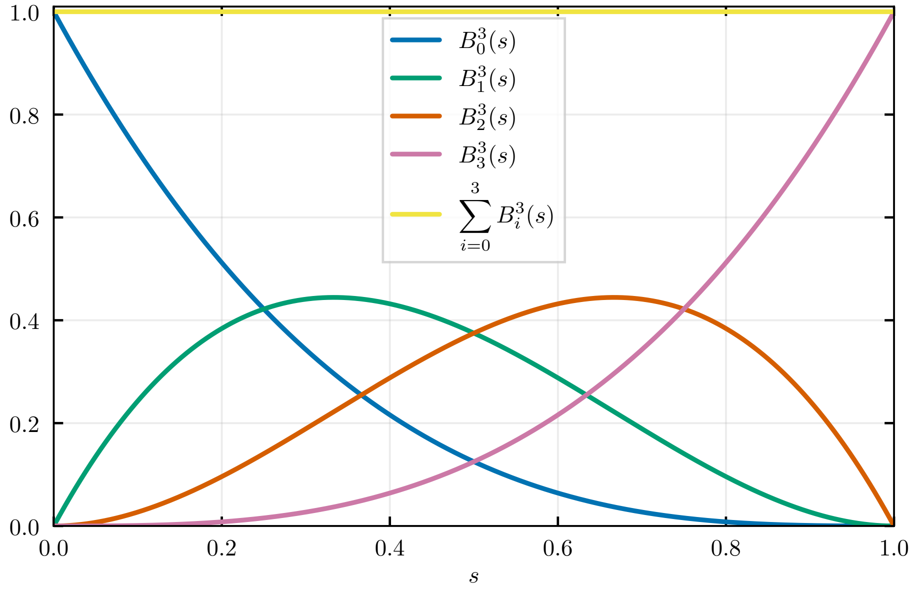

Figure 3.3: The 3rd order Bernstein polynomials as defined by 3.4 are shown. The set is a normalized one, as the sum of the four curves is equal to one.

3.1.3 Normalization

Quantities in `JOREK` are not calculated in SI units, but rather in their own self-consistent system. While they are transformed into a dimensionless description, there is some normalization based on a group of parameters which will be discussed here, such that the equations in the next section can be shown in their implemented form.

Two parameters that define the majority of the normalization routine are

$$\begin{aligned} n_0\left[\mathrm{m}^{-3}\right] &= \texttt{central\_density}\cdot 10^{20} \\ \rho_0\left[\mathrm{kg\ m}^{-3}\right] &= \texttt{central\_mass}\cdot n_0\cdot m_{\mathrm{proton}} \end{aligned} \tag{3.5}$$

which can be seen as scalings for the number density and mass density profiles, respectively. The main plasma species, which is reflected by the constants $m_{\mathrm{proton}} = 1.673\cdot 10^{-27}$kg and `central_mass` $= 2$. The term `central_density` will be varied to allow parameter scans in which multiple quantities are scaled consistently. The normalizations of time, density and temperature are

$$\begin{aligned} t_{\mathrm{SI}}\,[\mathrm{s}] &= t_{\texttt{JOREK}}\cdot\sqrt{\mu_0\rho_0} \\ T_{\mathrm{SI}}\,[\mathrm{eV}] &= T_{\texttt{JOREK}}/\left(e\mu_0 n_0\right) \\ n_{\mathrm{SI}}\left[\mathrm{m}^{-3}\right] &= \rho_{\texttt{JOREK}} n_0 \end{aligned} \tag{3.6}$$

with $\mu_0 = 4\pi\cdot 10^{-7}$ Vs/(Am), $e = 1.602\cdot 10^{-19}$ C and in which the temperature is that of the total plasma: $T = T_{\mathrm{electrons}} + T_{\mathrm{ions}}$. A more extensive list of normalized quantities can be found in C. By the definitions above, the total plasma pressure is

$$\begin{aligned} p_{\mathrm{SI}}\left[\mathrm{N/m}^2\right] &= n_{\mathrm{SI}} e T_{\mathrm{SI}} \\ &= \rho_{\texttt{JOREK}} n_0 e T_{\texttt{JOREK}}/\left(e\mu_0 n_0\right) \\ &= \rho_{\texttt{JOREK}} T_{\texttt{JOREK}}/\mu_0 \end{aligned} \tag{3.7}$$

Table 3.2: Mathematical definitions

Symbol	Definition	Description
$\{f, g\}$	$R\,(\nabla f \times \nabla g) \cdot \nabla \phi$	Poisson brackets
$\Delta^* f$	$R\frac{\partial}{\partial R}\left(\frac{1}{R}\frac{\partial}{\partial R}f\right) + \frac{\partial^2}{\partial Z^2}f$	Laplacian-like operator with components in the poloidal plane
$\nabla_{\text{pol}} f$	$\frac{\partial f}{\partial R}\nabla R + \frac{\partial f}{\partial Z}\nabla Z$	Components of the gradient in the poloidal plane

and thus independent of the choice of normalization. In other words, when doing a parameter scan by variation of `central_density`, the density and temperature profiles scale such that the pressure is unaffected.

From here on all expressions and equations are given in `JOREK` units, unless stated otherwise or units are explicitly written. Furthermore, the main plasma component will be deuterium, indicated with subscript D.

3.1.4 Quantities and their equations

`JOREK` model 501 solves a set of equations for the following 8 quantities: the poloidal magnetic flux ψ, the flow function u, the toroidal current density j, the toroidal vorticity ω, the total mass density ρ, the temperature T, the parallel velocity $v_{\|}$ (in toroidal direction) and the impurity mass density ρ_{imp}.

Model 501 has some definitions of quantities that are distinctly different than other version of the code. Neglecting the electron masses, the densities are related by $\rho = \rho_{\text{D}} + \rho_{\text{imp}}$. For the temperature it is assumed that all species have the same temperature $T/2$, such that $T = T_{\text{e}} + T_{\text{D}}$. The total pressure is defined by the product of the total particle density and temperature: $P = n_{\text{tot}}T/2$. Using charge neutrality, $n_{\text{e}} = n_{\text{D}} + \langle Z\rangle_{\text{imp}} n_{\text{imp}}$, the total density is rewritten as $n_{\text{tot}} = n_{\text{D}} + n_{\text{e}} + n_{\text{imp}} = 2n_{\text{D}} + \left(\langle Z\rangle_{\text{imp}} + 1\right) n_{\text{imp}}$. With the additional relations between particle and mass density $\rho_{\text{X}} = n_{\text{X}} m_{\text{X}}$, the final form is

$$n_{\text{tot}} = \frac{2}{m_{\text{D}}}\left(\rho + \left[\frac{\left(\langle Z\rangle_{\text{imp}} + 1\right) m_{\text{D}}}{2m_{\text{imp}}} - 1\right]\rho_{\text{imp}}\right) = \frac{2}{m_{\text{D}}}\left(\rho + \alpha\rho_{\text{imp}}\right). \tag{3.8}$$

Finally, the total pressure in `JOREK` units is

$$P = n_{\text{tot}}T/2 = \left(\rho + \alpha\rho_{\text{imp}}\right)T. \tag{3.9}$$

The terms that are unique to model 501 (including P) will be written in red in the equations below and explained if necessary. Non-trivial mathematical operations are written in table 3.2.

The poloidal flux is solved with the induction equation

$$\frac{\partial \psi}{\partial t} = \eta\,(j - j_0) - R\,\{u, \psi\} - F_0\frac{\partial u}{\partial \phi}, \tag{3.10}$$

where η is the resistivity which is scaled with temperature like the Spitzer resistivity ($\sim T_e^{-3/2}$) [41], with respect to a user defined input value. The first term on the right hand side contains a combination of the local current density j and a source current density j_0 which can be customized.

The current density is calculated with Ampère's law:

$$j = \Delta^* \psi. \tag{3.11}$$

This quantity is not a real current density, because it is multiplied by the local coordinate R. The real toroidal current density is $j_\phi = -j/R$.

The equations for vorticity and parallel momentum are both derived from a global momentum equation:

$$\frac{\partial \rho \mathbf{v}}{\partial t} = \mathbf{J} \times \mathbf{B} - \nabla P + \nu \nabla^2_{\mathrm{pol}} \mathbf{v} - \nabla \cdot (\rho \mathbf{v})\, \mathbf{v} - \rho \mathbf{v} \cdot \nabla \mathbf{v} \tag{3.12}$$

and obtained by specific vector operations which filter out the required components.

The vorticity equation is obtained by applying the operation $\nabla\phi \cdot \nabla \times \left(R^2 ...\right)$ on the momentum equation, as the rotation of a velocity field is the vorticity. This results in

$$\begin{aligned} R\nabla \cdot \left[R^2 \left(\rho \nabla_{\mathrm{pol}} \frac{\partial u}{\partial t} + \nabla_{\mathrm{pol}} u \frac{\partial \rho}{\partial t}\right)\right] =& \frac{1}{2}\left\{R^2 \left\|\nabla_{\mathrm{pol}} u\right\|^2, R^2 \rho\right\} + \left\{R^4 \rho \omega, u\right\} \\ &- R\nabla \cdot \left[R^2 \nabla_{\mathrm{pol}} u \nabla \cdot (\rho \mathbf{v})\right] + \{\psi, j\} \\ &- \frac{F_0}{R}\frac{\partial j}{\partial \phi} + \left\{P, R^2\right\} + R\mu \nabla^2_{\mathrm{pol}} \omega, \end{aligned} \tag{3.13}$$

in which μ is the user specified viscosity scaled with $T_{\mathrm{e}}^{-3/2}$.

The total continuity/density equation is

$$\frac{\partial \rho}{\partial t} = -\nabla \cdot (\rho \mathbf{v}) + \nabla \cdot \left[D_{\mathrm{D}} \nabla \left(\rho - \rho_{\mathrm{imp}}\right)\right] + \nabla \cdot \left(D_{\mathrm{imp}} \nabla \rho_{\mathrm{imp}}\right) + S_{\mathrm{D}} + S_{\mathrm{imp}}, \tag{3.14}$$

in which D_{D} and D_{imp} represent the diffusion coefficients for the deuterium and impurity ions respectively, and S_D and S_{imp} are source terms for the two species.

The pressure equation is

$$\begin{aligned} \frac{\partial P}{\partial t} =& - \mathbf{v} \cdot \nabla P - \gamma P \nabla \cdot \mathbf{v} + \frac{2}{3R^2} \eta_{\mathrm{Sp}} j^2 + \nabla \cdot \left(\kappa_\perp \nabla_\perp T + \kappa_\parallel \nabla_\parallel T\right) \\ & - n_{\mathrm{e}} n_{\mathrm{imp}} L_{\mathrm{rad}} - f\left(E_{\mathrm{ion}}\right), \end{aligned} \tag{3.15}$$

which includes the adiabatic index $\gamma = 5/3$, and in which $\kappa_\perp$ and $\kappa_\parallel$ are the heat conductivities perpendicular and parallel to the magnetic field respectively, L_{rad} is the radiation density function and $f\left(E_{\mathrm{ion}}\right)$ is a function containing all contributions of the ionization potential of the impurities:

$$\begin{aligned} f\left(E_{\mathrm{ion}}\right) =& - \frac{2}{3} n_{\mathrm{imp}} \frac{\partial E_{\mathrm{ion}}}{\partial T_{\mathrm{e}}} \frac{\partial T_{\mathrm{e}}}{\partial t} - \frac{2}{3} E_{\mathrm{ion}} \frac{\partial n_{\mathrm{imp}}}{\partial t} \\ & - \frac{2}{3} E_{\mathrm{ion}} n_{\mathrm{imp}} \nabla \cdot \mathbf{v} - \frac{2}{3}\left[n_{\mathrm{imp}} \frac{\partial E_{\mathrm{ion}}}{\partial T_{\mathrm{e}}} \mathbf{v} \cdot \nabla T_{\mathrm{e}} + E_{\mathrm{ion}} \mathbf{v} \cdot \nabla n_{\mathrm{imp}}\right] \end{aligned} \tag{3.16}$$

The parallel velocity is obtained by applying the operation $\mathbf{B} \cdot ...$ on the momentum equation, such that only the terms parallel to the magnetic field are left:

$$\begin{aligned} B^2 \frac{\partial \rho v_\parallel}{\partial t} = & -\frac{1}{2} \rho \frac{F_0}{R^2} \frac{\partial \left(v_\parallel B\right)^2}{\partial \phi} - \frac{\rho}{2R} \left\{ B^2 v_\parallel^2, \psi \right\} - \frac{F_0}{R^2} \frac{\partial P}{\partial \phi} + \frac{1}{R} \left\{ \psi, P \right\} \\ & - B^2 \nabla \cdot \left(\rho \mathbf{v}\right) v_\parallel + B^2 \mu_\parallel \nabla_{\mathrm{pol}}^2 v_\parallel , \end{aligned} \tag{3.17}$$

in which $\mu_\parallel$ is the parallel viscosity which can be defined by the user.

Lastly, the continuity equation for the impurity population is

$$\frac{\partial \rho_{\mathrm{imp}}}{\partial t} = -\nabla \cdot \left(\rho_{\mathrm{imp}} \cdot \mathbf{v}\right) + \nabla \cdot \left(D_{\mathrm{imp}} \nabla \rho_{\mathrm{imp}}\right) + S_{\mathrm{imp}}, \tag{3.18}$$

which has the exact form of the regular `JOREK` continuity equation without impurities, after dropping the subscripts.

3.1.5 Heat sources and sinks

The addition of the impurity density is specifically useful for studies in which the heat balance is a key element, as is reflected in the multiple red terms in the pressure equation (3.15). To accurately describe the physics the impurities add, some additional quantities are introduced here.

The effective charge state

$$Z_{\mathrm{eff}} = \frac{\sum_i n_i Z_i^2}{\sum_i n_i Z_i} \tag{3.19}$$

is defined such that it has the dimension of a charge. The summation includes different charge states and species i in the plasma, so that both deuterium (fully ionized with $Z = 1$) and impurities (charge states between $Z = 0$ and $Z = Z_{\mathrm{imp}}$) are represented. Note that the effective charge weighs large impurities more heavily and it is therefore not the same as the average charge state.

The Spitzer resistivity is given by

$$\eta_{\mathrm{Sp}} = \frac{\sqrt{2 m_{\mathrm{e}}} Z_{\mathrm{eff}} e^2 \ln \Lambda}{12 \pi^{3/2} \epsilon_0 T_{\mathrm{e}}^{3/2}} F\left(Z_{\mathrm{eff}}\right), \tag{3.20}$$

with

$$F\left(Z\right) = \frac{1 + 1.198 Z + 0.222 Z^2}{1 + 2.966 Z + 0.753 Z^2} \tag{3.21}$$

as an empirical fitting function to add the effect of the changing effective charge state in the plasma [41]. Further variables in this expression are the electron mass m_{e}, electron charge e, Coulomb logarithm $\ln \Lambda$ and vacuum permittivity ϵ_0. With η_{Sp} the physical Ohmic heating is included in equation (3.15) as replacement for an arbitrary heat source. The physical consequence is that cold fusion plasmas are more strongly heated than hot ones, for a given current profile. Without auxiliary heat sources, the plasma will not reach temperatures of several keV, which is in line with experiments that almost always have additional neutral beam injection (NBI), electron or ion cyclotron heating (ECRH/ICRH) [58, 59]. Model 501 is able to simulate the prominent role of Ohmic heating in the Gates-model and allows for extension of this model by adding additional customized sources.

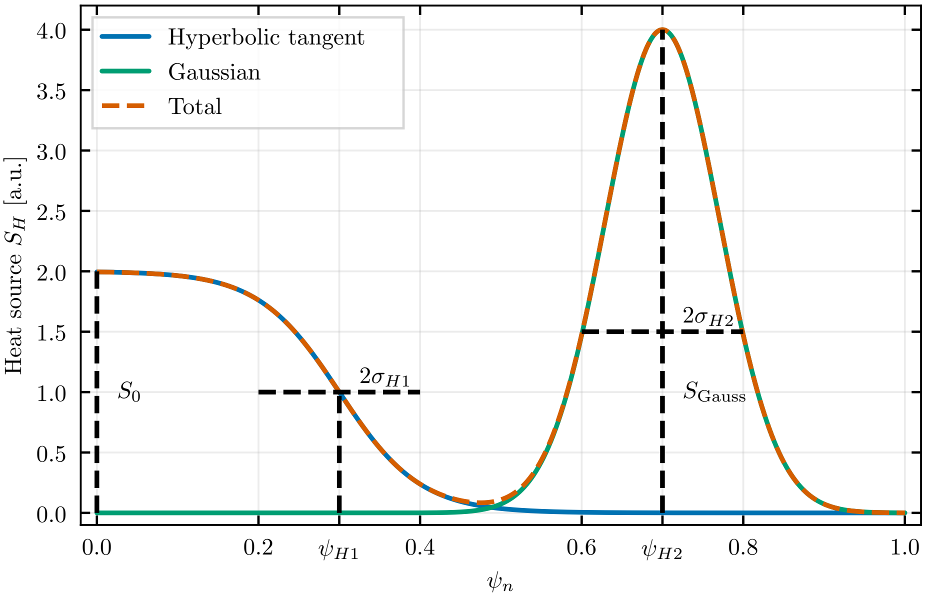

Figure 3.4: The heat source profile is made up of a hyperbolic tangent combined with a localized Gaussian function based on equation (3.22). Both can be scaled in strength, location and typical width.

The spatially localized heat source in `JOREK` is split up in two parts, consisting of a hyperbolic tangent in combination with a Gaussian function, both as function of the normalized flux ψ_N. In equation form this is given by

$$S_{\mathrm{H}} = S_0 \left(\frac{1}{2} - \frac{1}{2} \tanh \left[\frac{\psi_n - \psi_{H1}}{\sigma_{H1}} \right] \right) + S_{\mathrm{Gauss}} \exp \left[- \left(\frac{\psi_n - \psi_{H2}}{\sigma_{H2}} \right)^2 \right], \tag{3.22}$$

with S_0 and S_{Gauss} indicating the strength of the sources, ψ_{H1} and ψ_{H2} their locations, and σ_{H1} and σ_{H2} the typical width of the source. The construction of the heat source profile is given schematically in figure 3.4. The coefficients can be tuned such that the effects of central heating with a large radial profile centered around the magnetic axis or localized heating around a specific flux surface can be mimicked.

Besides sources, an additional energy sink is present in model 501 in the form of radiative cooling, represented by $n_{\mathrm{e}} n_{\mathrm{imp}} L_{\mathrm{rad}}$ in the pressure equation. The dependence on impurity type X, electron density and electron temperature is stored in the radiation power density $L_{\mathrm{rad}} = f\left(X, n_{\mathrm{e}}, T_{\mathrm{e}}\right)$. This quantity is obtained by interpolation of data retrieved from the free version of the Atomic Data and Analysis Structure (OPEN-ADAS). The data set provides coefficients for recombination, ionization, charge exchange, line radiation and continuum radiation like bremsstrahlung. Combination of these coefficients gives an effective radiation function which will be used as L_{rad} in this research. For a fixed electron density, the radiation curves of several species is given as a function of electron temperature in figure 3.5.

The radiation functions from ADAS are computed for systems in coronal equilibrium. In such system the charged state distribution of an atomic species is in equilibrium and constant in time for a given electron density and temperature. On one hand there is ionization through collisions with free electrons and auto-ionization, on the other

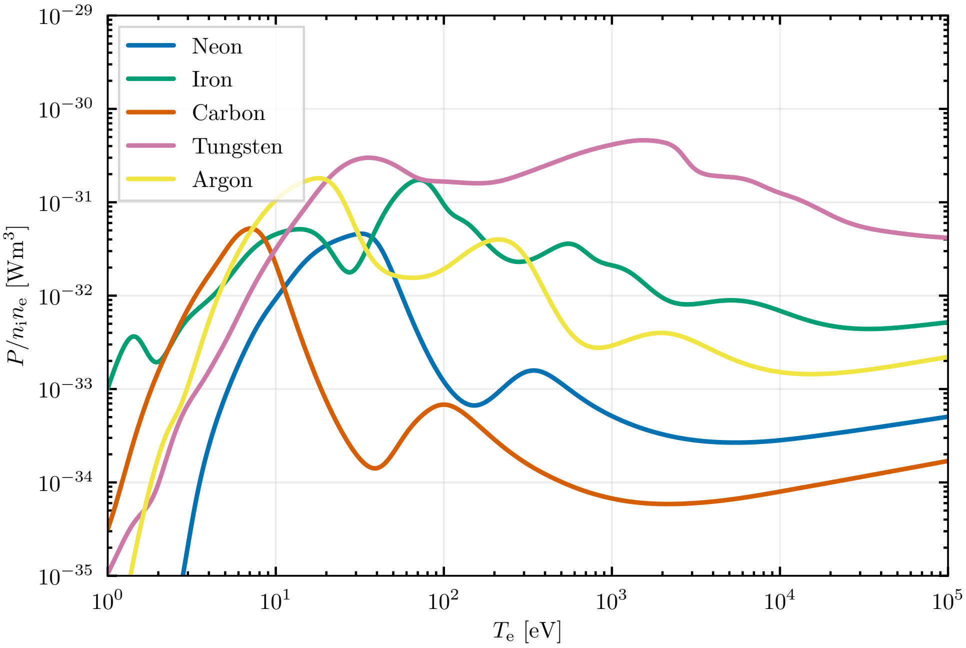

Figure 3.5: The radiation rate in a coronal equilibrium is heavily dependent on temperature and impurity species. The radiation data is obtained via OPEN-ADAS [60].

there is recombination through emission of photons [61, 62]. Systems can be assumed to be in coronal equilibrium as long as the changes in temperature and density are slow enough such that the charge state distribution can evolve with them. This can not happen instantaneously because the distribution is the result of the collisional processes. It typically takes a time of the order of a millisecond for the charge state distribution to equilibrate to local conditions [63, 64]. Since ADAS is used for all impurity radiation, the impurity population is assumed to be in coronal equilibrium. The validity of this assumption will be addressed in section 4.

3.1.6 Limitations of model 501

The main limitations of model 501 for this research are related to the way the impurities are treated. In a real fusion experiment, various impurity types are present in different concentrations, each with its own spatial and temporal evolution. The current model is only capable of handling a single impurity species, which is reflected in the single continuity equation (3.18). This is not necessarily detrimental for this research, because the aim for this work is not to realistically represent a real experiment. Simulations and reality can still be compared as long as the orders of magnitude of the radiation power densities are in line. For a qualitative look at the shape of the radiation curves it is irrelevant whether it is of a single species or a combined curve of multiple. A second simplification is the inclusion of only drift and diffusion in the continuity equations. This means that neo-classical transport and turbulence are inherently not accounted for in the model, while they can be important for the description of particle transport [65, 66]. On the other hand, as soon as anomalous transport gets important, the validity of an MHD description of the plasma ends. Gyrokinetics or full-kinetic codes are then better suited for numerical (transport) studies. Since the Gates-model is described in terms present in MHD, `JOREK` is suitable for testing it. In particular the (local) energy balance is expected to be valid, while some care should be taken with conclusions in which impurity transport plays a role.

3.2 General approach

The first part of this section is aimed to make clear what is changed to `JOREK` to make it suitable for testing the Gates-model. Then some information and motivation is given on which settings are used for the already present and newly implemented parts in the simulations.

3.2.1 Code additions and modifications

An **island finding routine** is designed, implemented in FORTRAN and tested for use as a post-processing tool. In short, it finds the location of the x-point of the user-specified magnetic islands, after which it starts tracing a magnetic field line and creates a Poincaré plot, with which the islands can be visualized. From this data, the width of the magnetic islands can be obtained and used as a quantity for comparing between simulations. A more thorough description of the methods in this tool can be found in Chapter B.

An **impurity addition routine** is implemented in Python to change the impurity concentration in the `JOREK` restart files. In a simulation, this translates to the instantaneous appearance of an impurity type, which is assumed to be instantaneously in coronal equilibrium. Because only ρ_{imp} is changed, the conservation of the total mass density ρ then tells that deuterium ions are exchanged for impurities. The implementation leaves it for the user to decide whether the impurities are added spatially uniform or at a fraction relative to the local total density.

Three new impurity types are implemented in the `JOREK` source code: carbon, iron and tungsten. They can be added through a particle source or with the implementation mentioned above. The radiation functions are obtained from interpolation of ADAS data, see figure 3.5.

The **induction equation** (3.10) **is modified** to have a more physically accurate current source during fast temperature changes. The term $\eta\,(j - j_0)$ is replaced by $\eta j - \eta_0 j_0$. The profile of the newly introduced resistivity η_0 can either be temperature (and thus time) dependent or constant, depending on the user's preference. The need for this change can be seen as follows: a rapid decrease in temperature due to radiation would let the local η grow, which increases the effective current source ηj_0 and with it the Ohmic heating. This would suppress the effect of the cooling, but is not physical. One workaround is to fix the current source at zero ($j_0 = 0$) from the moment impurities are added to the plasma. This is a valid approach for fast processes, but for times on the scale of magnetic island growth (typically > 100ms) causes decay of the current profile. By fixing the total term $\eta_0 j_0$ to a profile defined before the cooling, both the decay and the drive of extra (nonphysical) current are countered.

Table 3.3: Profile coefficients

	Temperature	**Density**	FF'
Center value	Varied	0.1	5.0
Edge value	$0.01 \cdot T_{\text{center}}$	0.1	0.0
C	-0.8	0.1	-1.0

3.2.2 Construction of equilibria

Initial profiles are chosen for the density, temperature and FF' ($= F\frac{dF}{d\psi}$, which will appear in the Grad-Shafranov equation (3.24)). In principle these can have any shape, but in this work the three profiles are all described with

$$y\left(\psi_N\right) = y_{\text{center}} + \left(y_{\text{center}} - y_{\text{edge}}\right) C\psi_N. \tag{3.23}$$

The center, edge and coefficient (C) values for the three profiles are given in table 3.3. With this choice of parameters the profiles are plotted in figure 3.6. The density profile is uniform, which is convenient because the local density will equal the line-averaged density, regardless of integration path. The temperature profile is roughly parabolic in r. With the choice of FF', the toroidal magnetic field is fixed. The combination of the three profiles allows for consistent calculation of the current density profile according to the Grad-Shafranov equation [67]

$$j = \Delta^*\psi = -\mu_0 R^2 \frac{dp}{d\psi} - F\frac{dF}{d\psi}. \tag{3.24}$$

In order to change the macroscopic equilibrium of the plasma, the profiles have to be adjusted. The value of the density will be adjusted by tuning `central_density`. Because this is a parameter used in the normalization, this causes most other parameters to change consistently with it as well, see Appendix C. The temperature of the plasma is scaled by manual adjustment of the central value T_{center}. Whenever the initial temperature profile is adjusted, the resistivity η (not Spitzer) should be scaled with it for consistency. Moreover, the perpendicular heat diffusivity should be changed along T as well, because the Ohmic heating is strongly temperature dependent. This would let the temperature quickly evolve to a different state than desired, if there is no equally large energy sink in the form of transport losses to counter it.

In addition to the initial profiles, the values for several parameters need to be given, most of which remain constant for all simulations. Those are given in table 3.4. The values regarding the grid size and time steps are chosen based on convergence studies, which are shown in Appendix A.

3.2.3 Simulations

Now that the initial conditions and constants are clear, the settings that do vary *during* the simulations need to be defined. To make this more clear, figure 3.7 schematically sketches the different expected phases of a simulation by showing the different types of energies for different harmonics. Initially an axisymmetric system is solved in which the initial profiles are allowed to become self-consistent and flows can evolve. This is the equilibration phase, during which no impurities are present and the current source is free to evolve. This phase ends once the axisymmetric kinetic energy is constant in time. Then an impurity population is added as a fraction relative to the total mass density, the current source profile is fixed in time and more toroidal

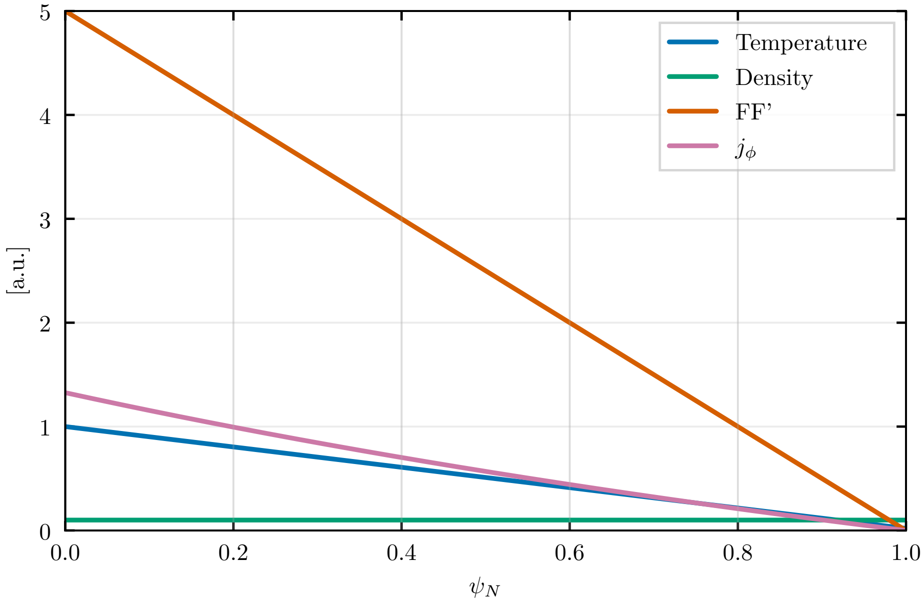

Figure 3.6: The profiles for temperature, density, FF' and current density as a function of the normalized flux ψ_N.

Table 3.4: Simulation settings and parameters

Geometrical parameters	
Poloidal plasma shape	Circular
Major radius R_{axis}	3 m
Minor radius a	1 m
Physics parameters	
Toroidal magnetic field B_ϕ	3.67 T
Viscosity μ	10^{-7} `JOREK` units
Parallel particle diffusivity $D_\parallel$	0.0
Perpendicular particle diffusivity $D_\perp$	10^{-7} `JOREK` units
Heat conductivity ratio $\chi_\parallel/\chi_\perp$	10^8
Simulation parameters	
Number of radial grid elements	126
Number of poloidal grid elements	76
Typical timestep equilibrium and linear phase	100 `JOREK` units
Typical timestep non-linear phase	$0.1 - 10$ `JOREK` units

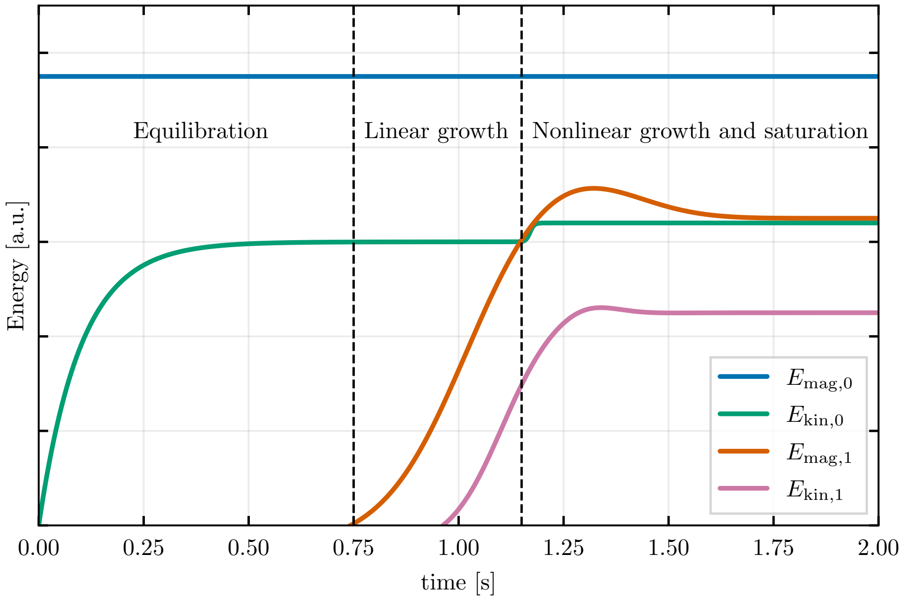

Figure 3.7: A schematic representation of the relative energies (on logscale) during the tearing mode evolution. A simulation run typically consists of an equilibration phase, followed by the linear growth phase and the non-linear phase.

harmonics are included, allowing the tearing mode to grow. The linear growth phase is characterized by the straight slope on the logscale, and can be described using perturbation theory. The amplitude of the mode grows exponentially until it is roughly at the same order of magnitude as the axisymmetric modes. Then, these modes become affected, causing nonlinear effects to emerge and the mode to saturate, possibly after an overshoot. Typically the nonlinear phase is most difficult to solve and will need smaller time steps for convergence.

3.2.4 Data analysis and post processing

After the simulation, the raw data is converted into several quantities which can give insight in the comparison with the Gates-model and the empirical Greenwald limit. Radial temperature and current density profiles can help identify the island growth and events related to disruptions, as in 1.7. On top of this, the Ohmic heating and radiative cooling terms give information on the local power balance, providing an explanation on changes in the profiles. Spatial integration of velocities or magnetic field components gives the kinetic or magnetic energies respectively. Decomposed into their harmonic components, these will give information about the evolution of the tearing mode, as in 3.7. Finally, Poincaré plots of the magnetic islands and their width are calculated to visualize and quantify the coupling between tearing mode growth, local heating/cooling and disruption characteristics. The details on this routine are found in Appendix B.

4. Results

In this chapter the presented results are divided in different sections, each building forth on the previous results. For aspects specifically relevant to the interpretation of the results, a short discussion is given alongside. At the end of this chapter, a more general discussion regarding overarching aspects and an extrapolation are given.

4.1 The tearing mode

For the simulations presented in this section a uniform, flat density (ρ) profile is chosen to remove ambiguity in the value of the line-averaged electron density. Electron densities of $0.5, 0.6, 0.7$ and $1.0 \times 10^{20}\mathrm{m}^{-3}$ have been used. The simulations have been initially run for electron temperatures $T_\mathrm{e} = 50, 100, 250, 500$ and 1000 eV. Only results of the first four are used, as for the latter the tearing mode has not been found to be unstable in the used equilibria. For high temperatures this behavior can be explained by the `JOREK` resistivity being adapted such as to follow the $-3/2$-scaling with temperature. The temperatures at the $q = 2$ surfaces are approximately 40-50% of the central temperature values.

4.1.1 Energies and growth rates

Figure 4.1 shows the decomposition of energies for a simulation in which the tearing mode is found to be unstable. It agrees with the conceptual picture of the different phases of the evolution of a mode. After the axisymmetric quantities and thus energies (subscript 0) are in steady state, the components with a dependency on toroidal angle are initialized at an arbitrary low noise level and included in the calculations. An unstable mode should be able to emerge from this state, as is seen here when it grows in the linear phase. Only the lowest two toroidal harmonics of a Fourier decomposition are included for the toroidal dependency. This means that the energies with subscript 1 may contain all modes with periodicity $m/1$, so only $m/1$-islands can exist in the simulations. A convergence scan over the toroidal harmonics included in the simulations is given in Appendix A.

During the linear growth phase, ranging from approximately $t = 0.85\,\mathrm{s}$ to $t = 0.94\,\mathrm{s}$, the effects on any axisymmetric component are negligibly small. Once this coupling becomes significant, the equilibria profiles will be affected by the growing mode and the nonlinear phase starts. This is typically the point at which `JOREK` gets more computationally costly and smaller timesteps up to a factor 100 are needed. After an overshoot of the energies the mode settles to an approximately constant value at times $t > 0.99\,\mathrm{s}$. In this quasi-saturated state the magnetic energy slowly increases, this time over vastly larger timescales. In the remaining part of this report the focus will be on the initial overshoot because it contains the nonlinear growth of magnetic islands and all important aspect of the Gates-model, as will be shown later on.

A verification that the tearing modes agree with the theoretical description is shown in figure 4.2, where the $-9/10$-scaling of the growth rate with electron temperature is found. The data for this plot is obtained by fitting a straight line to the $E_{\mathrm{mag},1}$ curve during the linear growth phase in figure 4.1. Since magnetic energy scales with the strength of the magnetic field squared, the square root of the growth rate from the fit is taken. This is then repeated for the whole set of simulations, including the scan over impurity concentrations. The impurity concentrations in the plot have no relevance in this part yet, but help to give order to the figure. The outliers in the plots can be related to cases in which high radiation causes the macroscopic profiles

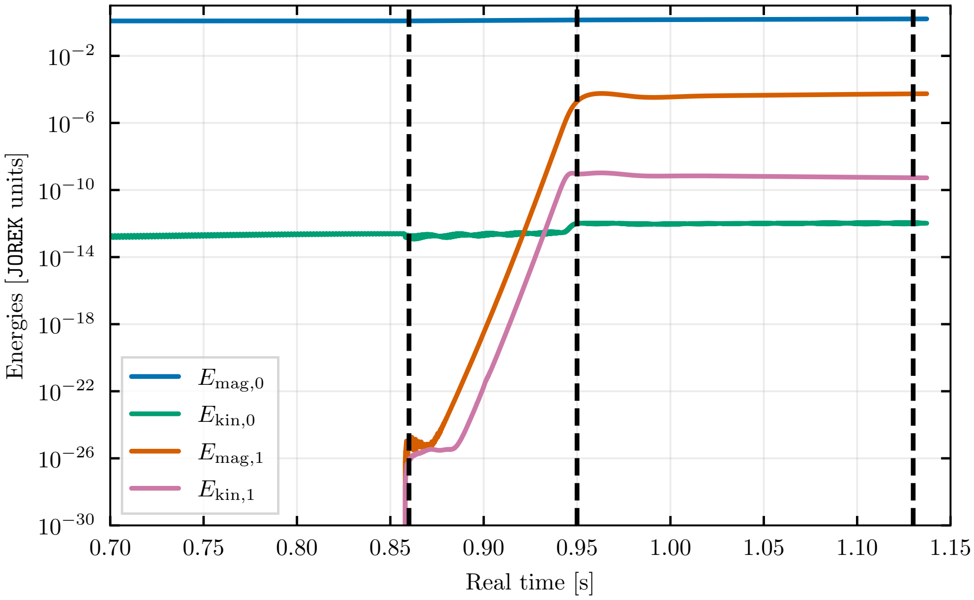

Figure 4.1: For a simulation with $n_\mathrm{e} = 0.7 \times 10^{20}$ m^{-3} $\approx 1.14\ n_\mathrm{G}$ and $T_\mathrm{e} = 100$ eV the different phases of the tearing mode evolution are distinctly visible and show similarity with the expected behavior. The black dashed lines correspond to the times at which the profiles are examined in figures 4.3 and 4.4.

Table 4.1: Coefficient of determination values for the fits in figure 4.2 indicating the 'goodness' of the fits.

Impurity concentration	R^2
0.0 %	0.96
0.1 %	0.96
0.5 %	0.87
1.0 %	0.38

to be altered such as to influence the tearing mode growth. Specifically the drop in temperature causes the resistivity to rise, thereby enlarging the effect of island growth during the linear phase.

The agreement between the data and theoretical scalings is quantified by calculating the coefficient of determination R^2 for each impurity concentration. The values are shown in table 4.1 and show that especially for low impurity concentrations there is good agreement indicated by a value of R close to 1. The two highest values found with 1.0% neon, the outliers from before, are not included in the fit. This result indicates that the `JOREK` resistivity is scaled sufficiently well with respect to the temperatures over multiple simulations. This gives confidence that the simulations are consistent with respect to each other and that they can be directly compared in further sections. The impurity concentrations have a far lesser impact on the linear phase of the growth rate than the temperature does. This is explained by the fact that the resistivities are manually chosen at the start of the simulation, before impurities are added. No information about n_imp is thus taken into account in the scaling.

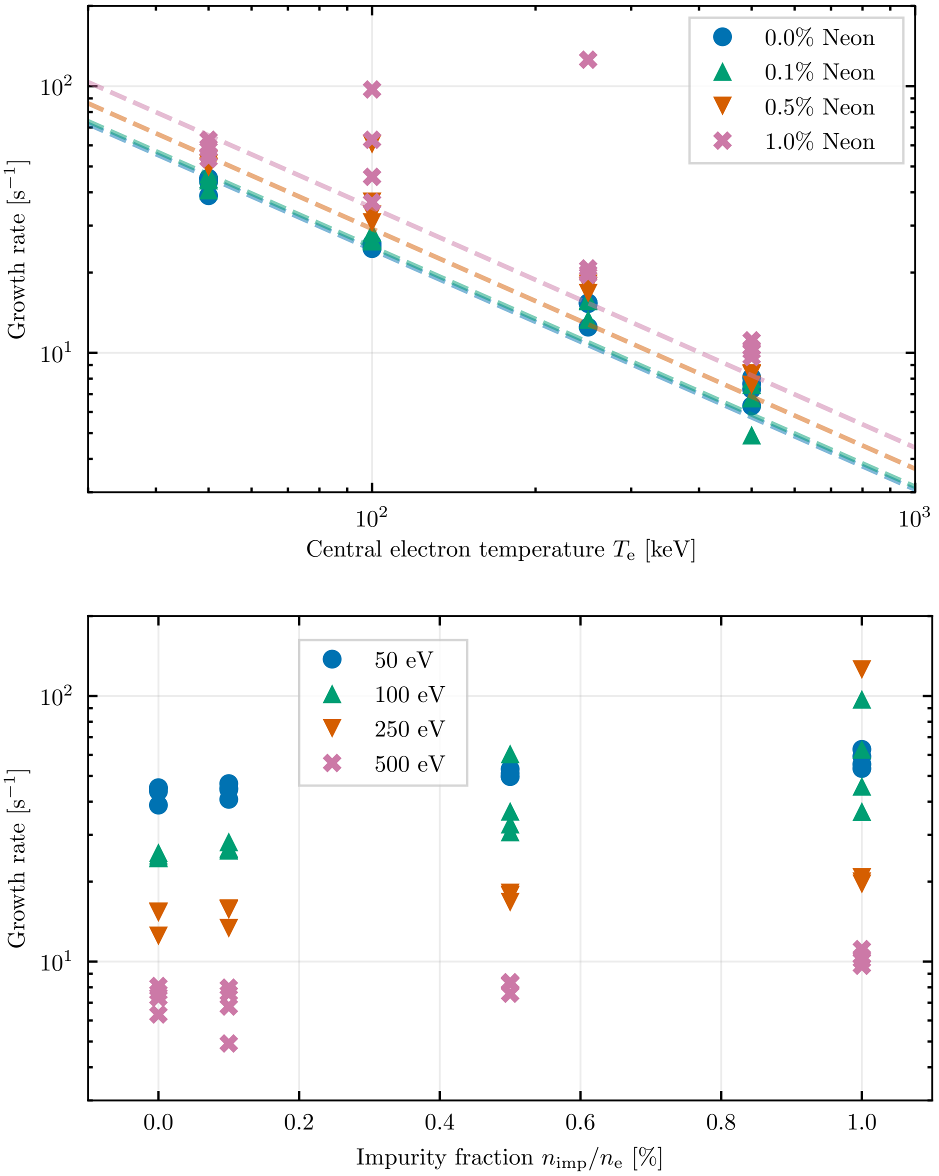

Figure 4.2: For different temperatures T_e, densities n_e and impurity densities n_imp, the growth rate during the linear phase is calculated using a least squares fitting method. Each marker represents a simulation. Despite the range in densities, the data has a similar trend to the theoretical temperature scaling of $-9/10$. Outliers can be related to cases in which high radiation causes the initial profiles to be altered so much as to significantly alter the tearing mode growth. The effect of impurity concentration on the growth rate is comparably small. The dashed lines in the top plot are linear fits with $T_\mathrm{e}^{-9/10}$-scalings of which the coefficient of determination R^2 is calculated.

4.1.2 Magnetic islands

In this section the focus will shift to the evolution of the macroscopic profiles in the nonlinear phase and the relation of magnetic island to them. Specifically the temperature profile is of interest because changes in energy confinement should be visible in it and islands with a significant size should cause temperature flattening as explained in the theory. The current density is looked at for its clear showing of a perturbation and its link to Ohmic heating. For three times indicating start of mode growth, maximum of nonlinear growth and saturated state, the poloidal cross sections for both quantities are given in figure 4.3. During the linear growth phase no changes in macroscopic profiles are seen, which is conform expectations. At the end of the nonlinear phase the perturbations in the profiles become visible, which evolve to their final state. On top of the temperature are Poincaré plots of the $^2/_1$-islands, which are made using the methods described in Appendix B. Not the full islands are shown as can be inferred from the lack of an X-point. Rather the flux surfaces close to (but inside) the separatrix are found. Still these give a good indication of the size and location of the full structure.

In the current density the changes between phases are distinct and the footprint of a $^2/_1$-island can be seen in the local minima that emerge. The value of j in the center of the plasma increases as the perturbation rises, this is called 'current peaking'. This causes the Ohmic heating and therefore the temperature in the center to increase. As time progresses, the perturbation is seen to be shifting radially outwards, which is the direct effect of the larger current in the center altering the q-profile and thus the location of the $q = 2$ surface.

In the temperature plots the perturbations are less apparent, because the flattening is a relatively small effect compared to the current perturbation. Additional insight can be found when looking at the profiles along the black lines that intersect the projection of the islands at their widest points. This is visualized in figure 4.4. Here the temperature shows an evolution that results in full flattening in the saturated case, which means that the width of the island satisfies the Fitzpatrick width w_C. This in turn means that for the choice made for $\chi_\parallel/\chi_\perp$ the center of the islands at these widths can be approximated as thermally isolated regions. Moreover, the width of the magnetic islands is then approximately equal to the width over which the temperature is flattened. Looking closely at the outer side of the flattened region, a small increase is seen as result of the increased Ohmic heating at the outside of the magnetic islands.

Now the width of the magnetic islands obtained from the Poincaré plots is considered, resulting in a maximum width as function of time in figure 4.5. This plot shows the width in terms of normalized poloidal flux ψ_N and normalized spatial distance, transformed as if the widest part would lie on the midplane, so that flux surface geometry and island rotation in the poloidal plane does not play a role in comparisons. Details are again found in Appendix B.

The temporal behavior of the maximum width agrees with figure 4.1 when comparing the nonlinear phases during which the islands have a finite width that the tracer can detect. At identical times the overshoot and start of saturation are found. Together with the visual observations in the poloidal cross sections and profiles, it can thus be concluded that the energies of the non-axisymmetric modes are due to the formation and growth of the $^2/_1$-islands. In general, the q-profile during the simulations will range between 1.4 on the axis to 3.7 at the plasma edge. This means that modes with a $^{3}/_{1}$ periodicity can be present as well in the simulations, as will be seen later on. However, the islands found here are generally largest, dominant in perturbing the equilibria and will be used in the further analysis. The maximum island width during the overshoot in the nonlinear phase will be regarded as figure of merit in the comparison of different cases.

The fluctuation in the found width, especially clear during the saturated phase, is an artifact of the island finding routine. It originates from the difficulty to exactly locate the spatial position of the X-point. As a consequence, flux surfaces that are inside the island's separatrix are traced. This is also apparent in the varying distance between the 'end-points' of the islands in figure 4.3. In Appendix B a scan over this separation shows that the island width is underestimated typically by a few percent, which is sufficiently small for the qualitative comparisons in this thesis.

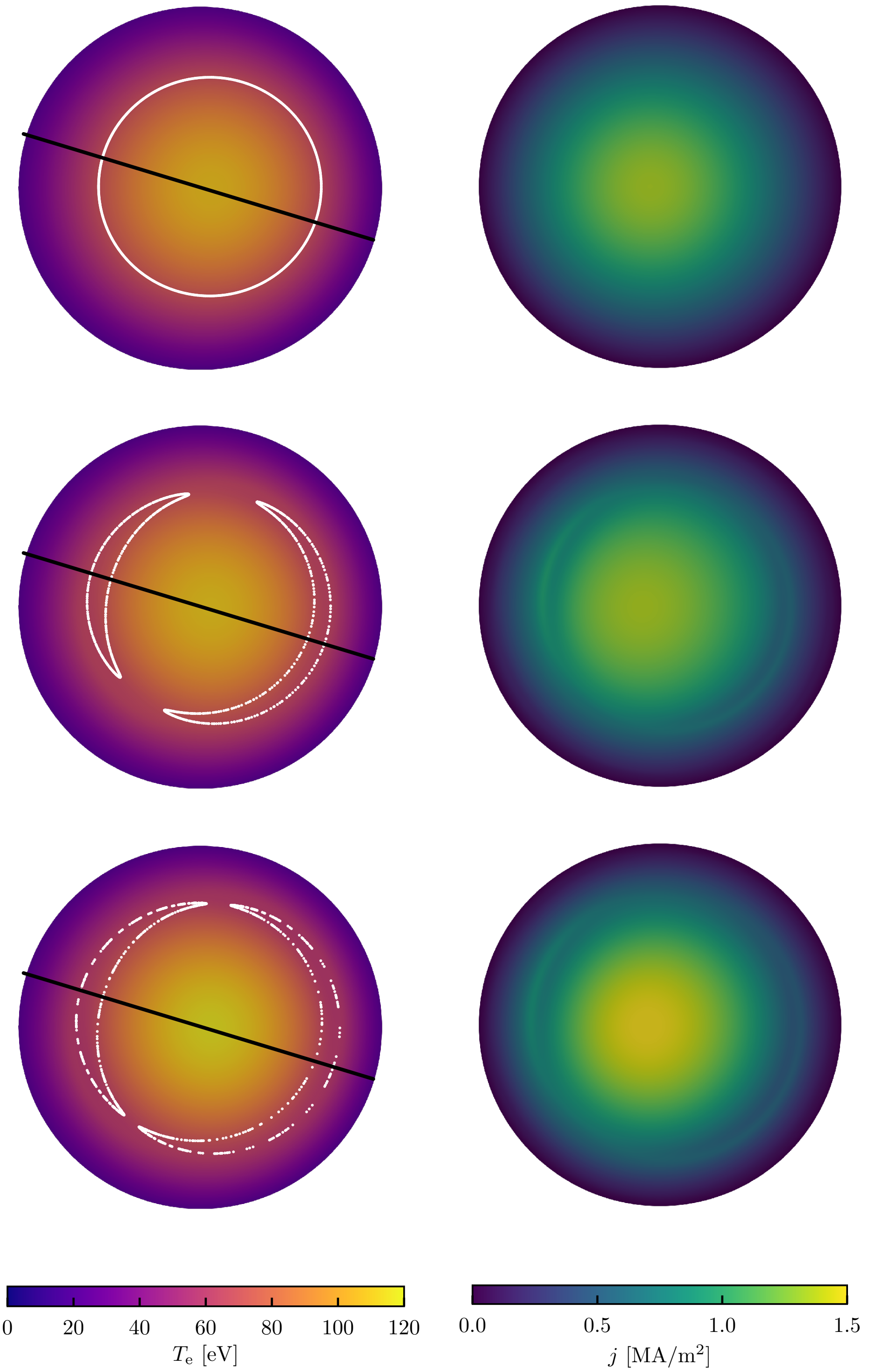

Figure 4.3: The electron temperature T_e and toroidal current density j at different times (top $t = 0.86\,\mathrm{s}$, center $t = 0.95\,\mathrm{s}$, bottom $t = 1.13\,\mathrm{s}$) corresponding to the plasma before the tearing mode, at the start of the nonlinear phase and during the saturated state. Superimposed on the temperature profile are a Poincaré plots of the $^2/_1$ magnetic islands (white) and the line over which the profiles are plotted in figure 4.4 (black).

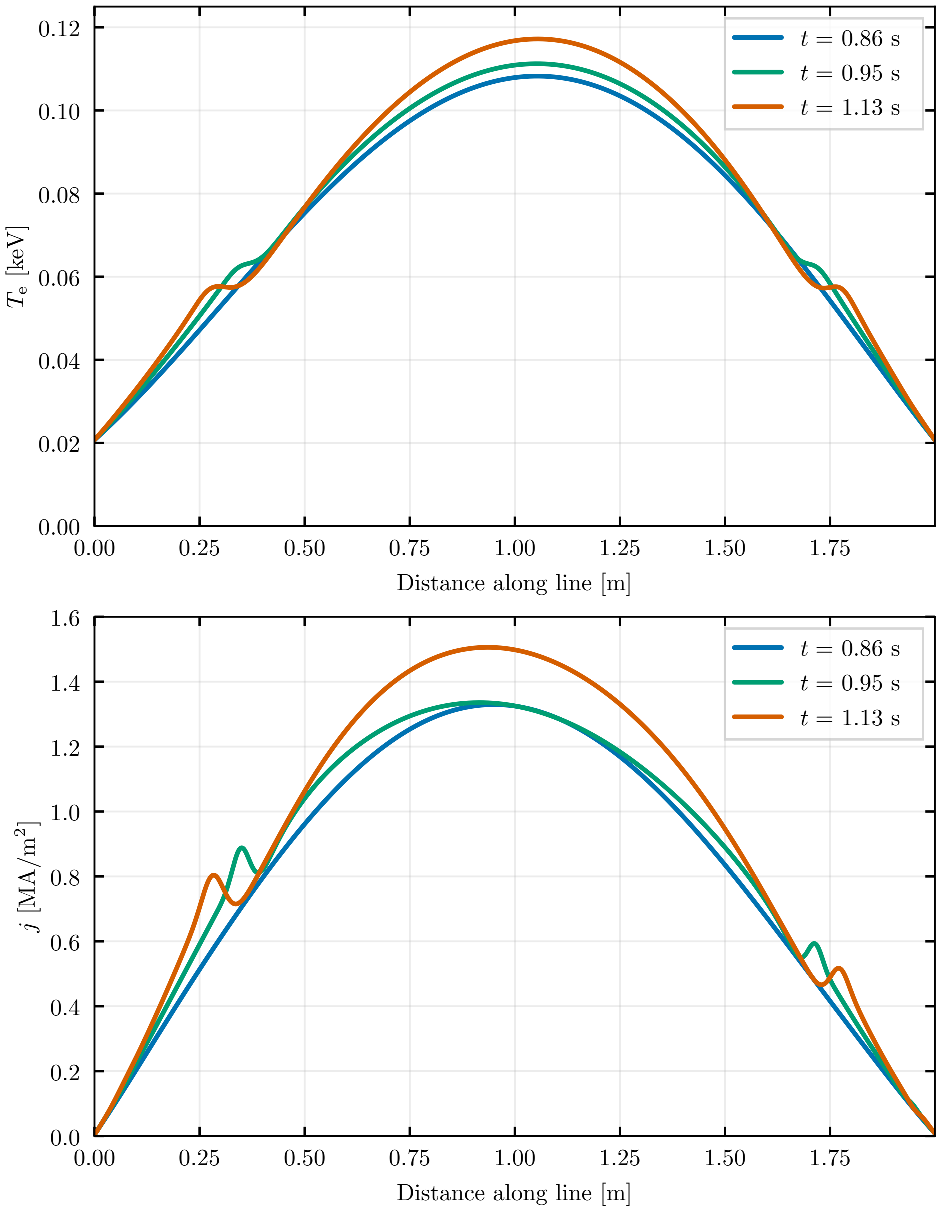

Figure 4.4: The current density (top) and electron temperature (bottom) profiles are obtained over a line in the poloidal plane (see figure 4.3) that intersects the islands approximately at their largest width. At approximately 0.35 and 1.7 on the horizontal axis, the perturbations in the current density are visible, where the location of the local minimum corresponds to the center of the island. Over the island width the temperature profile is flattened, indicating that parallel heat transport dominates. In the center of the plasma, the current peaks as the tearing mode grows.

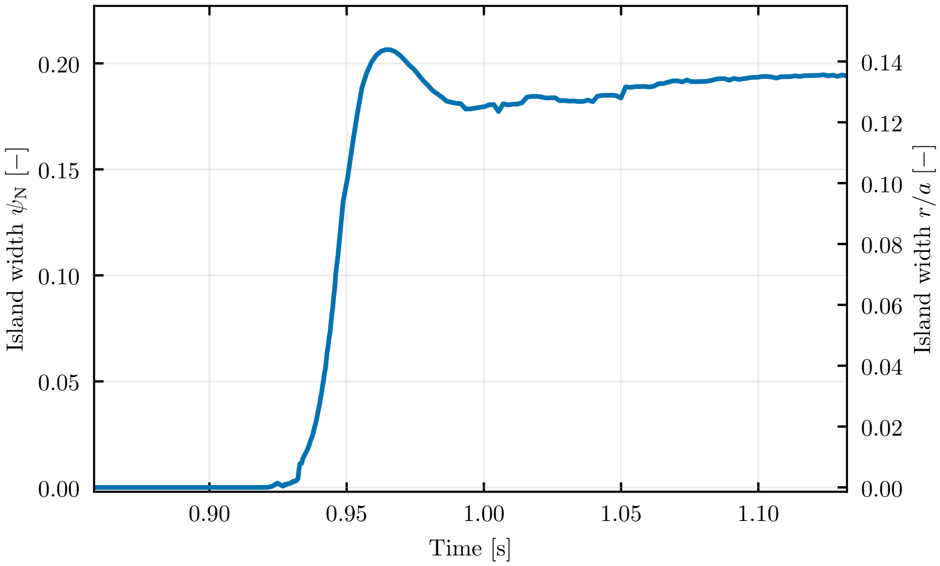

Figure 4.5: The maximum width of the magnetic islands is calculated using the island finding routine described in Appendix B. It is converted to the midplane width and given in units of normalized poloidal flux ψ_N and normalized real width r/a to allow for direct comparisons between different cases.

4.2 Testing the Gates-model

Now that the islands are observed along with the perturbations in the macroscopic temperature and current density profiles, the mechanism of enhanced island growth under radiative cooling from the Gates-model will be tested.

4.2.1 Impurity addition, transport and radiation

For the previously mentioned temperatures and electron densities, the impurities are added in concentrations of $0.1, 0.5, 0.75$ and 1.0%. This is done relative to the electron (number) density by scaling `JOREK` variable ρ_imp at a fraction of ρ, leaving the latter unaltered. This addition is not comparable to any physical process, but ensures the desired concentrations around the $q = 2$ surface. If other methods of addition such as Shattered Pellet Injection (SPI) or Massive Gas Injection (MGI) were used, particle transport would need to be included in the analysis. The choice is made to keep this out of the scope of this research.

Because of the uniformity in both the ρ and ρ_imp profile, particle transport is low. Combination with the addition method leads to the assumption that impurities happen to be present around the $q = 2$ surface at the time of the tearing mode growth.

For the majority of simulations neon will be used as impurity species, of which the coronal radiation curve is already given in figure 3.5. In principle results similar to the ones in this thesis are expected to be found for any impurity type, if only scaled with a different fraction. This is because the product $f_\mathrm{imp}L_\mathrm{rad}$ is the contributing factor in the energy balance. For example, the radiation due to 1% neon or 0.01% iron is approximately equal at 100 eV. The derivatives of the radiation with respect to temperature do vary between species and can be important for nonlinear effects.

4.2.2 Demonstration of the mechanism

The purpose of this section is to demonstrate the enhanced growth of the magnetic islands at densities above the Greenwald density. The parameter scans go over the three variables T_e, n_e and n_imp, where the latter signifies the importance of the radiative cooling. The maximum island width as a function of time is shown in figure 4.6 for a central electron temperature of 100 eV. The maximum island width increases significantly if both densities are increased. This effect becomes significant around the Greenwald limit as islands start to grow significantly faster and to larger widths for increased impurity contents. This behavior is similar to the electron density scan in [40], but here the dependence on n_imp is made explicitly clear. Increasing the density even further to values 21% and 72% above n_G leads to explosive island growth to widths in the range of 20%-50% relative to the minor radius. The growth typically takes place within 10 ms. As a reference, analysis of JET, ASDEX-Upgrade and COMPASS shows a critical island width for triggering a thermal quench around 30% [68]. Early termination of some curves is caused by presumably numerical instabilities during the simulations, where growing oscillations in the current density around the magnetic axis are found. A possible cause may be the fixed current source term in the induction equation 3.10. In the discussion a recommendation will be given for improvement of `JOREK` and hopefully prevention of these issues. At the time of termination, the found width is already well above the maximum widths for lower impurity concentrations, with a positive derivative indicating further growth.

The fluctuations in the curves can again be explained by the tracer failing to precisely determine whether the approximate location of the x-point is within or outside of the islands. On the other hand, this effect shows that the approximate error in the width is always found to be smaller than the enhanced growth effect.

The large jumps in vertical width, especially found for fractions of 0.75% and 1.0%, are related to the transition to a stochastic regime and the tracer sometimes finding both the $^3\!/_1$ and $^2\!/_1$-islands. This is better visualized in the Poincaré plots of the magnetic islands from which the width is initially derived. Figure 4.7 shows the different stages of the enhanced island growth for parameter settings of $n_\mathrm{e} = 0.7 \times 10^{20}\ \mathrm{m}^{-3} \approx 1.14\ n_\mathrm{G}$, $n_\mathrm{Ne}/n_\mathrm{e} = 0.01$ and $T_\mathrm{e} = 100$ eV. The first two times are selected to represent the linear growth phase where there is no observable island width and the nonlinear growth phase in which the islands have a finite width and are well defined. Further into the nonlinear regime first signs of stochastisation occur in which the separatrix is not found to be smooth and small radial excursions are made. This leads to the x-points being not as sharply defined in the Poincaré representation. At the final stages, full stochastisation is seen where a coupling is created between magnetic islands. Whenever this happens the radial excursion of a magnetic field line is larger than when only the stochastic region around the initial islands are found, which explains the variation in found widths.

Besides these jumps, the stochastisation and coupling explain the flattening of the temperature profile over a large radial distance, which will be discussed in section 4.3.1. Given that the energy transport along magnetic field lines is much faster than across, the radial excursions of the field line flatten the temperature profile and provide a shortcut for the energy transport.

To allow the comparison of the island growth at different temperatures, the temporal information needs to be removed by regarding only the maximum island widths found during the nonlinear growth of the tearing modes. This then allows for direct comparison of all three parameter scans, shown in figure 4.8.

The main result from these plots is that the rapid growth of islands only occurs for specific temperatures and densities, with the case at $T_\mathrm{e} = 100\,\mathrm{eV}$ being the most apparent. In contrast to earlier work on the Gates-model, a large dependency on density, temperature and impurity type is found.

When closely comparing the data there is consistency to be found between the different impurity concentrations. The island widths grows substantially larger at the high densities at 100 and 250 eV. For these cases the enhanced growth is indeed observed. The color scaling is chosen to saturate at a value of 0.3, since island widths above this value show large variations due to stochastic behavior, which are irrelevant for this figure. Besides that, the presented scale shows a more subtle effect for temperatures of 50 and 500 eV. Here, the maximum found width is actually smaller than for the case with little or no impurities. According to the Gates-model this may happen when heating inside the islands is enhanced. A comparison run with iron as impurity species shows the mechanism to be present at central temperatures of at least 250 eV.

In the simulations related to the data points with crosses through them, termination happened before the maximum island width is reached, such for the case with 0.75% neon at $n_\mathrm{e} = 0.7 \times 10^{20}\ \mathrm{m}^{-3}$ in figure 4.6. If assumed that these would have grown to a substantial width, then a structure emerges for the runs with 0.5%, 0.75% and 1.0%.

Before looking more specifically at the effect on the temperature profile, an attempt is made to couple the observed behavior to the explanation and mechanisms given in the Gates-model in the following section. The difference in qualitative behavior between the impurity types will be addressed there as well.

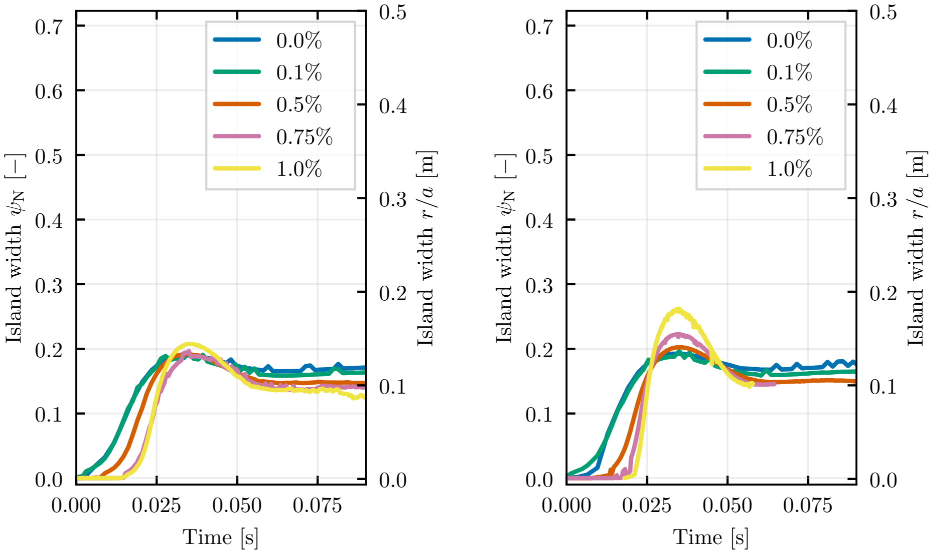

(a) $n_e = 0.5 \times 10^{20}$ m^{-3} ≈ 0.86 n_G **(b)** $n_e = 0.6 \times 10^{20}$ m^{-3} ≈ 1.04 n_G

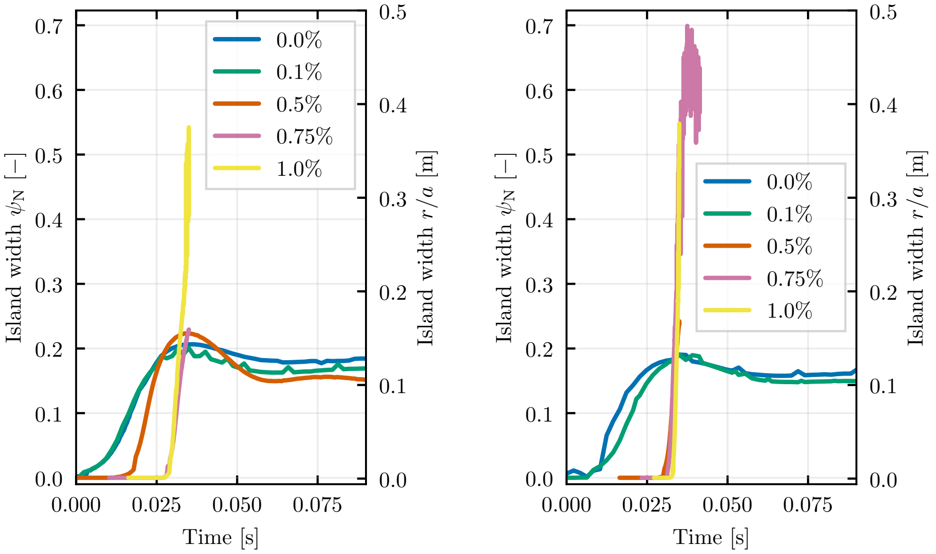

(c) $n_e = 0.7 \times 10^{20}$ m^{-3} ≈ 1.21 n_G **(d)** $n_e = 1.0 \times 10^{20}$ m^{-3} ≈ 1.72 n_G

Figure 4.6: For five neon fractions and four different electron densities, both below and above the Greenwald density n_G, the maximum widths of the $^2\!/\!_1$-islands are given as a function of time. Islands with a sufficient impurity and electron density concentration grow drastically faster and to larger sizes. Especially for the two largest electron densities a threshold behavior is observed where the islands stay bounded for low impurity concentrations or grow to sizes of 20% to 50% of the minor radius. The sudden termination of the curves for impurity fractions larger than 0.75% in the bottom two plots is caused by numerical instabilities in the `JOREK` simulations due to large temperature changes in the plasma.

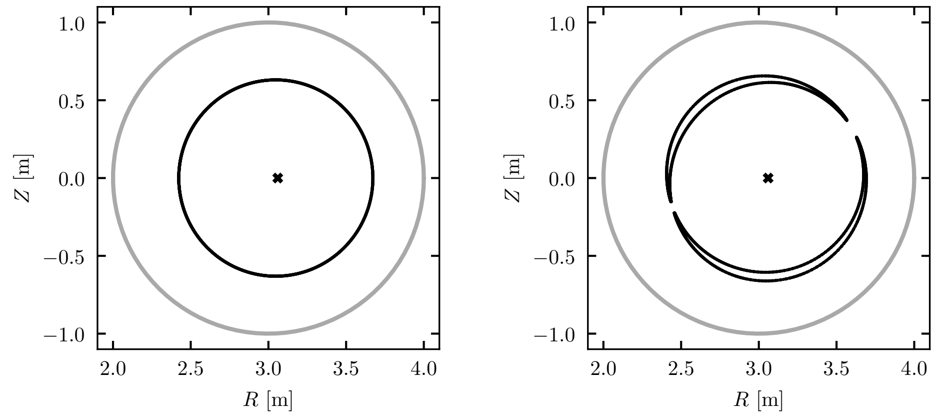

(a) Linear growth

(b) Nonlinear growth

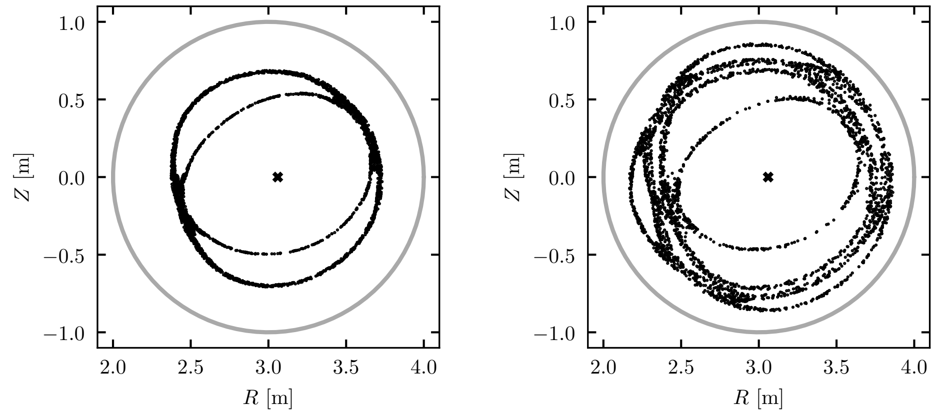

(c) X-point stochastisation

(d) Full stochastisation

Figure 4.7: Magnetic islands grow drastically in size leading to the termination of the simulation with $n_\mathrm{e} = 0.7 \times 10^{20}\ \mathrm{m}^{-3} \approx 1.14\ n_\mathrm{G}$, $n_\mathrm{Ne}/n_\mathrm{e} = 0.01$ and $T_\mathrm{e} = 100$ eV. Poincaré plots close to the $q = 2$ surface shows four distinct phases in the evolution. During the nonlinear growth phase the islands get a finite width and can be detected. At later times the field line starts to show stochastisation, which is seen mainly near the X-points. Coupling between $^2\!/_1$ and $^3\!/_1$-islands is observed at the end of the simulation.

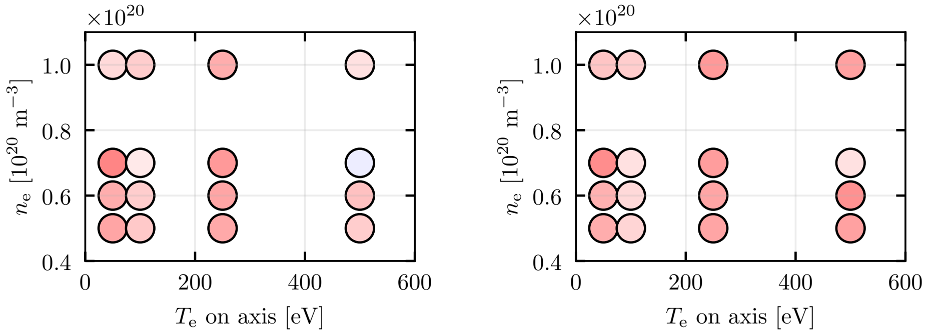

(a) 0% Neon

(b) 0.1% Neon

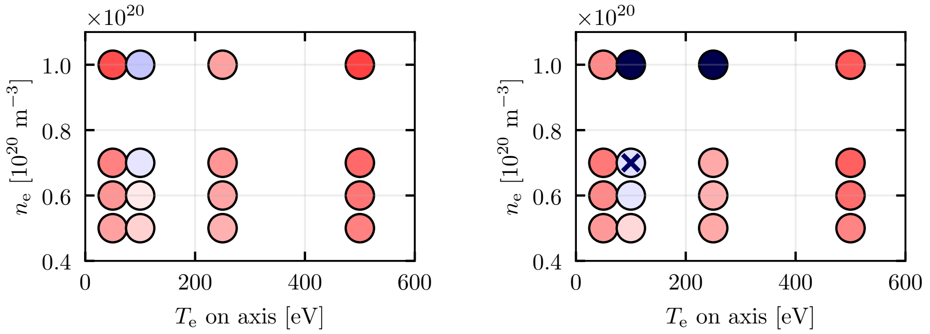

(c) 0.5% Neon

(d) 0.75% Neon

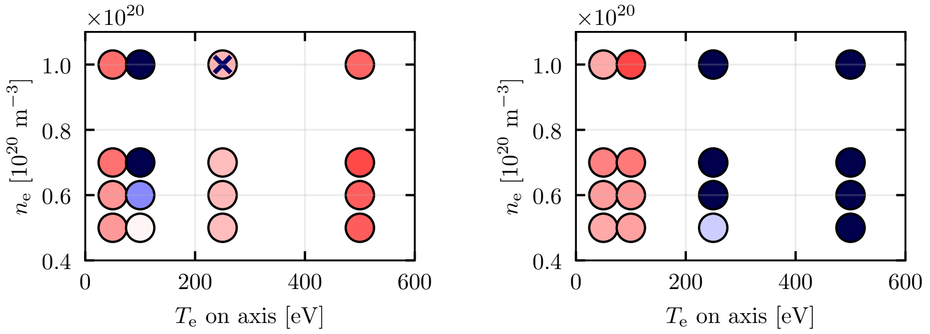

(e) 1.0% Neon

(f) 0.1% Iron

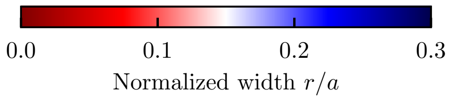

Figure 4.8: The maximum island width is given for all simulations, covering the scans over electron temperature, electron density and impurity fraction. The color scale is chosen such that the transition from net cooled to net heated islands is distinctly visible. Simulations that were terminated early while the island had not yet reached a maximum width are indicated with a cross.

4.2.3 A new look at the F-function

This section is aimed to relate the local conditions that allow for the growth of radiative islands according to the Gates-model to a formulation of the Greenwald density limit with local quantities. For this a formulation will be used, from here on called the F-function, which is introduced in [69], but also used in analysis of the Gates-model in [37], [39] and [35]. In these works its relative independence on temperature and impurity density is used as argument for the robustness of the Greenwald density limit and its lack of dependence on these parameters. In this thesis, F will be used in an opposing way to explain the dependencies found in the previous section.

The F-function is obtained by assuming the island to be thermally insulated by its separatrix. Now only two terms are important in the local power balance: the Ohmic heating

$$P_\Omega = \eta_{\mathrm{Sp}} j^2 \qquad = \frac{\sqrt{2m_\mathrm{e}} Z_\mathrm{eff} e^2 \ln\Lambda}{12\pi^{3/2}\epsilon_0^2 T_\mathrm{e}^{3/2}} \cdot \frac{1 + 1.198 Z_\mathrm{eff} + 0.222 Z_\mathrm{eff}^2}{1 + 2.966 Z_\mathrm{eff} + 0.753 Z_\mathrm{eff}^2} j^2, \tag{4.1}$$

[41] and the radiative cooling

$$P_\mathrm{rad} = n_\mathrm{e} n_\mathrm{imp} L_\mathrm{imp} = n_\mathrm{e}^2 f_\mathrm{imp} L_\mathrm{imp}. \tag{4.2}$$

Equating these two terms, an expression for the local quantities inside the magnetic island is obtained:

$$n_\mathrm{e}\ \left[10^{20}\mathrm{m}^{-3}\right] = Fj\ \left[\mathrm{MA\ m}^{-2}\right], \tag{4.3}$$

where

$$\begin{aligned} F &= 10^{-14}\sqrt{\eta/(f_\mathrm{imp} L_\mathrm{imp})} \\ &= 10^{-14}\sqrt{\frac{\sqrt{2m_\mathrm{e}} Z_\mathrm{eff} e^2 \ln\Lambda}{12\pi^{3/2}\epsilon_0^2 T_\mathrm{e}^{3/2}} \cdot \frac{1 + 1.198 Z_\mathrm{eff} + 0.222 Z_\mathrm{eff}^2}{1 + 2.966 Z_\mathrm{eff} + 0.753 Z_\mathrm{eff}^2} \cdot \frac{1}{f_\mathrm{imp} L_\mathrm{imp}}} \end{aligned} \tag{4.4}$$

is the function of interest in this section.

External heat sources P_ext can be included in this derivation, for which the balance can be rewritten as

$$n_\mathrm{e} = \sqrt{\frac{1}{f_\mathrm{imp} L_\mathrm{imp}} (\eta_{\mathrm{Sp}} j^2 + P_\mathrm{ext})}. \tag{4.5}$$

If the external source is scaled with the Ohmic heating as $P_\mathrm{ext} = \alpha P_\Omega$, an expression similar to (4.3) comes out:

$$n_\mathrm{e}\ \left[10^{20}\mathrm{m}^{-3}\right] = F^* j\ \left[\mathrm{MA\ m}^{-2}\right], \tag{4.6}$$

with $F^* = \sqrt{1+\alpha} F$.

The formulation of (4.3) is similar to the global formulation of the Greenwald density limit (1.7). For a value of $F = 1$ the local electron density and current density satisfy an identical expression as the averaged quantities of the global limit do. In formulation (4.4) there is an explicit temperature dependence through the Spitzer resistivity and an implicit one through the radiation rate L_{rad}, see figure 3.5. The impurity density is directly present through the impurity fraction f_{imp} and indirectly through the effective charge state of the plasma Z_{eff}. For different impurity concentrations and types, F is given as a function of T_{e} in figure 4.9. A significant dependency on temperature, impurity type and fraction are seen, as is expected from equation 4.4, but again in contrast with literature. There are regions of a few hundred eV for which the curve shows plateauing, especially for iron, but show large variance on the range of reactor-relevant temperatures: typically on the order of 0.1 to 1 keV, and even higher (>10 keV) for future devices such as ITER.

In order to further investigate the effect of impurity fraction on the density limit, the values of F at $T_{\mathrm{e}} = 1\,\mathrm{keV}$ is plot in figure 4.10. On the horizontal axis is the multiplication factor of the impurity fractions used in figure 4.11. As a reference, the values at which the global density limit is found in the Gates model are shown [39], together with a scaling that goes with $f_{\mathrm{imp}}^{-1/2}$ that would be expected if Z_{eff} would be fixed in equation 4.4. For sufficient high impurity fractions the value of F falls of slower than the given scaling and becomes insensitive to impurity concentration. This is observed in both the data from the Gates-model and all presented impurity species except tungsten. At higher concentrations ($> 0.005\%$) this curve saturates to a fixed level as well.

Figure 4.11 shows the result of having more than one impurity species on the local heat balance. At each temperature the value of the function is determined mostly by the lowest, and thus strictest, impurity species. For specific combinations such as the one given here, the individual F-curves can complement each other, creating temperature regimes spanning an order of magnitude where plateauing happens around $F \approx 1$. For such a regime in which F is close to unity, it can be left out of equation (4.3), in which it becomes a direct reflection of the empirical Greenwald limit (1.7), but with averaged coordinates replaced by local ones. Besides the local variations and local extrema, the underlying $T_{\mathrm{e}}^{-3/4}$ scaling of equation (4.4) emerges on the large scales, which is a direct effec of the Ohmic heating being more effective at low temperatures.

Apart from looking for similarities in local and global conditions, i.e. where $F = 1$, the plots can also be interpreted as a boundary between net cooled and net heated parts of the plasma, under the assumption that P_{Ω} and P_{rad} dominate the heat balance. For values of $n_{\mathrm{e}}/j < F$, these parts are net heated and temperature will typically increase. Values above F are net cooled and will have a drop in local temperature. In this way the ratio n_{e}/j can be seen as the relative importance of radiation with respect to the Ohmic heating.

The assumption that energy transport is negligible should hold best at the O-points of the magnetic islands. At these locations data in the form of $(T_{\mathrm{e}}, n_{\mathrm{e}}/j)$ is retrieved from `JOREK` for the runs with 1% neon and 0.1% iron. With this data at multiple consecutive times in the nonlinear regime, a trajectory is obtained and plotted alongside the F-functions in figure 4.12. Of special interest are the curves that intersect with the F-function, transitioning from a heated to a cooled regime. After crossing the curve, a runaway effect happens as current is expelled and temperature is rapidly lost from the island. This behavior is absent for curves corresponding to lower densities that do not cross the F-function. The cases that show the runaway effect correspond to the ones for which in figure 4.8 the largest widths are found.

The trajectories of figure 4.12 show an interplay of radiative cooling, heat transport and growth of the tearing mode. Firstly, all trajectories evolve toward lower tem-

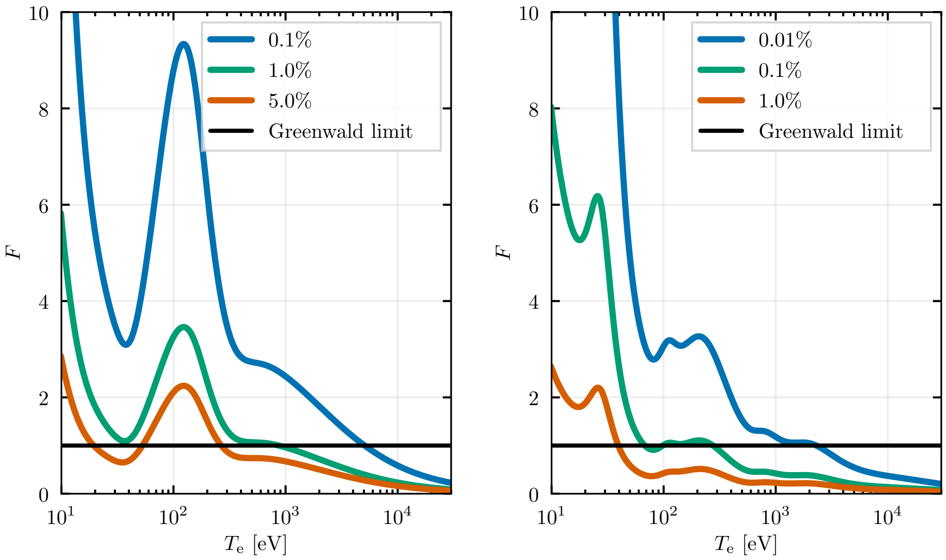

(a) Neon **(b)** Iron

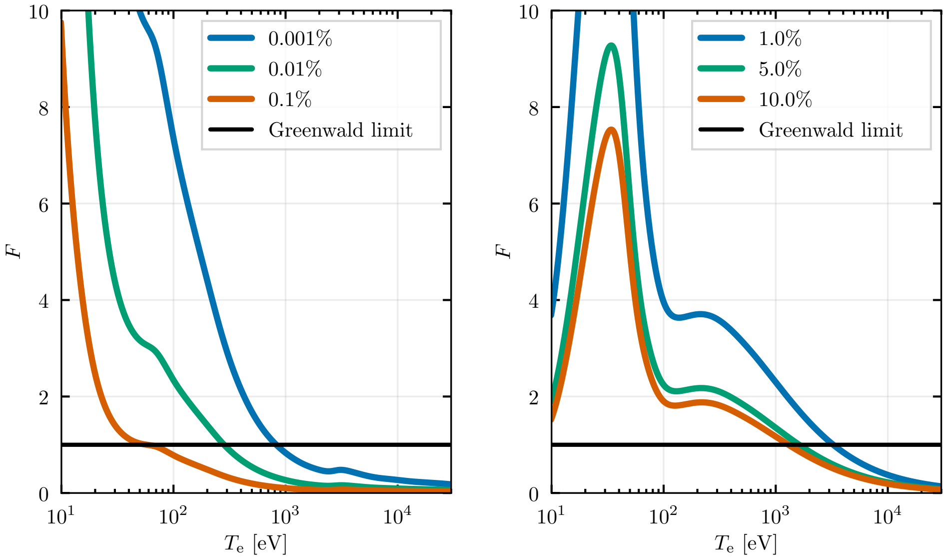

(c) Tungsten **(d)** Carbon

Figure 4.9: The F-function separates isolated regions that are net heated ($n_e/j < F$) and net cooled ($n_e/j > F$). It is plotted here for different species over a range of fractions. The function has a strong dependence on impurity type, fraction and electron temperature.

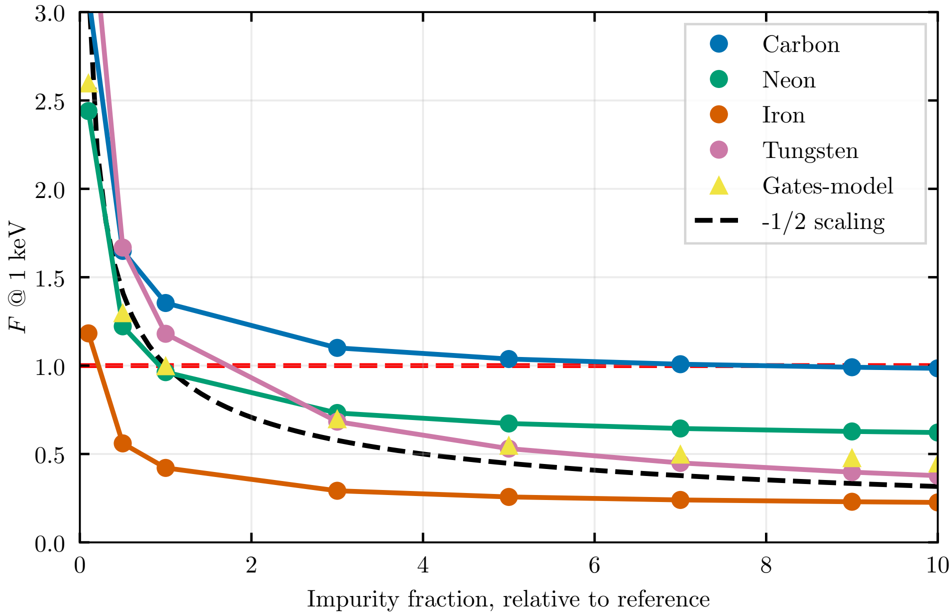

Figure 4.10: The dependency of the F-curve to impurity fraction relative to the values in 4.11 is given for $T_\mathrm{e} = 1\,\mathrm{keV}$ and $n_\mathrm{e} = 5 \times 10^{19}\ \mathrm{m}^{-3}$, along with data obtained from the Gates-model by Teng [39]. The height of the curve is arbitrary and can be changed by sampling F at a different temperature or reference impurity fraction. At sufficiently high impurity fractions the value of F falls of slower than the $-1/2$-scaling (black) that neglects the contribution of Z_eff. The value of F saturates at even higher fractions.

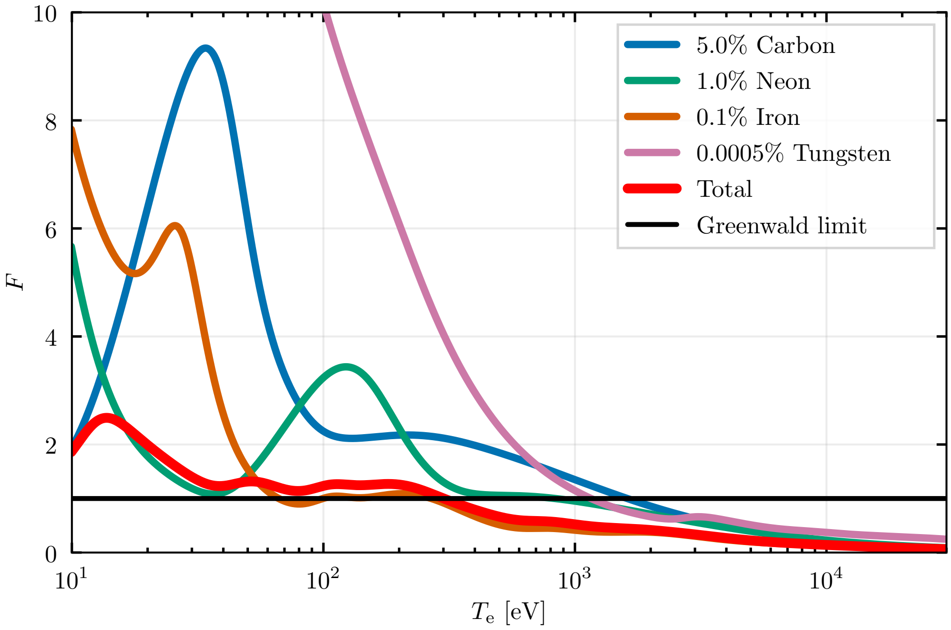

Figure 4.11: In order to describe more realistic situations with the F-function, a mixture of impurities is included in the analysis. The function with the lowest value at a certain temperature dominates the behavior of F. For temperatures ranging from $\sim 40\,\text{eV}$ to $\sim 300\,\text{eV}$, plateauing around $F \approx 1$ is seen. By combining the individual curves, the large temperature dependencies in the curve fall out as the function have local minima at different values of T_e.

peratures despite the fact that Ohmic heating should be dominant under the curve. This means that transport can not be disregarded entirely due to small islands with temperature profiles that are not entirely flattened (yet) during the start of the nonlinear phase. Additionally the global cooling of the plasma due to the presence of impurities, with relatively large edge cooling, enhances the temperature transport to the edge, lowering the temperature at the O-points. The motion towards higher n_e/j values is expected from the perturbation in the current density profile as the tearing mode evolves. As current is expelled from the island, local minima in j arise near the O-points, as seen in figure 4.4. The sudden vertical motions are due to the radial shift of the islands, causing not the O-point, but different parts of the island with higher j to be used in the calculation. Due to the profile uniformity and temperature flattening, n and T stay approximately constant. A future attempt at such a figure should include the calculation of the O-point at each timestep, instead of the manual selection for multiple steps at a time, which is used here.

Furthermore, the red curve at $250-300$ eV for 1% neon is of special interest as it shows a stabilizing effect of the F-curve. Even though the trajectory crosses the F-curve it is deflected back towards a balance between heating and cooling. The decrease in j is not sufficient to carry it over the peak, corresponding to a dip in the radiation curve. This example shows that both the value of the radiation curve as well as the derivative are of importance for the (de)stabilization of radiative islands.

For the case with 0.1% iron, the trajectories are bound for temperatures between 30-60 eV and the islands are stable. For temperatures around 100 eV, the enhanced growth is seen as trajectories cross the blue solid line. The cooling effect is limited however due to the strong gradient in F, acting as a stability boundary for further thermal runaway. At the highest temperatures all four cases show enhanced growth, even when under the F-function. This can be explained by radiation cooling the edge of the plasma, thereby enhancing radial transport, lowering the temperature around the $q = 2$ surface and enlarging the growth of the tearing mode.

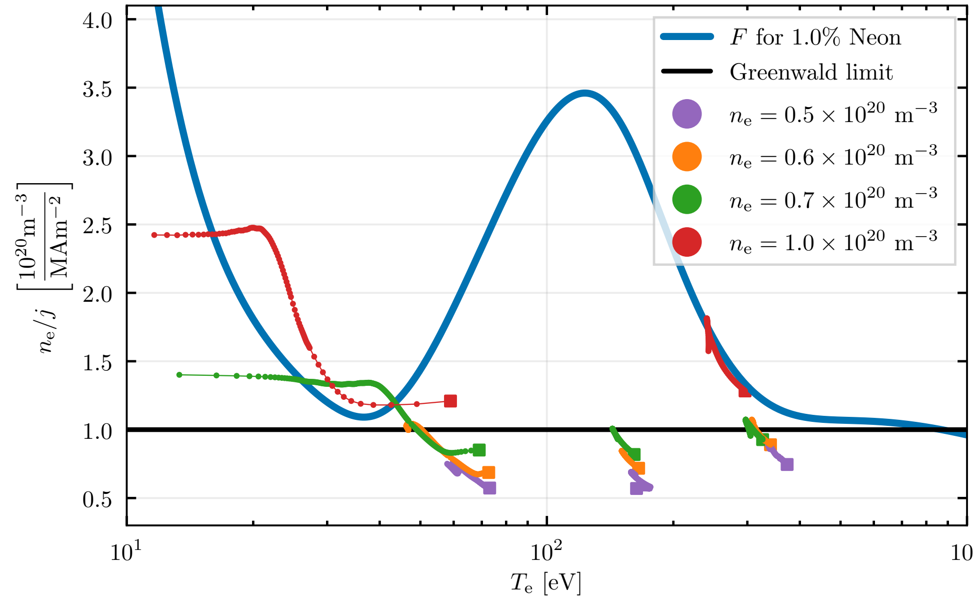

(a) 1% Neon

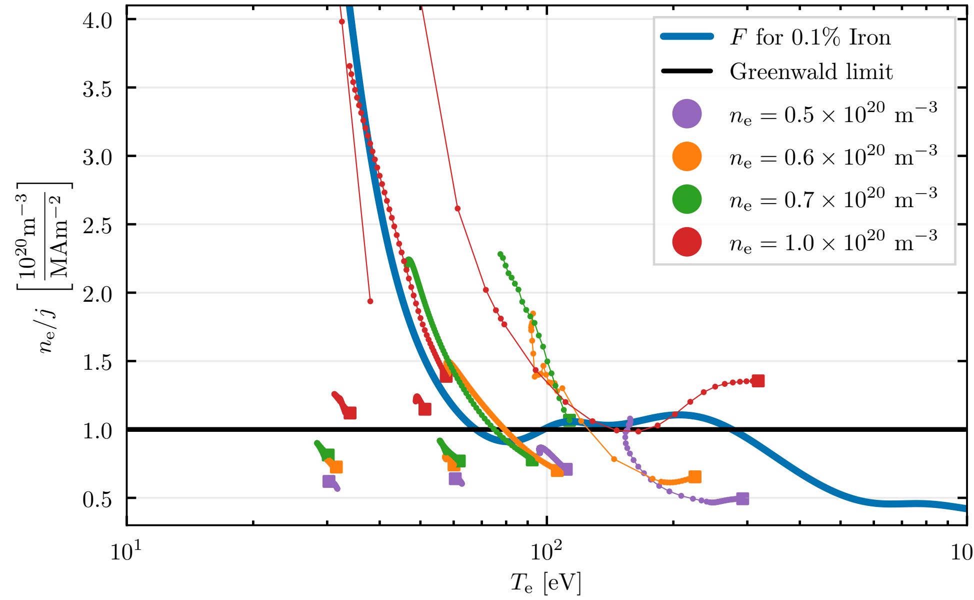

(b) 0.1% Iron

Figure 4.12: The electron temperature, density and current density are measured in the O-point of the magnetic islands during their nonlinear growth and given here in relation to the F-function. All trajectories have squares as starting points, with each consecutive time step represented by a dot and different colors corresponding to different electron densities. Trajectories that cross the curve experience a runaway effect as the island gets cooled. The curve can act as a stability barrier as well, preventing an island from further cooling, as shown for the rightmost red trajectory for 1% neon. In the bottom plot, with 0.1% iron, large excursions are seen for island temperatures of approximately 100 eV and larger. The large excursions at the highest temperatures, especially those under F, are due to a more heavily radiating edge, increasing the radial transport and net cooling.

4.3 Localized heating and cooling

This section is meant to give an explicit look at the influence of (localized) heating and cooling terms on the island growth.

4.3.1 Localized impurities

For the presented simulations the temperatures at the edge of the plasma correspond to high values on the radiation density curve of neon. This causes a relatively large temperature drop at the outer regions, increasing the radiation density even further. Due to the fixed boundary conditions at the edge of the plasma, the global minima of the profile shifts inwards from the edge, up to 10% towards the axis. This 'hollowing' of the outer region of the temperature profile is not physical. Besides this, the increased radiation and increased gradients could cause a radiative edge propagating inwards. This could be an alternative mechanism for triggering the enhanced growth of magnetic islands. To rule out a major influence of any of these two phenomena in the previously presented data, the simulation with parameters $n_\mathrm{e} = 0.7 \times 10^{20}\ \mathrm{m}^{-3}$, $n_\mathrm{Ne}/n_\mathrm{e} = 0.01$ and $T_\mathrm{e} = 100$ eV is repeated with localized radiation and a lowered edge temperature. Impurities are added in the region satisfying $-0.5 < \psi < -0.2$, $(0.418 < \psi_\mathrm{N} < 0.767)$, corresponding to a circular band around the $q = 2$ surface in the poloidal plane. This setup is similar to the simulations done in [40]. The evolution of the island widths and temperature profile are shown in figure 4.13. At the various time indicated in this figure, the Ohmic heating and radiative cooling terms are given in figure 4.14, along the same poloidal line as the temperature profile is given.

Overall, a similar island width evolution is found as for the uniform impurity distribution, with traced magnetic field lines making radial excursions of over half the size of the minor radius. In the temperature profile the effect of such a shortcut in the heat transport is evident. From a nearly unperturbed profile at $t = 0.0013\,\mathrm{s}$, flattening occurs once the island get a finite width. The central peak then fully collapses in approximately 8 ms during the stochastic regime. Moreover, the islands seem to be cooled sufficiently to create a local minimum around their O-points due to enhanced cooling inside. At the later times additional perturbations of the $3/1$-islands are seen near the edge. No signs of nonphysical hollowing close to the edge are present.

In the comparison of the heating and cooling, the islands can be identified by the minima in P_Ω, corresponding to minima in j. Inside the islands the radiation is strongest and causes the enhanced growing of the islands, here seen as an increase in amplitude and width of the perturbation in P_Ω. An additional nonlinear effect is seen in the radiation: the local cooling leads to an increase in radiation, which enhances the cooling again. This accelerates the growth process of the islands.

4.3.2 Additional Heating

The empirical Greenwald limit is reported to be both robust against auxiliary heating [19], but is sometimes overcome in scenarios with external heating [28]. In the Gates-model this could be explained by the (radial) location of the power deposition. The effects of centralized heating through Neutral Beam Injection (NBI) and localized heating around the $q = 2$ surface through Electron Cyclotron Resonance Heating (ECRH) are simulated using the heat source introduced in equation (3.22). Spatial parameter settings $\sigma_\mathrm{H1} = 0.1$, $\sigma_\mathrm{H2} = 0.1$, $\psi_\mathrm{H1} = 0.25$ and $\psi_\mathrm{H2} = 0.45$ are kept fixed, while the magnitude is varied for a total of eight scenarios, shown in table 4.2.

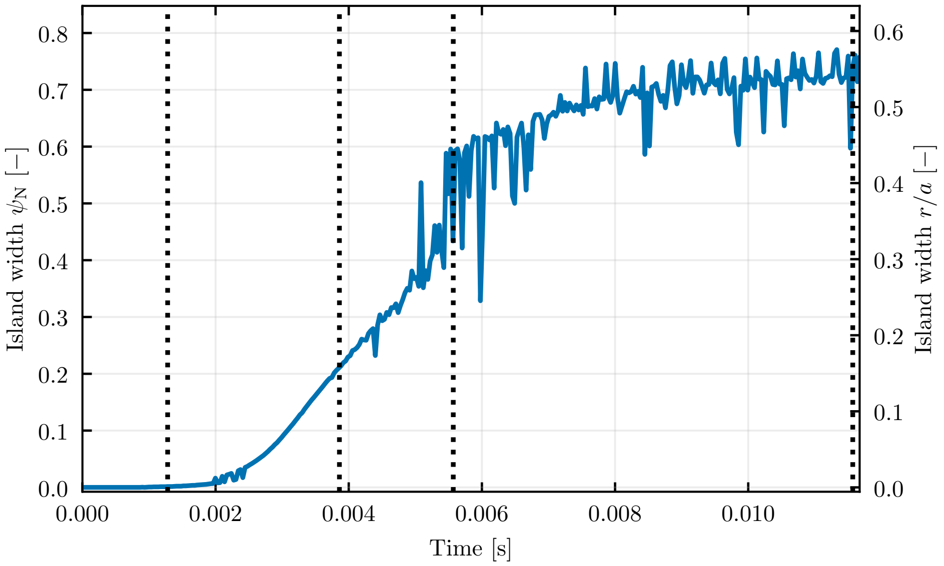

(a) Normalized island width

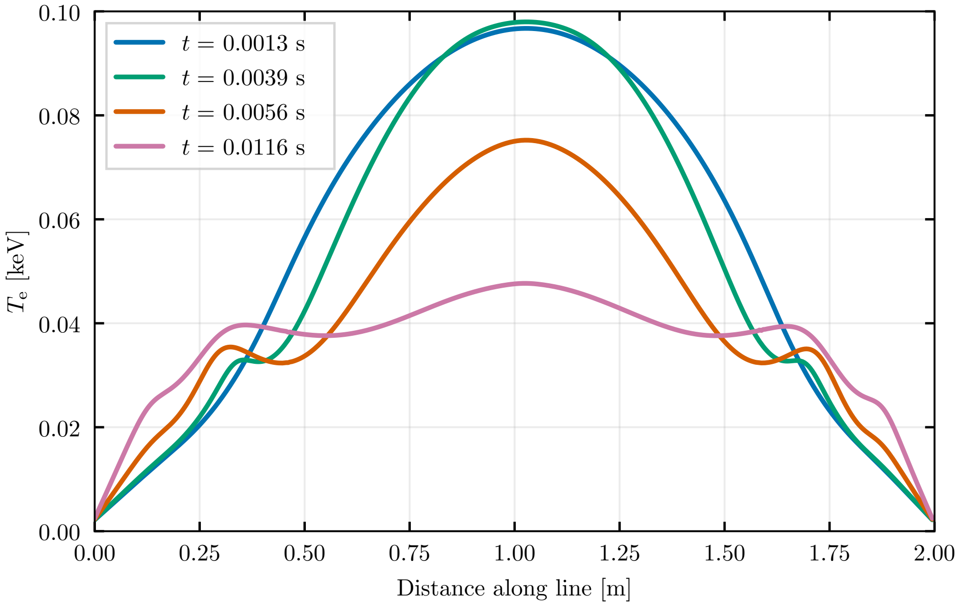

(b) Temperature profile evolution

Figure 4.13: The evolution of the island width and temperature profile are given for a simulation with 1% neon impurities localized around the $q = 2$ surface and a lower edge temperature. During the stochastic phase the island width grows substantially and the temperature profile collapses, reducing the central value by a factor 2. This effect is absent during the regular tearing mode growth shown figure 4.4.

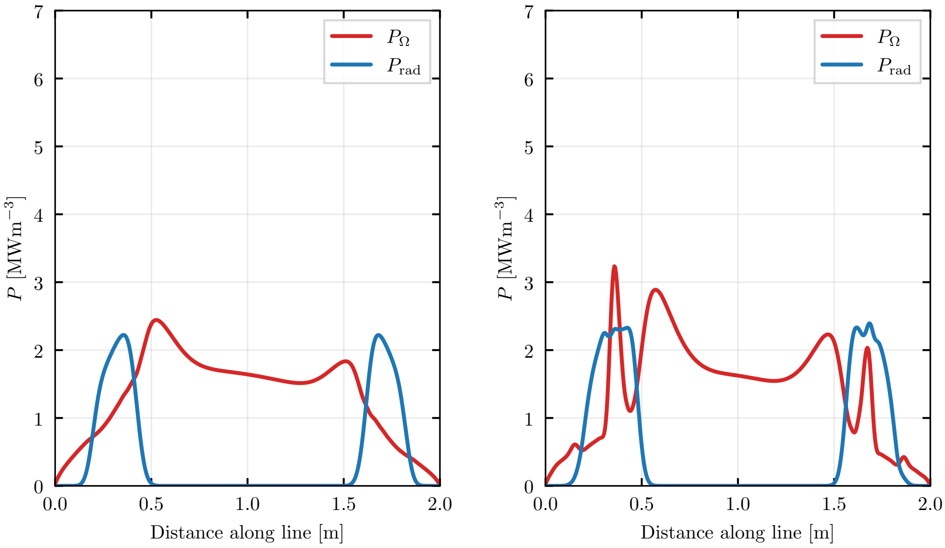

(a) $t = 0.0013$ s

(b) $t = 0.0039$ s

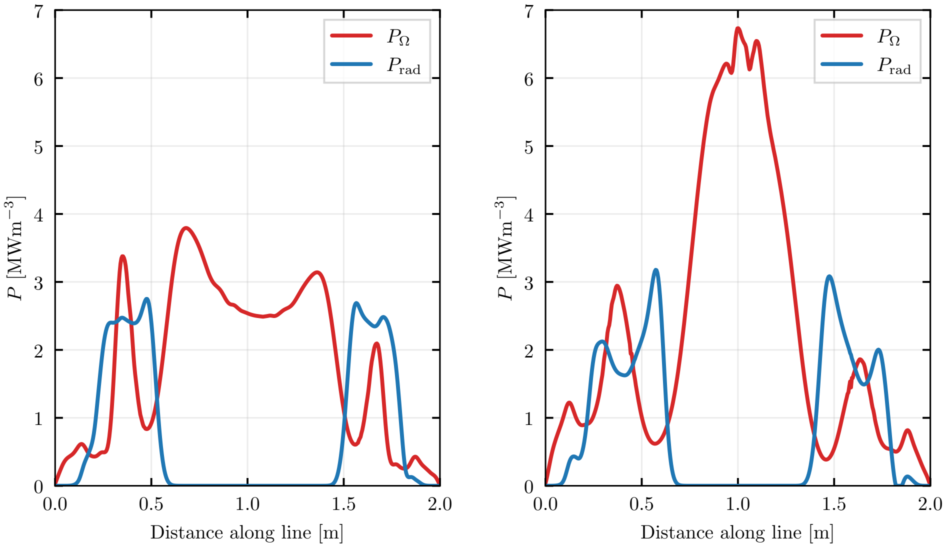

(c) $t = 0.0056$ s

(d) $t = 0.0116$ s

Figure 4.14: The Ohmic heating and radiative cooling along poloidal lines that intersect the islands at their largest width are plot at several times during the nonlinear growth phase. The localized cooling enhances the growth of magnetic islands. Nonlinear effects show through the increase in radiation as the temperature decreases due to net cooling.

Table 4.2: The magnitude of the heating profile is changed to simulate different heating scenarios. Due to changes in the ψ profile during the simulations, the total deposited power varies in time and is given at the start and end of the simulations.

Central heating

Case	S_0 [`JOREK` units]	Heating power [MW] (start-end)
Low	1×10^{-6}	7.2 - 5.2
Medium	3×10^{-6}	22 - 16
High	5×10^{-6}	36 - 34
Extreme	1×10^{-5}	72 - 72

Local heating

Case	S_{Gauss} [`JOREK` units]	Heating power [MW] (start-end)
Low	1×10^{-6}	6.2 - 6.2
Medium	3×10^{-6}	18 - 20
High	5×10^{-6}	31 - 33
Extreme	1×10^{-5}	62 - 65

Radial profiles of these scenarios are plotted in figure 4.15. Even though the localized heating has a much narrower profile, the total input power between the centralized and localized cases is similar, due to the fact that the latter are located more radially outwards.

The simulation with parameters $n_{\mathrm{e}} = 0.7 \times 10^{20}$ m^{-3}, $n_{\mathrm{Ne}}/n_{\mathrm{e}} = 0.01$ and $T_{\mathrm{e}} = 100$ eV is run from the start of the nonlinear phase for these scenarios. The island widths are calculated over time and compared in figure 4.16. Centralized heating has the effect of limiting the severance of the island growth, but does not seem to prevent the enhanced growth. With localized heating, the maximum widths are suppressed to remain within 15% or the minor radius for at least 2 cases. The lowest heating magnitude for which this is found corresponds to 'Medium heating'. Additionally, this is the case where the total heating and cooling are approximately equal at the $q = 2$ surface, according to figure 4.15.

Especially for the cases with low heating, the total input power is found to have a relatively large variation. This is due to the larger perturbation in the ψ_{N} profile, which is coordinate for which the heating power profile is defined. The simulation in which the 'extreme heating' settings are used are terminated early due to numerical instabilities created by large gradients in temperature and current.

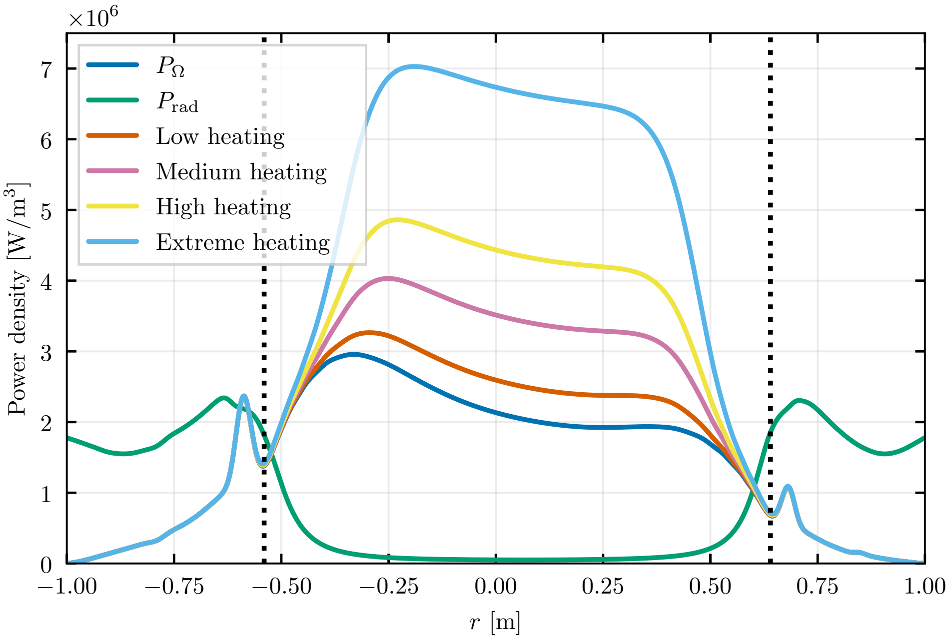

(a) Central heating

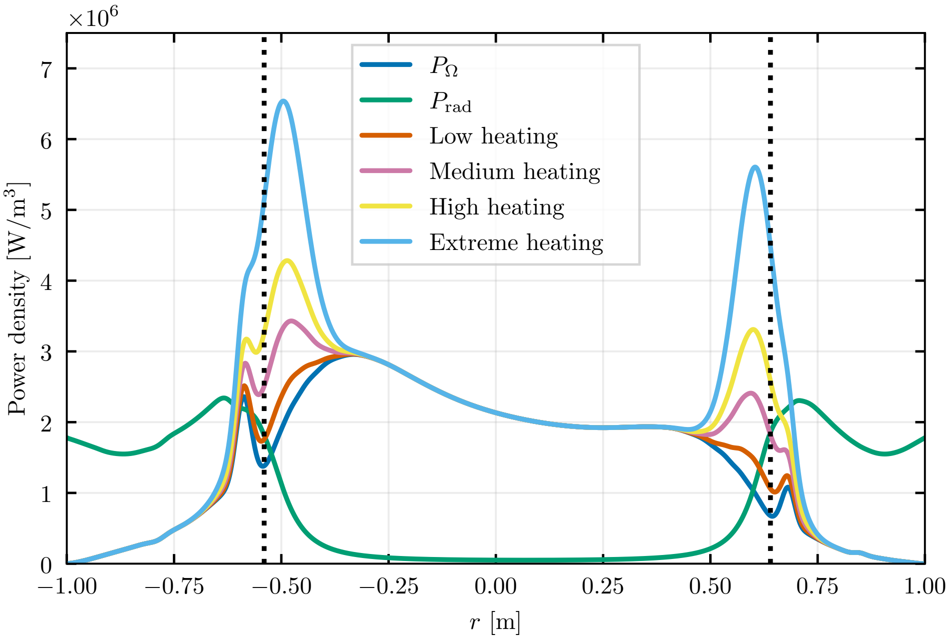

(b) Localized heating

Figure 4.15: The radial profiles of the radiative cooling and Ohmic + auxiliary heating are plot at the start of the different scenarios. The locations of the $q = 2$ surfaces are indicated by the black dotted lines.

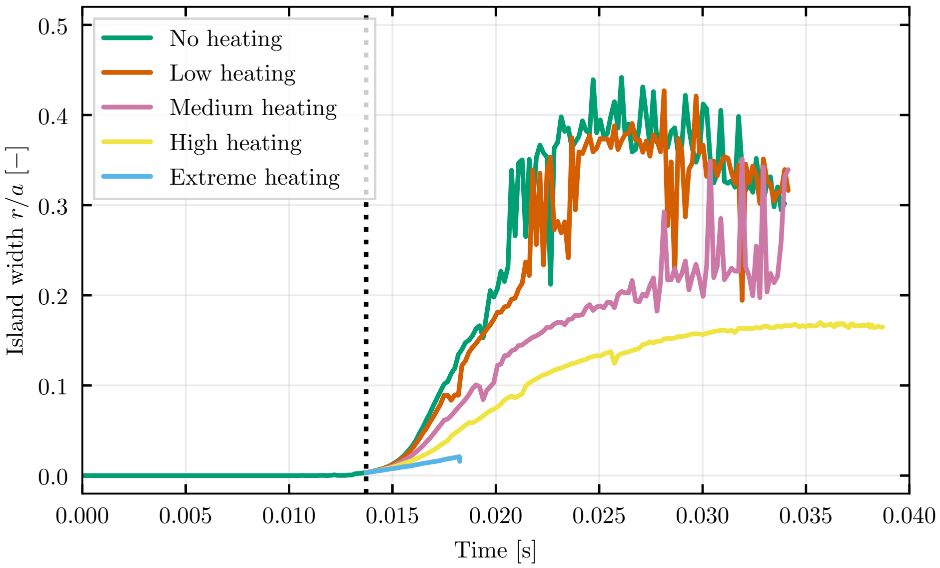

(a) Central heating

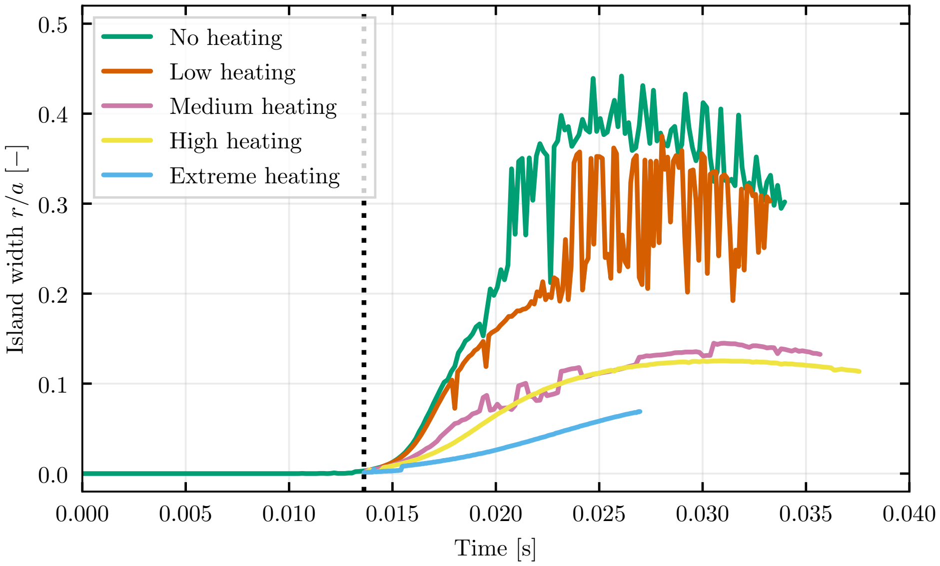

(b) Localized heating

Figure 4.16: The evolution of the island width shows that for similar total deposited heat the localized scenarios are capable of limiting the maximum island growth to within 15% for at least 2 cases. For the central heating no such scenario is conclusively found. The cases labeled as 'Extreme heating' suffered from numerical instabilities and are terminated relatively early in the nonlinear phase.

4.4 From a local balance to a global limit

Now that an attempt has been made to characterize the Greenwald density limit using the F-function and local parameters, this section presents an attempt to make a robust coupling between the local parameters and the global form of the limit as in equation (1.7). In order to match the local power balance to a global one, the set of self-consistent Furth-Rutherford-Selberg (FRS) equilibria will be used, which first appears in [42] and later in the Gates-model.

In the latter, the FRS equilibria play a significant role as they serve both as initial conditions in simulations [40] and as an effort to explain the switch from net heated to cooled magnetic islands [39]. This is based around the argument that a higher plasma density causes the current profile to be more peaked, thereby altering the Ohmic heating term at the $q = 2$ surface. Note that this effect is not explicitly looked at in this thesis. In this work, the profiles of the FRS equilibria are not used and the most influential aspect is found to be the impurity radiation. However, the FRS profiles will be used in this section as a tool to couple the local and global limit for multiple experimental devices and models.

In the FRS equilibrium the toroidal current density is given by

$$j(r) = j_0 \left[1 + \left(\frac{r}{r_0}\right)^{2\nu}\right]^{-(1+1/\nu)} \tag{4.7}$$

with j_0 the central current density, r the spatial distance along the minor radius and r_0 the typical width of the current channel which is related to the peakedness ν of the profiles. Imposing the requirement that the current distribution is smooth and poloidally symmetric leads to the restriction that the derivative on the magnetic axis should be equal to zero. This derivative is

$$\frac{\partial j}{\partial r} = -j_0 \frac{2\nu}{r_0}\left(1 + \frac{1}{\nu}\right) \frac{\left(\frac{r}{r_0}\right)^{2\nu - 1}}{\left(1 + \left(\frac{r}{r_0}\right)^{2\nu}\right)^{2+1/\nu}}, \tag{4.8}$$

and the requirement

$$\lim_{r \downarrow 0} \frac{\partial j}{\partial r} = \begin{cases} 0, & \text{if } \nu > \frac{1}{2} \\ \text{undetermined}, & \text{if } \nu \leq \frac{1}{2}, \end{cases} \tag{4.9}$$

puts a lower bound on the peakedness of the profiles in the FRS equilibria.

Again assuming symmetry in the poloidal plane, the safety factor profile is obtained by using equation (1.2) in combination with Ampère's law, resulting in

$$q(r) = q_0 \left[1 + \left(\frac{r}{r_0}\right)^{2\nu}\right]^{1/\nu}. \tag{4.10}$$

The central value q_0 is related to the central current density by

$$q_0 = 2B_{\text{tor}}/(\mu_0 R_0 j_0) \iff j_0 = 2B_{\text{tor}}/(\mu_0 R_0 q_0), \tag{4.11}$$

with R_0 the (constant) major radius of the plasma. The width of the current channel is expressed in the values of the q-profile on the axis, on the edge q_{edge} and the minor radius a:

$$r_0 = a\left[\left(\frac{q_{\mathrm{edge}}}{q_0}\right)^{\nu} - 1\right]^{-1/2\nu}. \tag{4.12}$$

The safety factor and current density profiles are plotted for different values of ν in figure 4.17, corresponding to a peaked, rounded and flattened shape according to [42].

Based on these profiles the radial locations of the $q = 2$ surface and volume averaged density $\bar{j} = I_{\mathrm{p}}/\left(\pi a^2\right)$ are calculated and compared. First, the total current I_{p} is obtained by integration over the poloidal plane, again assuming a circular, poloidal symmetric plasma:

$$\begin{aligned} I_{\mathrm{p}} &= \int_0^a j_0\left[1+\left(\frac{r}{r_0}\right)^{2\nu}\right]^{-(1+1/\nu)} 2\pi r dr \\ &= \pi a^2 j_0\left[1+\left(\frac{a}{r_0}\right)^{2\nu}\right]^{-1/\nu} \\ &= \pi a^2 j_0\left(\frac{q_0}{q_{\mathrm{edge}}}\right) \\ &= \pi a^2\frac{2B_{\mathrm{tor}}}{\mu_0 R_0 q_{\mathrm{edge}}}. \end{aligned} \tag{4.13}$$

The total current is thus independent of ν. Now solving $j(r) = I_p/\pi a^2 = \bar{j}$ for r gives

$$\begin{aligned} r_{j=\bar{j}} &= r_0\left(\left[1+\left(\frac{a}{r_0}\right)^{2\nu}\right]^{1/(1+\nu)} - 1\right)^{1/2\nu} \\ &= a\left[\frac{\left(\frac{q_{\mathrm{edge}}}{q_0}\right)^{\nu/(1+\nu)} - 1}{\left(\frac{q_{\mathrm{edge}}}{q_0}\right)^{\nu} - 1}\right]^{1/2\nu}. \end{aligned} \tag{4.14}$$

So the location where the local and volume averaged current densities match, does depend on the shape of the profile, which is not surprising. However, this dependence is typically weak, of the order of a few percent, as can be seen by the marked locations in figure 4.17 or the continuous line in figure 4.18.

In a similar calculation as above, the location of the $q = 2$ rational surface is found by solving $q(r) = 2$ for r:

$$\begin{aligned} r_{q=2} &= r_0\left[\left(\frac{2}{q_0}\right)^{\nu} - 1\right]^{1/2\nu} \\ &= a\left[\frac{\left(\frac{2}{q_0}\right)^{\nu} - 1}{\left(\frac{q_{\mathrm{edge}}}{q_0}\right)^{\nu} - 1}\right]^{1/2\nu}. \end{aligned} \tag{4.15}$$

This expression has roughly the same structure as (4.14). The radial locations, normalized as r/a, are now obtained as a function of 3 parameters: q_0, q_{edge} and ν. For most devices or experiments, the center and edge value of the q-profile is fixed and known, while information about the shapes of these profiles is not necessarily available. This is why the presented results in the next figures are given as a function of ν.

The electron density profile does not appear in the FRS equilibria. However, using a simple parabolic function as a typical profile, the density can be included in the analysis. The radial dependency is equal to the initial profiles in simulations on the Gates-model [40]:

$$n_\mathrm{e}(r) = n_{\mathrm{e},0}\left(1 - \frac{r}{a}\right)^2, \tag{4.16}$$

with $n_{\mathrm{e},0}$ the central density. From this an approximation of the line-averaged density can be calculated, which in this case is purely done in the poloidal plane. In real experiments, the line-averaged density may be obtained from a sight-line with a toroidal directional component. Due to the variation in geometrical placement of diagnostics in fusion devices, the toroidal component of such a sight-line will not be included. If only the poloidal plane is considered and a line going from the magnetic axis to the edge of the plasma is traced, implicitly the assumption is made that each flux surface contributes an equal amount to the density. This gives the following integral:

$$\overline{n}_\mathrm{e} = \frac{1}{a}\int_0^a n_{\mathrm{e},0}\left(1 - \frac{r}{a}\right)^2 dr = \frac{2}{3}n_{\mathrm{e},0}. \tag{4.17}$$

Now solving $n_\mathrm{e}(r) = \frac{2}{3}n_{\mathrm{e},0}$ for r gives

$$r_{n=\overline{n}} = \frac{1}{3}a\sqrt{3}. \tag{4.18}$$

The three obtained radial distances are directly compared as a function of ν in figure 4.18, with typical values for the safety profile between 1.4 and 3.7, consistent with the profiles from the simulations presented in earlier parts of this thesis. From this plot can be seen that the locations where average and local density and current density match are within a few percent of each other, for any peakedness. Furthermore, an island width of 15% is assumed and drawn symmetrically around the $q = 2$ rational surface. This value is based on typical maximum island widths found in figure 4.6, but remains arbitrary in some sense. The grey band indicates the radial extent that a magnetic island spans. The rational surface lies in vicinity to the other curves for most of the peakedness range, roughly between 1 and 3. The local values of n_e and j at a magnetic island, with such width and in a plasma with the presented profiles, translate directly to the global, averaged values. In other words, the measured values $\overline{n}_\mathrm{e}$ and $\overline{j}$ can then directly be used as local values at the $^2\!/_1$-islands. This effectively couples the local mechanism of the Gates-model to the global Greenwald density limit criterion.

A similar analysis is done for experiments in which the density limit is encountered, using the values listed in table 4.3. The range of possible overlap of the magnetic islands with the radial distances for density and current are given in figure 4.19. Here the dark and light bars give the overlap with the current and density curve respectively. Per device the two bars transpose and change length in similar consistent fashion, which is due to the associated radial locations $r_{n_\mathrm{e}=\overline{n}_\mathrm{e}}$ and $r_{j=\overline{j}}$ vary little in the FRS equilibria. It is thus the intersection with the $q = 2$ surface that determines the range in ν for which the global and local limits match.

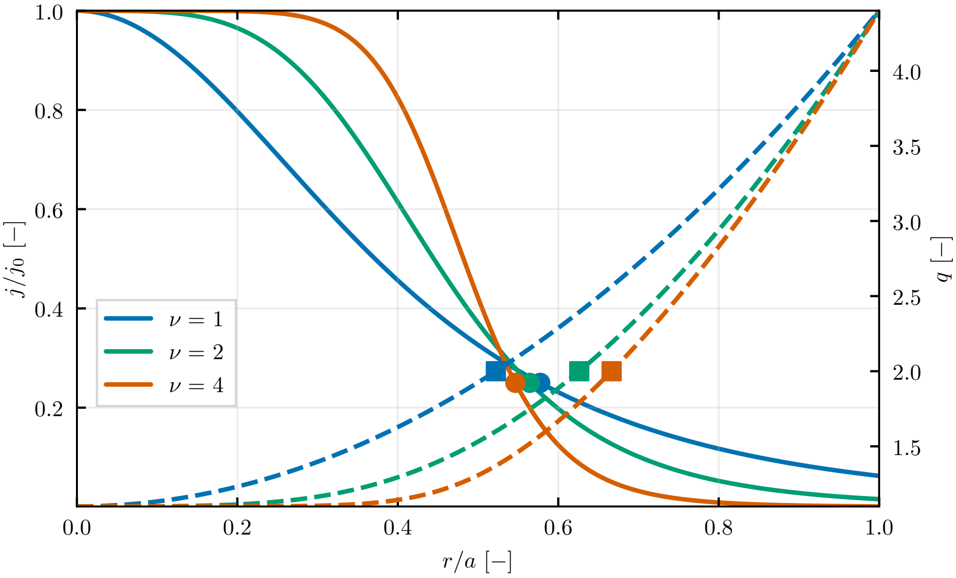

Figure 4.17: The radial profiles of the normalized current density (solid) and safety factor (dashed) are calculated according to the Furth-Rutherford-Selberg (FRS) equilibrium [42]. Variation of the peakedness parameter ν from peaked (1) to rounded (2) and flattened (4) results in variation in the shape of the profiles. The radial location of $\overline{j}$ stays approximately at the same place, while there is a variation of about 0.15 in the location of the $q = 2$ surface.

The significant ranges in ν for which this matching holds, is a possible explanation for why the density limit is widely encountered across multiple experiments. The appearance that the radial location of the $q = 2$ surface is the dominant factor, is in agreement with the conceptual description of the local heat balance: shifting an island to a region with a higher j (and thus higher P_Ω) or a lower n_e (and thus a lower P_{rad}) can prevent net cooling in its interior and thereby make operation above the Greenwald density limit possible.

Table 4.3: The device and operation parameters used to calculate the peakedness regime of figure 4.19, with data adapted from density limit simulations in the Gates-model [40], and experiments (or general operational parameters) in several devices: TEXTOR [28], ITER [70], ASDEX [71] and JET [72, 22].

Device/model	R_0 [m]	a [m]	B_{tor} [T]	q_0	q_{edge}
This thesis (`JOREK`)	3.0	1.0	3.67	1.4	3.7
Gates-model	3.0	1.0	1.0	1.01	3.7
TEXTOR-94	1.75	0.46	2.0	1.1	4.4
ASDEX-Upgrade	1.65	0.5	1.75	1.1	4.0
ITER	6.2	2.0	5.3	1.2	3.0
JET	2.96	1.25	3.45	1.1	2.9

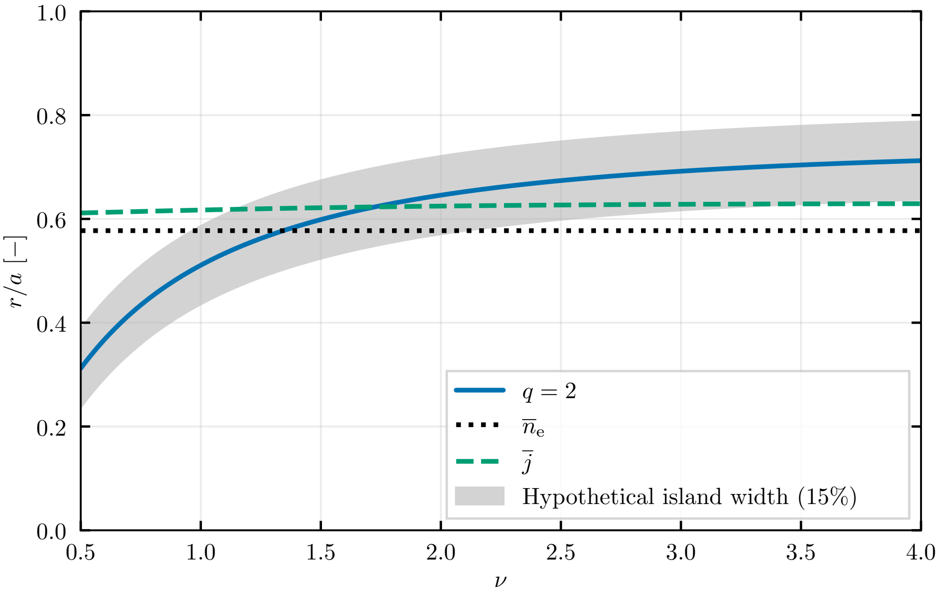

Figure 4.18: The radial location of the $q = 2$ surface with is shown with a symmetric band of 15% around it indicating the radial extent of a magnetic island. For a significant range of profile shapes, indicated by ν, there is an overlap between this surface and the locations where the averaged density and current are equal to the local values.

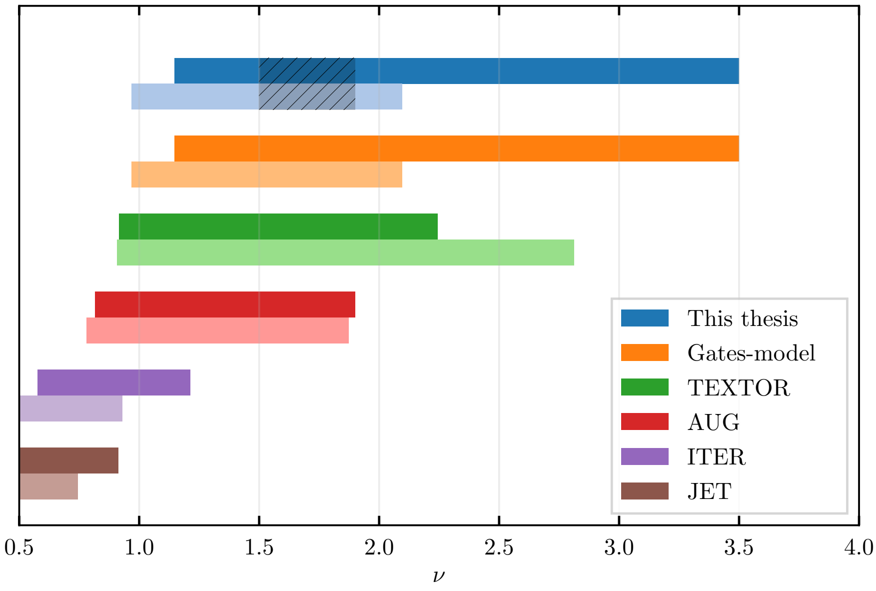

Figure 4.19: The FRS equilibria are imposed on the simulations in this thesis, as well as earlier simulations on the Gates-model and operational conditions of several devises. The overlap is shown between a magnetic island with a width of 15% and the radial locations (4.14) for averaged current density (dark) and (4.18) for electron density (light) are equal. The black shaded region indicates the range of current profiles used in the `JOREK` simulations.

5. Discussion

In summary, the results presented in the previous chapter are split between different aspects: the mechanism, the coupling of local and global scales and heating effects. Each provides a different perspective to the relation between the Gates-model and the Greenwald density limit. The tearing mode is found in `JOREK` simulations for electron densities between 0.5 and 1.0×10^{20} m^{-3} and central electron temperatures between 50 and 500 eV, with growth rates in the linear phase matching the theoretical $T_\mathrm{e}^{-9/10}$ scaling. During the nonlinear phase full temperature flattening inside the growing island is found. Without impurities and radiation, maximum normalized island widths of 0.15 are found during the overshoot in the nonlinear phase. For increasing neon impurity concentrations, the timescale on which the islands grow decreases from tens of milliseconds to a few milliseconds. Normalized widths increase to values significantly larger than 0.15, with values between 0.2-0.5 being the result of stochastisation. The maximum observed widths in these cases exceed the reported critical width of 30% required to trigger a thermal quench [68]. A sharp transition between these island growth regimes is found for net heated or cooled islands for densities 20% above the empirical Greenwald limit. Numerical results show the dependency of this transition on temperature, electron density, impurity density and impurity type. Semi-analytic results explain these dependencies with the F-function. Plateauing around $F = 1$ is observed for specific impurity mixtures, together with a vanishing dependency on f_imp. Cooling only the region around the $^2\!/_1$-islands is found to be sufficient in triggering the enhanced growth of magnetic islands. Subsequently, part of a temperature quench is observed. Localized heating at the islands is able to suppress island growth to normalized widths of 0.15, while central heating is found to be less efficient, suppressing the width to 0.17 at higher heating power. Finally, using the Furth-Rutherford-Selberg equilibria, expressions are found for the radial locations where local and averaged quantities match in combination with the radial location of the $q = 2$ surface. Assuming a width of 0.15 for the $^2\!/_1$-island, a range of profiles is found for different models and devices, where the averaged quantities in the global Greenwald density limit can be replaced by local quantities.

These results will first be discussed with respect to earlier work done on the Gates-model, before comparing them to experiments, as far as applicable. After that, new insights are presented along with unaddressed issues and concrete recommendations for follow-up studies.

5.1 Relation to the Gates-model

Most comparisons in this section come from the two most recent papers in which the Gates-model is formulated in similar terms as in this thesis [39] and results of nonlinear simulations on radiative island growth are presented [40].

The evolution of the island width in figure 8 of Teng [40] occurs on a typical timescale of $0.04 - 0.05\tau_\mathrm{R}$. This is compared to the evolution presented in figure 4.6. The temperature inside the island is approximately 70 eV, according to figure 4.12, such that the resistive time is $\tau_\mathrm{R} = 0.83\,\mathrm{s}$. In real time the timescales from Teng are then 0.03-0.04 s, which is similar to the 0.03 s found in `JOREK` between the start of the nonlinear phase and the maximum island width. This is for cases where the island width is enhanced, but not growing into a stochastic regime, since ergodic behavior is not observed in earlier work on the Gates-model.

While timescales of the island growth match, discrepancy is found in the maximum island widths reached. In this thesis normalized widths range from 0.15 in the impurity-free scenario, to 0.17 under enhanced growth and 0.2-0.5 in stochastic regimes. In earlier numerical work, islands are always found to be smaller than 10% of the minor radius [40], while semi-analytically a range between 25% - 35% is found at the density limit. The numerical values in this thesis thus follow the latter predictions in earlier literature better than previous simulations, despite similarities in geometrical and physics parameters. However, values above 0.2 in this report should not be regarded as real island widths, but rather as radial excursions of stochastic magnetic field line. The analytical models do not account for this.

A possible explanation for the discrepancy in found widths with other numerical work can be due to the omission of higher order harmonics in the `JOREK` simulations. This choice enables only the growth of modes at flux surfaces with integer q values. $^2\!/_1$-islands are expected to saturate at smaller widths when additional modes are able to grow at intermediate rational surfaces. Indications for this are present in earlier `JOREK` simulations [43, 73, 74]. On the other hand, with more modes being present, overlapping and the transition to stochastic regimes may happen at smaller widths already, but then again covering smaller radial extends.

As for the scan over electron densities, the island width is found to show a drastic increase by a factor of 3 [40] or even more than 10 [39] when these densities are increased from $0.8n_\mathrm{G}$ to values $1-1.05n_\mathrm{G}$. In this thesis, the sharp transition is found at densities well above the Greenwald density, when going from $0.6\times10^{20}\,\mathrm{m}^{-3}\approx 1.04n_\mathrm{G}$ to $0.7\times10^{20}\,\mathrm{m}^{-3}\approx1.21n_\mathrm{G}$. However, with the use of figure 4.12 it is identified that n_G is not a good measure for the local description of the limit. The actual figure of merit is the local value of F, which determines the boundary between net heated and cooled islands. From this in combination with the definition of F in 4.4, it can be concluded that the local limit is dependent on the local electron temperature, electron density, impurity density, impurity type and current density. The repeated finding of the island growth at n_G in literature may thus either be a coincidence or the result of deliberate tuning of parameters. For example, the use of iron as main or only impurity species between 100-300 eV explains the lack of temperature dependence.

In the Gates-model, the peakedness of the profiles is a key parameter in determining the transition from heated to cooled islands. For this net cooling, at the $q=2$ surface the inequality $n_\mathrm{e}/j > F(n_\mathrm{e}, T_\mathrm{e}, f_\mathrm{imp})$ is needed. With an additional ad-hoc model for the internal inductance, at higher densities more peaked profiles are obtained, which increase n_e/j at $q=2$. In this thesis however, the peakedness and internal inductance are not explicitly used anywhere with regard to the simulations. The initial current density is consistently calculated from the pressure profile according to the Grad-Shafranov equation 3.24. An increase of the flat density profile leads to steeper pressure gradients under the same temperature, which then does steepen the current density profile. The total current is not fixed, in contrast to earlier work. The increase of the electron density and subsequent changes to j calculated by the Grad-Shafranov equation 3.24 are equally sufficient to trigger islands into enhanced growth. In `JOREK` simulations there is no explicit need for internal inductance, peakedness or FRS equilibria to reproduce the mechanism of the Greenwald density limit and observe the threshold behavior.

As a final remark, the dependency on impurity density is considered. The scaling of the F-function with $f_\mathrm{imp}^{-0.5}$ for low concentrations and the flattening at relatively high concentrations is universally found for the different impurity species and concentrations, see figure 4.10. Consistently with these results, this effect is found in

Gates-model, for which the following explanation is given:

"The weak impact of impurity densities on the limit is because when impurity densities are increased, Z_{eff} increases and T_{e} increases as η is fixed (...). The cooling rate L_Z then decreases (...). This effect is canceling the impact of impurity densities on radiation power. Thus the dependence of the density limit on impurity densities is weaker than $n_Z^{-0.5}$ as one would expect[.]" [39],

in which n_Z is used as impurity density. In this thesis the requirement that η is fixed and the direct consequences that has on temperature and cooling rate are not used. Neither are they necessary in reproducing the weak dependence on f_{imp} found in [39]. On top of that, if any additional effect should be taken into account, then that would be a temperature *decrease* due to the presence of higher concentrations of impurities. This would lead to an increase in η_{Sp} and thus in Ohmic heating. The effect of the cooling on the radiation is determined by the local temperature derivative, but for most cases will stay similar or increase, especially for mixtures. Accompanying the previous quote is an additional reasoning towards the global density limit:

"[T]he density limit varies by no more than 2.5 times. This implies that the density limit can't be improved much by reducing the impurity densities considering the difficulty of removing the impurities in experiments." [39]

In contrast to this, the plateauing of F, as shown in figure 4.10, occurs only for sufficiently high impurity densities. For lower concentrations there *is* a strong $n_Z^{-0.5}$ dependence. Conceptually this means that for each decrease in impurity fraction the density limit becomes less strict. Any achieved stable operation with a density above the Greenwald limit is beneficial for the fusion reaction efficiency. Exceeding the limit by 40% in TEXTOR has been reported as a large success, indicating the relative importance of high density operation [28]. For future experiments much smaller factors than 2.5, even just above unity, above the limit can make the difference between net fusion energy and a show stopper.

5.2 Relation to experiments

Direct comparisons of the simulations with experiments for which the Greenwald density limit is found are difficult due to the limited data[1] on impurity profiles and concentrations. First, comparisons are made with experiments in TEXTOR-94, in which both disruptions due to a symmetric radiative collapse and due to high electron density at the Greenwald limit are observed [29, 28]. For high impurity concentrations, $n_{\mathrm{Ne}^{10+}} \approx 1-4\%$ and $n_{\mathrm{C}^{6+}} \approx 1\%$ a symmetrical radiative collapse is found where the radiated power exceeds the input power at the edge. The temperature decreases at the edge and causes a radiation front to propagate inwards. This description matches observations found in this work where for high impurity concentrations and electron densities the radiation at the edge is higher than around the islands. This is specifically seen for the cases with $f_{\mathrm{Ne}} = 1\%$, $n_{\mathrm{e}} = 10 \times 10^{20}\mathrm{m}^{-3}$ and with $f_{\mathrm{Fe}} = 0.1\%$ at 500 eV, see figure 4.8. Specifically for the neon case, the transition is seen in which for relatively low densities, the islands are net cooled and become unstable, even when the global radiated power is smaller than the heating power. At either higher electron or impurity densities the radiative disruption is seen with enhanced island growth due

---

[1] An effort is made to obtain experimental data on disruptions from a selection of experimental devices. Especially time traces of n_{e}, T_{e}, P_{rad}, and their peaking factors as shown in [75] are of interest. Unfortunately access to this data is not obtained during this thesis.

to rapid cooling on a faster timescale than the indepedent growth of the tearing mode, as identified in figure 4.2.

In either disruption case, $^2/_1$-oscillations are experimentally observed due to the rapid growth of the magnetic islands [19, 29]. These islands can be detected in external coils due to the plasma rotation and the islands moving with the plasma. Despite its importance in effects associated with disruptions, such as mode-locking [22, 21], rotation is not included in this thesis. For the heat balance this rotation is expected to be of little importance, but to eventually be able to simulate the full current quench, it should be included. Specifically for Greenwald density limit disruptions, the $^2/_1$-oscillations are seen up to 40 ms prior to the macroscopic temperature loss and the disruption in TEXTOR shot #59297 [29]. This supports the Gates-model in which the islands grow due to a local power imbalance, before the macroscopic profile is affected and lost. In figure 4.13, this is visible from the small perturbation in the temperature profile during the island growth. As soon as the stochastic region is reached, the temperature profile collapses rapidly.

The experimentally observed local radiative precursors observed prior to disruptions at the Greenwald limit, MARFEs, are neither expected nor observed in the `JOREK` simulations. A plasma geometry with an X-point is a prerequisite for MARFEs to appear, as they are found outside the closed flux surfaces [76, 19, 28]. The fact that this is a radiative event points in the direction of relatively large impurity concentrations at the edge, but does not necessarily lead to radiative islands. In the current state the observation of MARFEs neither proves nor disproves the Gates-model.

Besides these comparisons with specific phenomena, the general empirical scaling of the Greenwald density limit should be addressed. The absent dependence on impurity density and temperature can only be united with the Gates-model if the F-function is independent on these parameters. Two plausible explanations are the weak dependence on f_{imp} at sufficiently high values (figure 4.10) and having specific mixtures to cancel out the T_{e}-dependence (figure 4.11). These effects are shown in figures 4.10 and 4.11 respectively. To make a conclusive comparison, in future studies the impurity types and fractions from specific experiments need to be obtained. Then it can be validated whether F is indeed independent of T_{e} and n_{imp} in the operational regime of that specific reactor.

In this thesis, the simulations on the effects of different heating scenarios should be seen as a study on the mechanism, not as an attempt to realistically mimic existing heating methods. more a study on the principle. Heating outside the island's separatrix is investigated first in this thesis. The lower efficiency compared to local heating is a first indication of the absence of auxiliary heating power in the empirical limit. Besides this, the scan over heating scenarios does not mimic experiments. To simulate modern devices and how the Greenwald limit is overcome through auxiliary power input, realistic heating scenarios are needed.

The island growth and changes in the T_{e}-profile both happen on a timescale on the order of 10 ms, according to figures 4.6 and 4.13. The typical time it takes for the charge state distribution to equilibrate and thus for the coronal approximation to be valid, is on the order of milliseconds [63, 64]. In the case that the coronal model would not be valid on the timescales of the mechanism, the islands in experiments will experience radiation deviating from the radiation rates given by OPEN-ADAS. The simulations and semi-analytical work in this thesis are mutually consistent. It is expected that for a different radiation model the qualitative results on the mechanism will remain similar. The analysis of the F-function could then be off in predicting for which temperatures or fractions the radiative cooling will happen. Because the resistive timescale and thus tearing mode evolution becomes longer for higher temperatures, it is expected that the coronal assumption will generally hold better for future studies where experiments are replicated at higher temperatures, increasing the resistive time scale.

Finally, the applicability of the FRS equilibria used in chapter 4.4 is considered. Because the argument in this section is meant mainly as qualitative one, the chosen profiles in this model do not exactly have to match the profiles in the simulations or experiments. Least square fits of the FRS current profile over several `JOREK` current distributions show that the peakedness of the numerical profiles is centered in the region for which overlap between the radial positions is found. For the argument that the radial positions are separated less than a typical island width, this is sufficient.

5.3 New insights and extrapolations

Despite the differences and uncertainties presented above, the mechanism in the Gates-model is consistently observed in `JOREK` simulations and matches several experimental observations. Now the added benefit of a semi-analytical model shows, because it can be used to generalize the specific simulations and extrapolate. Based on new work done in this thesis, new predictions can be done, which are presented here.

The F-function is shown as a stability boundary between net heated and cooled magnetic islands in figure 4.12, with trajectories of $(T_\mathrm{e}, n_\mathrm{e}/j)$ obtained at the O-points indicating the effect of the tearing mode and cooling. In this report the transition from separate temperature-dependent curves from single species towards the total F-curve for multiple species and the plateauing effect around $F = 1$ is visualized. Using the knowledge of F for a specific experiment, the local quantities at the $q = 2$ surface can be used to predict a disruption instead of averaged ones, if they are available from diagnostics. Even more important, is that the new knowledge about F can be used in finding pathways to exceed the limit. As shown in figure 4.12, peaks in F act as nonlinear stability barriers against the thermal runaway. As a result, operation with 1% neon at 500 eV is stable and allows for densities much higher than the theoretical limit, while at 100 eV a series of disruptions is observed. For impurity mixtures this tells which impurities are most harmful in triggering the radiative growth and should be avoided most. By customization of the impurity content (in combination with the temperature profile at the islands), disruptions can be prevented. As an example based on figure 4.11, with temperatures between 50 eV and 400 eV around the $q = 2$ surface, removing iron from the machine is beneficial, even if it comes at the cost of higher concentrations of the other species. As far as the Gates-model is concerned, it will allow for densities a factor 2 above n_G. Even an increased edge radiation is an acceptable trade-off, as this is commonly countered by additional edge heating [28].

To improve the reliability of such predictions, the $(T_\mathrm{e}, n_\mathrm{e}/j)$-trajectories as shown in figure 4.12 should be quantified either empirically or analytically. To increase accuracy with respect to the manual method used in this thesis, the island finding routine of Appendix B should be extended to allow for finding of O-points. Using reference trajectories due to regular tearing modes, one should be able to predict whether a thermal runaway may happen and which shape of F is needed to prevent this.

An additional way of altering F is by extra heating. Especially for high temperatures above 1 keV, radiation will overcome the Ohmic heating at low densities, according to figure 4.9. This is mainly due to the $T^{-3/2}$ scaling of the Ohmic heating. For future devices such as ITER, operating at 10-15 keV, heating directed specifically at the islands is necessary to prevent them from growing under the mechanisms of the Gates-model. This suppresses the island growth as shown in figure 4.13 and thereby increases the stable region under the F-function as shown in equation (4.5). Future and current devices such as TEXTOR and ASDEX-Upgrade use auxiliary heating anyway, because Ohmic heating alone is not sufficient to carry them to their operating temperatures.

5.4 Concrete suggestions for improvements

The numerical work presented in this thesis consists mainly of parameter scans and finding the threshold behavior. Increasing the accuracy by which the island growth and temperature quench resemble real experiments, higher toroidal harmonics should be included during the simulations. Qualitatively similar observations are expected in the enhanced island growth and threshold behavior. However, quantitatively it is expected that the magnetic islands will be narrower, because additional ones will be present at intermediate rational surfaces. Furthermore, the convergence scan in appendix A indicates that numerical instabilities can be avoided by increasing the number of harmonics. This requires more computational time in possible successive research projects. The set of simulation settings and results that are obtained in `JOREK` provide a starting point.

Better comparisons with experiments will be possible by inclusion of multiple impurity species. For mixtures the effect of flat regimes in the F-function should be investigated to see if at similar temperatures and densities observed disruptions can be explained with the Gates-model. In `JOREK` this would ideally be done by adding more density variables, each corresponding to a single species, to accurately include transport and interactions between species as well. Increasing the number of equations to solve for lets the problem become computationally expensive very fast. An easier to implement alternative is to include an option in which a generic impurity species is used with an artificial radiation curve constructed by an array of user defined impurity species and concentrations. The resulting curve would be a linear combination of the OPEN-ADAS radiation curves. Transport can not be accurately taken into account in such simulations, but solely for radiation purposes this would suffice.

To quantitatively distinguish between the density limit due to the edge radiation and the Greenwald limit, a diagnostic to measure the total radiative cooling and Ohmic heating within the separatrices of the islands should be added to the island finding routine in `JOREK`. Comparisons between the total power balance and power balance inside the islands should give a transition as a function of temperature and density. This then likely gives the mechanism that triggers the island growth and can be used to better explain the parameter space plots of figure 4.8. Furthermore, the time-evolution of the radiated power can help quantify nonlinear effects in the thermal runaway due to the temperature dependency of the radiation rate.
In the same diagnostic, the temperature gradients and heat flux through the separatrix can be calculated during the tracing of the magnetic field line close to the separatrix. At different times this tells at which times and to which degree the separatrix acts as an isolator and the heat balance from the Gates-model holds.

The way current drive is implemented in `JOREK` should eventually be altered if one wants to investigate the tearing mode with added impurities at reactor relevant temperatures ($T_e > 500\,\mathrm{eV}$) and thus at longer timescales. In the present state, the current source j_0 should be either disabled or have a fixed temperature dependence, which are both inaccurate on large timescales. A proposed way is replace the current source profile by a fully consistent inductive drive. The current is then driven at the edge of the plasma, based on the internal inductance l_i and distribution characterized by the resistivity. This method gives an additional numerical value (l_i) that can be used in comparisons with experiments, for which this value is often reported.

Additional unaddressed matters

Profiles in `JOREK` simulations are never exactly comparable due to the fact that the initial profiles for n, T and j are coupled by the Grad-Shafranov equation (3.24). No fully independent tuning of a single parameter is possible without it affecting the others. The q-profile is affected as well, as the enclosed current is used for its calculation.

Impurity transport effects are intentionally neglected by choosing a uniform spatial distribution. Moreover, the sudden appearance of impurities at the start of the tearing mode growth is in no way physical. The questions on why and how the impurities should have sufficient concentrations around the $q = 2$ surfaces can not be answered in this thesis, but are crucial in linking the Gates-model to real experiments.

Besides particle transport, the radial heat transport does not necessarily reflect experimental situations. Values of the corresponding coefficient are chosen solely as to keep the temperature profile stable at a desirable value. The ratio between heat conductivities is chosen in agreement with literature.

Finally, no questions are addressed or answered about the situations in which the tearing mode grows. This work only shows simulations for cases for which is known that the tearing mode is unstable, even without impurities. Starting from saturated cases or with seed islands are two different scenarios which should be done in future studies.

Gradually increasing the density during runs

The cases investigated in this thesis all start at the beginning of the tearing mode growth, with a constant density. However, in experiments there may be already small seed islands presents in a saturated state. Increasing the density during a simulation is of interest because during experiments the plasma density is often increased until the disruption at the Greenwald density limit is found. Besides this, it will be interesting to investigate whether nonlinear growth occurs similar to that in [40] for saturated islands. Additionally, the existence of an overshoot and transition to a stochastic regime needs to be studied for these scenarios. In order to simulate these, control over both plasma and impurity density is needed. Initially simulations in which the plasma density is increased uniformly at a fixed impurity fraction are of interest, to see whether similar sharp transitions as in figure 4.6 are found. Such simulations require additions to `JOREK`, which are not implemented during this research due to time constraints. However, a global description of the necessary dual source is given here.

Using the existing density source, ρ can be increased at a fixed ρ_{imp}, meaning that the impurity fraction decreases as the total mass density goes up. This can be used to study the effect of fueling with a 100% deuterium. For the proposed additional density source, the impurity to electron fraction f_{imp} should remain constant:

$$\begin{aligned}\frac{n_{\mathrm{imp}}}{n_{\mathrm{e}}} &= \frac{n_{\mathrm{imp}}}{n_{\mathrm{D}} + \langle Z\rangle_{\mathrm{imp}} n_{\mathrm{imp}}} = f_{\mathrm{imp}} = \text{constant} \\ &= \frac{2n_{\mathrm{imp}}}{n_{\mathrm{tot}} + \Big(\langle Z\rangle_{\mathrm{imp}} - 1\Big) n_{\mathrm{imp}}} \\ &= \frac{2\rho_{\mathrm{imp}} n_0 \frac{m_{\mathrm{D}}}{m_{\mathrm{imp}}}}{\frac{2m_{\mathrm{D}}}{(\rho+\alpha\rho_{\mathrm{imp}})} + \Big(\langle Z\rangle_{\mathrm{imp}} - 1\Big) \rho_{\mathrm{imp}} n_0 \frac{m_{\mathrm{D}}}{m_{\mathrm{imp}}}} \\ &= \frac{2\rho_{\mathrm{imp}} \left(\rho + \alpha\rho_{\mathrm{imp}}\right) n_0}{2m_{\mathrm{imp}} + \Big(\langle Z\rangle_{\mathrm{imp}} - 1\Big) \rho_{\mathrm{imp}} \left(\rho + \alpha\rho_{\mathrm{imp}}\right) n_0}.\end{aligned} \tag{5.1}$$

This is a more difficult expression than expected, nevertheless a simple quadratic equation can be obtained from this relating ρ_{imp} directly to ρ:

$$\alpha\rho_{\mathrm{imp}}^2 + \rho\rho_{\mathrm{imp}} - \frac{2m_{\mathrm{imp}}}{n_0} \frac{f_{\mathrm{imp}}}{2 - f_{\mathrm{imp}} \Big(\langle Z\rangle_{\mathrm{imp}} - 1\Big)} = 0. \tag{5.2}$$

6. Conclusion

The main purpose of this research has been to validate and expand on a proposed explanation of the empirical Greenwald density limit: A semi-analytical model in which magnetic island growth is enhanced by net radiative cooling, triggering the disruption of the fusion plasma.

In nonlinear `JOREK` simulations, a clear transition is observed in the island evolution when the electron density is increased to values 20% above the empirical Greenwald density. In these cases, the radiation due to impurities inside the island separatrix is found to overcome the local Ohmic heating. This leads to enhanced growth of the islands, stochastisation of the magnetic field and quenching of the temperature profile. With only a single impurity type included, both numerically and semi-analytically a transition is found that is highly dependent on electron temperature, impurity density and type. In these cases, the Gates-model is suitable to predict plasma stability but not unifiable with the Greenwald density limit.

From a local heat balance inside the islands an expression is found that is able to predict the cooling and enhanced nonlinear growth of the islands. The inclusion of multiple impurity species eradicates the temperature dependence and diminishes the impurity dependence for sufficiently high fractions. With $F \approx 1$ for these cases, a direct reflection of the global limit is found in terms of local electron and current densities.

Using profiles corresponding to Furth-Rutherford-Selberg equilibria, the radial locations of where the local electron and current densities are equal to their globally averaged values are calculated. Both locations are found to match the position of the magnetic islands for a wide range of profile shapes and different devices. Under this condition, combined with F close to unity, the local power balance $n_\mathrm{e} = Fj$ can be rewritten as $\overline{n}_\mathrm{e} = \overline{j}$ and the full formulation of the Greenwald density limit is consistently explained.

The suppression of island growth is shown to be more effective for localized heating, which is consistent with the conceptual picture of thermally isolated islands. For current and future experiments a pathway is presented to exceed the Greenwald density limit by creating stable regimes by control of impurity species and fractions, or by specifically heating of the $^2\!/_1$-islands.

Higher toroidal resolution will increase the physical accuracy of perturbations that describe the islands and allow for simulation of full disruptions. It is identified that modifications in the impurity description and current drive are needed in `JOREK` to allow direct comparison with real experiments.

7. Acknowledgments

First and foremost, I would like to thank my supervisors Guido Huijmans and Leon Kamp who helped to provide structure to this project.

Special thanks is in place for my daily supervisor Daan van Vugt. Without his help this project would not have been possible. Discussions with him served as a catalyst for this research.

I thank Di Hu for the creation and documentation of `JOREK` model 501, as well as his suggestions for usage and improvements.

Further I would like to thank Peter de Vries for his views on experiments and density limits and Stijn Franssen and Stefan Kempers for feedback on the written deliverables.

Bibliography

[1] P. D. United Nations, Department of Economic and Social Affairs, “World Population Prospects: The 2017 Revision, Online Demographic Profiles,” 2017. 3

[2] J. Asafu-Adjaye, “The relationship between energy consumption, energy prices and economic growth: Time series evidence from Asian developing countries,” *Energy Economics*, vol. 22, pp. 615–625, dec 2000. 3

[3] C. C. Lee, “Energy consumption and GDP in developing countries: A cointegrated panel analysis,” *Energy Economics*, vol. 27, pp. 415–427, may 2005. 3

[4] S. Shafiee and E. Topal, “When will fossil fuel reserves be diminished?,” *Energy Policy*, vol. 37, pp. 181–189, jan 2009. 3

[5] D. A. Lashof and D. R. Ahuja, “Relative contributions of greenhouse gas emissions to global warming,” *Nature*, vol. 344, pp. 529–531, apr 1990. 3

[6] J. H. Diaz, “The influence of global warming on natural disasters and their public health outcomes.,” *American journal of disaster medicine*, vol. 2, no. 1, pp. 33–42, 2007. 3

[7] M. van Aalst, “The impacts of climate change on the risk of natural disasters,” *Disasters*, vol. 30, no. 1, pp. 5–18, 2006. 3

[8] B.P St. Review, “— Energy economics — Home (B.P Statistical Review of World Energy),” 2018. 4

[9] United Nations, “What is the Paris agreement?,” 2015. 3

[10] C. F. Schleussner, J. Rogelj, M. Schaeffer, T. Lissner, R. Licker, E. M. Fischer, R. Knutti, A. Levermann, K. Frieler, and W. Hare, “Science and policy characteristics of the Paris Agreement temperature goal,” sep 2016. 3

[11] N. J. Lopes Cardozo, A. G. Lange, and G. J. Kramer, “Fusion: Expensive and Taking Forever?,” *Journal of Fusion Energy*, vol. 35, no. 1, pp. 94–101, 2016. 3

[12] D. J. MacKay, *Sustainable Energy - without the hot air.* UIT Cambridge, 2008. 3

[13] F. Tavassoli, “Eurofer steel, development to full code qualification,” in *Procedia Engineering*, vol. 55, pp. 300–308, Elsevier, jan 2013. 4

[14] J. D. Huba, “NRL Plasma Formulary,” tech. rep., 2007. 6

[15] J. J. McNally, K. Rothe, and R. Sharp, “Fusion reactivity graphs and tables for charged particle reactions,” tech. rep., Oak Ridge National Laboratory (ORNL), Oak Ridge, TN (United States), aug 1979. 6

[16] J. P. Freidberg, *Plasma physics and fusion energy.* 2007. 5, 7, 10, 18

[17] David J. Griffiths, *Introduction to Electrodynamics.* 3 ed., 2013. 7

[18] T. Meulenbroeks and S. Fransen, “Tokamak coil configuration,” 2019. 8

[19] M. Greenwald, J. L. Terry, S. M. Wolfe, G. H. Neilson, M. G. Zwebellben, S. M. Kaye, and G. H. Neilson, “A new look at density limits in tokamaks,” *Nuclear Fusion*, vol. 28, no. 12, pp. 2207–2219, 1988. 9, 11, 12, 55, 69

[20] M. Greenwald, “Density limits in toroidal plasmas,” 2001. 9, 13

[21] F. C. Schuller, “Disruptions in tokamaks,” *Plasma Physics and Controlled Fusion*, vol. 37, no. 11A, pp. 135–62, 1995. 10, 69

[22] J. Wesson, R. Gill, M. Hugon, and Schu, “Disruptions in JET,” *Nuclear Fusion*, vol. 29, no. 4, p. 641, 1989. 10, 64, 69

[23] T. Kudyakov, K. H. Finken, M. W. Jakubowski, M. Lehnen, Y. Xu, B. Schweer, T. Toncian, G. Van Wassenhove, and O. Willi, “Spatially and temporally resolved measurements of runaway electrons in the TEXTOR tokamak,” *Nuclear Fusion*, vol. 48, p. 122002, dec 2008. 10

[24] G. Pautasso, D. Coster, T. Eich, J. C. Fuchs, O. Gruber, A. Gude, A. Herrmann, V. Igochine, C. Konz, B. Kurzan, K. Lackner, T. Lunt, M. Marascheck, A. Mlynek, B. Reiter, V. Rohde, Y. Zhang, X. Bonnin, M. Beck, and G. Prausner, “Disruption studies in ASDEX Upgrade in view of ITER,” *Plasma Physics and Controlled Fusion*, vol. 51, p. 124056, dec 2009. 10

[25] F. C. Schuller, “Disruptions in tokamaks,” *Plasma Physics and Controlled Fusion*, vol. 37, no. 11A, pp. 135–62, 1995. 11

[26] M. Jakobs, *Fusion energy : burning questions*. PhD thesis, Eindhoven University of Technology, 2016. 10

[27] F. Troyon, R. Gruber, H. Saurenmann, S. Semenzato, and S. Succi, “MHD-limits to plasma confinement,” *Plasma Physics and Controlled Fusion*, vol. 26, pp. 209–215, jan 1984. 11

[28] J. Rapp, P. C. De Vries, F. C. Schüller, M. Z. Tokar’, W. Biel, R. Jaspers, H. R. Koslowski, A. Krämer-Flecken, A. Kreter, M. Lehnen, A. Pospieszczyk, D. Reiser, U. Samm, and G. Sergienko, “Density limits in TEXTOR-94 auxiliary heated discharges,” *Nuclear Fusion*, vol. 39, no. 6, pp. 765–776, 1999. 11, 13, 55, 64, 68, 69, 70

[29] P. C. de Vries, *Magnetic islands in tokamak plasmas*. PhD thesis, 1997. 11, 68, 69

[30] M. Greenwald, “Density limits in toroidal plasmas,” *Plasma physics and control fusion*, vol. 44, no. 2002, pp. 1–55, 2002. 12, 14

[31] M. Lehnen, D. J. Campbell, S. Maruyama, J. A. Snipes, P. C. De Vries, and L. Zabeo, “Control, detection and mitigation of disruptions on ITER,” in *Proceedings - Symposium on Fusion Engineering*, vol. 2016-May, pp. 1–8, IEEE, may 2016. 13

[32] M. Lehnen, K. Aleynikova, P. B. Aleynikov, D. J. Campbell, P. Drewelow, N. W. Eidietis, Y. Gasparyan, R. S. Granetz, Y. Gribov, N. Hartmann, E. M. Hollmann, V. A. Izzo, S. Jachmich, S. H. Kim, M. Kočan, H. R. Koslowski, D. Kovalenko, U. Kruezi, A. Loarte, S. Maruyama, G. F. Matthews, P. B. Parks, G. Pautasso, R. A. Pitts, C. Reux, V. Riccardo, R. Roccella, J. A. Snipes, A. J. Thornton, and P. C. De Vries, “Disruptions in ITER and strategies for their control and mitigation,” *Journal of Nuclear Materials*, vol. 463, pp. 39–48, aug 2015. 13

[33] M. A. Mahdavi, T. H. Osborne, A. W. Leonard, M. S. Chu, E. J. Doyle, M. E. Fenstermacher, G. R. McKee, G. M. Staebler, T. W. Petrie, M. R. Wade, S. L. Allen, J. A. Boedo, N. H. Brooks, R. J. Colchin, T. E. Evans, C. M. Greenfield,

G. D. Porter, R. C. Isler, R. J. La Haye, C. J. Lasnier, R. Maingi, R. A. Moyer, M. J. Schaffer, P. G. Stangeby, J. G. Watkins, W. P. West, D. G. Whyte, and N. S. Wolf, “High performance H mode plasmas at densities above the Greenwald limit,” *Nuclear Fusion*, vol. 42, no. 1, pp. 52–58, 2002. 13

[34] K. Borrass, “Disruptive tokamak density limit as scrape-off layer/divertor phenomenon,” *Nuclear Fusion*, vol. 31, no. 6, pp. 1035–1051, 1991. 14

[35] D. A. Gates and L. Delgado-Aparicio, “Origin of tokamak density limit scalings,” *Physical Review Letters*, vol. 108, no. 16, pp. 1–4, 2012. 14, 15, 48

[36] D. A. Gates, L. Delgado-Aparicio, and R. B. White, “Physics of radiation-driven islands near the tokamak density limit,” *Nuclear Fusion*, vol. 53, no. 6, 2013. 14, 15

[37] D. A. Gates, D. P. Brennan, L. Delgado-Aparicio, and R. B. White, “The tokamak density limit: A thermo-resistive disruption mechanism,” *Physics of Plasmas*, vol. 22, no. 6, p. 60701, 2015. 14, 48

[38] R. B. White, D. A. Gates, and D. P. Brennan, “Thermal island destabilization and the Greenwald limit,” *Physics of Plasmas*, vol. 22, no. 2, p. 22514, 2015. 14, 15, 20

[39] Q. Teng, D. P. Brennan, L. Delgado-Aparicio, D. A. Gates, J. Swerdlow, and R. B. White, “A predictive model for the tokamak density limit,” *Nuclear Fusion*, vol. 56, no. 10, 2016. 14, 15, 48, 49, 51, 61, 66, 67, 68

[40] Q. Teng, N. Ferraro, D. Gates, and R. White, “Nonlinear simulations of thermo-resistive tearing mode formalism of the density limit,” *Nuclear Fusion*, vol. 58, p. 106024, 2018. 14, 15, 16, 18, 19, 43, 55, 61, 63, 64, 66, 67, 72

[41] L. Spitzer and R. Harm, “Transport Phenomena in a Nonuniform Slightly Ionized Gas,” *Progress of Theoretical Physics*, vol. 27, no. 6, pp. 1128–1136, 1962. 14, 20, 26, 28, 48

[42] H. P. Furth, P. H. Rutherford, and H. Selberg, “Tearing mode in the cylindrical tokamak,” *Physics of Fluids*, vol. 16, no. 7, pp. 1054–1063, 1973. 15, 61, 62, 64

[43] D. Hu, E. Nardon, M. Lehnen, G. T. Huijsmans, and D. C. Van Vugt, “3D non-linear MHD simulation of the MHD response and density increase as a result of shattered pellet injection,” *Nuclear Fusion*, vol. 58, no. 12, 2018. 16, 22, 67

[44] D. D. Schnack, *Lectures in Magnetohydrodynamics*, vol. 780 of *Lecture Notes in Physics*. Berlin, Heidelberg: Springer Berlin Heidelberg, 2009. 18

[45] M. Hölzl, “Diffusive Heat Transport across Magnetic Islands and Stochastic Layers in Tokamaks,” 2010. 18, 21, 88, 89

[46] X. Garbet, Y. Idomura, L. Villard, and T. H. Watanabe, “Gyrokinetic simulations of turbulent transport,” 2010. 19

[47] H. P. Furth, J. Killeen, and M. N. Rosenbluth, “Finite-Resistivity Instabilities of a Sheet Pinch,” *Physics of Fluids*, vol. 6, no. 4, p. 459, 1963. 19

[48] R. Fitzpartrick, “Linear Tearing Mode Theory,” 2011. 19

[49] P. H. Rutherford, “Nonlinear growth of the tearing mode,” *Physics of Fluids*, vol. 16, no. 11, pp. 1903–1908, 1973. 20

[50] J. WESSON, “HYDROMAGNETIC STABILITY OF TOKAMAKS,” *Nuclear Fusion*, vol. 18, p. 1, 1978. 20

[51] R. Fitzpatrick, “Helical temperature perturbations associated with tearing modes in tokamak plasmas,” *Physics of Plasmas*, vol. 2, no. 3, pp. 825–838, 1995. 21

[52] C. C. Hegna and J. D. Callen, “Interaction of bootstrap-current-driven magnetic islands,” *Physics of Fluids B*, vol. 4, pp. 1855–1866, mar 1992. 21

[53] R. J. La Haye, “Neoclassical tearing modes and their control,” in *Physics of Plasmas*, vol. 13, p. 055501, American Institute of Physics, may 2006. 21

[54] G. T. A. Huysmans and O. Czarny, “MHD stability in X-point geometry: Simulation of ELMs,” in *Nuclear Fusion*, vol. 47, pp. 659–666, 2007. 22

[55] D. Meshcheriakov, M. Hoelzl, V. Igochine, S. Fietz, F. Orain, G. T. Huijsmans, M. Maraschek, M. Dunne, R. McDermott, H. Zohm, K. Lackner, and S. Günter, “Numerical study of tearing mode seeding in tokamak X-point plasma,” *Physics of Plasmas*, vol. 26, no. 4, p. 102014, 2019. 22

[56] N. Murphy, “Reduced MHD,” 2014. 22

[57] O. Czarny and G. Huysmans, “Bézier surfaces and finite elements for MHD simulations,” *Journal of Computational Physics*, vol. 227, pp. 7423–7445, aug 2008. 22

[58] F. Ryter, K. Buchl, C. Fuchs, O. Gehre, O. Gruber, A. Herrmann, A. Kallenbach, M. Kaufmann, W. Koppendorfer, F. Mast, V. Mertens, R. Neu, S. De Pena Hempel, K. H. Steuer, and H. Zohm, “H-mode results in ASDEX Upgrade,” *Plasma Physics and Controlled Fusion*, vol. 36, pp. A99–A104, jul 1994. 28

[59] V. P. Bhatnagar, J. Lingertat, R. Barnsley, P. Breger, J. P. Christiansen, S. Clement, J. G. Cordey, S. J. Davies, J. K. Ehrenberg, L. G. Eriksson, G. M. Fishpool, P. J. Harbour, L. D. Horton, J. Jacquinot, H. J. Jäckel, K. Lawson, C. G. Lowry, C. F. Maggi, G. F. Matthews, R. D. Monk, D. P. O'Brien, V. V. Parail, E. Righi, G. Saibene, R. Sartori, B. Schunke, A. C. Sips, M. F. Stamp, D. F. Start, and K. Thomsen, “Edge localized modes and edge pedestal in NBI and ICRF heated H, D and T plasmas in JET,” *Nuclear Fusion*, vol. 39, pp. 353–367, mar 1999. 28

[60] H. Summers, “The ADAS User Manual, version 2.6,” 2004. 30

[61] M. A. Dopita and R. S. Sutherland, “Collisional Ionization Equilibrium,” pp. 101–123, Springer, Berlin, Heidelberg, 2013. 30

[62] M. O'mullane, “Background to ADAS,” tech. rep., 2012. 30

[63] D. C. V. Vugt, “Nonlinear coupled MHD-kinetic particle simulations of heavy impurities in tokamak plasmas,” jul 2019. 30, 69, 86

[64] P. G. Carolan and V. A. Piotrowicz, “The behaviour of impurities out of coronal equilibrium,” *Plasma Physics*, 1983. 30, 69

[65] S. P. Hirshman and D. J. Sigmar, "Neoclassical transport of impurities in tokamak plasmas," sep 1981. 30

[66] T. Fülöp and H. Nordman, "Turbulent and neoclassical impurity transport in tokamak plasmas," *Physics of Plasmas*, vol. 16, p. 032306, mar 2009. 30

[67] V. Shafranov, "Plasma Equilibrium in Magnetic Field," *Reviews of Plasma Physics*, vol. 2, pp. 343–365, 1966. 32

[68] P. C. De Vries, G. Pautasso, E. Nardon, P. Cahyna, S. Gerasimov, J. Havlicek, T. C. Hender, G. T. Huijsmans, M. Lehnen, M. Maraschek, T. Markovič, and J. A. Snipes, "Scaling of the MHD perturbation amplitude required to trigger a disruption and predictions for ITER," *Nuclear Fusion*, vol. 56, p. 026007, feb 2015. 43, 66

[69] F. W. Perkins and R. A. Hulse, "On the Murakami density limit in tokamaks and reversed-field pinches," *Physics of Fluids*, vol. 28, pp. 1837–1844, sep 1985. 48

[70] R. Aymar, P. Barabaschi, and Y. Shimomura, "The ITER design," *Plasma Physics and Controlled Fusion*, vol. 44, pp. 519–565, may 2002. 64

[71] V. Mertens, M. Kaufmann, J. Neuhauser, J. Schweinzer, J. Stober, K. Büchl, O. Gruber, G. Haas, A. Herrmann, A. Kallenbach, and M. Weinlich, "High density operation close to Greenwald limit and H mode limit in ASDEX Upgrade," *Nuclear Fusion*, vol. 37, pp. 1607–1614, nov 1997. 64

[72] M. Keilhacker, A. Gibson, C. Gormezano, and P. H. Rebut, "The scientific success of JET," tech. rep., 2001. 64

[73] E. Nardon, A. Fil, M. Hoelzl, and G. Huijsmans, "Progress in understanding disruptions triggered by massive gas injection via 3D non-linear MHD modelling with JOREK," jan 2017. 67

[74] I. Krebs, M. Hölzl, K. Lackner, and S. Günter, "Nonlinear excitation of low-n harmonics in reduced magnetohydrodynamic simulations of edge-localized modes," *Physics of Plasmas*, vol. 20, p. 082506, aug 2013. 67

[75] A. Pau, A. Fanni, B. Cannas, S. Carcangiu, G. Sias, P. Sparapani, E. Alessi, C. Sozzi, M. Baruzzo, E. Joffrin, P. J. Lomas, A. Murari, and F. Rimini, "A machine learning approach towards disruption prediction and avoidance on JET," in *45th EPS Conference on Plasma Physics, EPS 2018*, vol. 2018-July, pp. 713–716, 2018. 68

[76] B. Lipschultz, "Review of MARFE phenomena in tokamaks," *Journal of Nuclear Materials*, pp. 15–25, 1987. 69

[77] G. Goh, "Why Momentum Really Works.," *Distill*, vol. 2, p. e6, apr 2017. 88

[78] H. H. Rosenbrock, "An Automatic Method for Finding the Greatest or Least Value of a Function," *The Computer Journal*, 1960. 89

[79] J. A. Nelder and R. Mead, "A Simplex Method for Function Minimization," *The Computer Journal*, 1965. 89

A. Convergence of simulations

A.1 Number of harmonic modes convergence

For the case with $n_\mathrm{e} = 0.7 \times 10^{20}$ m^{-3}, $n_\mathrm{Ne}/n_\mathrm{e} = 0.01$ and $T_\mathrm{e} = 100$ eV, different amounts of harmonics are included in the Fourier decomposition for the toroidal dependencies of the quantities. The magnetic energy in the first harmonics $E_\mathrm{mag,1}$ is given in figure A.1 for the transition from the linear to nonlinear phase. Each increase of n_tor by 2 corresponds to an extra pair of sines and cosines added to the decomposition: n_tor = 3 has a single sine and cosine, n_tor = 5 has a an additional sine and cosine squared, etc. The simulations seem to be converged when at least n_tor = 5 is used. The temperature and current density profiles at the midplane for the time indicated by the black dotted line, shown in figure A.2, confirm this. Here it seems that numerical oscillations around the axis can be prevented using higher order modes, while increasing the details around the magnetic island where the profile flattening shows. It is however unknown whether the extra features between $0.4 < \psi_\mathrm{N} < 0.6$ have a physical or numerical origin.

Despite these results, the runs with n_tor = 3 are used for the research done in this thesis, since this allows for the use of a direct matrix solver. For more harmonics, preconditioning of the system using an iterative generalized minimal residual method (`gmres`) is needed. To satisfy similar convergence criteria as during the linear phase, the typical time step needs to be decreased by up to a factor 100. Overall this increases the time to simulate the nonlinear evolution of the tearing mode from the order of days to multiple weeks/months.

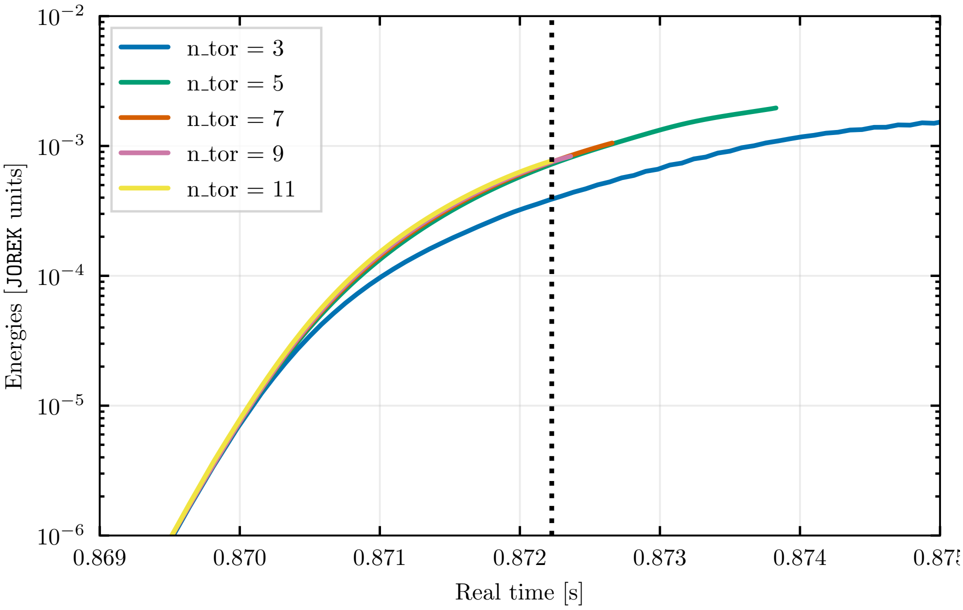

Figure A.1: The magnetic energy in the first harmonics $E_\mathrm{mag,1}$ is plotted for the end of the linear and part of the nonlinear phase. Convergence is reached when at least n_tor = 5 is used.

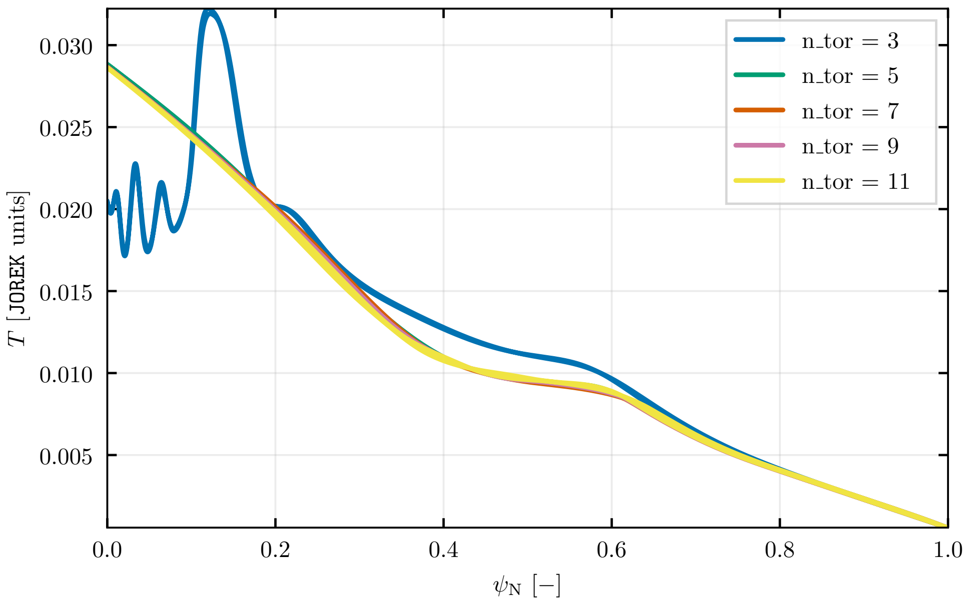

(a) Temperature profile

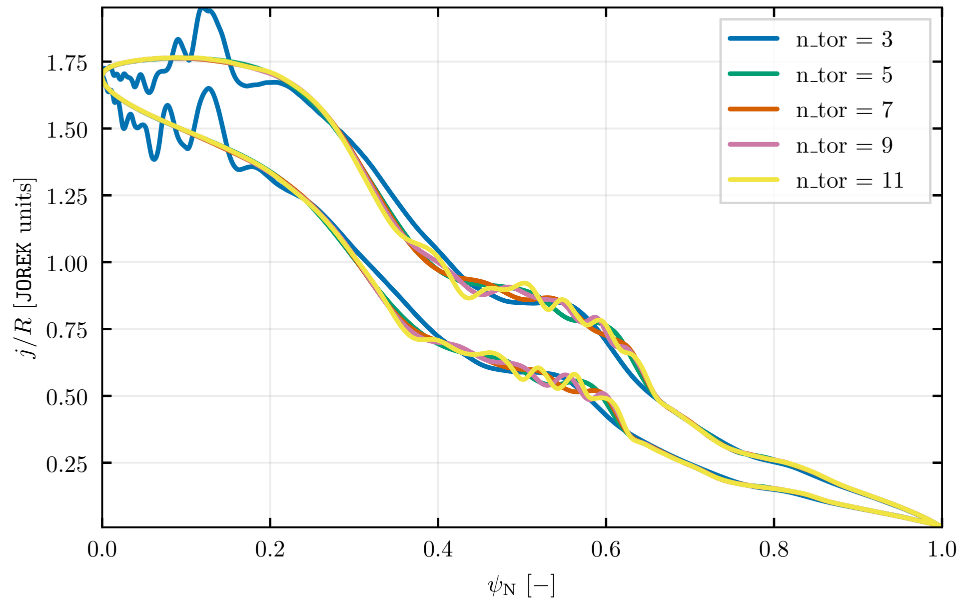

(b) Current density profile

Figure A.2: The midplane temperature and current density profiles in `JOREK` units are plotted for different number of toroidal harmonics included in the simulations. For the current density two curves show for the two midplane sections on the inner and outer side with respect to the magnetic axis, due to the $1/R$-dependency. Oscillations around the axis can be suppressed while the additional features emerge around the magnetic islands when using at least n_tor = 5, at the cost of increasing the simulation duration significantly.

A.2 Poloidal grid size convergence

The number of elements in the poloidal grid is varied by scans over the number of elements in the radial direction n_flux and in the poloidal direction n_theta. This is done for parameter settings $n_\mathrm{e} = 0.5 \times 10^{20}$ m^{-3}, $n_\mathrm{Ne}/n_\mathrm{e} = 0.0$ and $T_\mathrm{e} = 50$ eV. With either n_flux ≤ 76 or n_theta ≤ 51, sudden jumps in various components are observed. For the simulations in which these jumps are absent, the magnetic energy $E_{\mathrm{mag},1}$ is plot in figure A.3. Here, no significant dependence is found on the number of grid cells during either linear or nonlinear phase. For the simulations in this thesis, a grid is used with n_flux = 126 and n_theta ≤ 76.

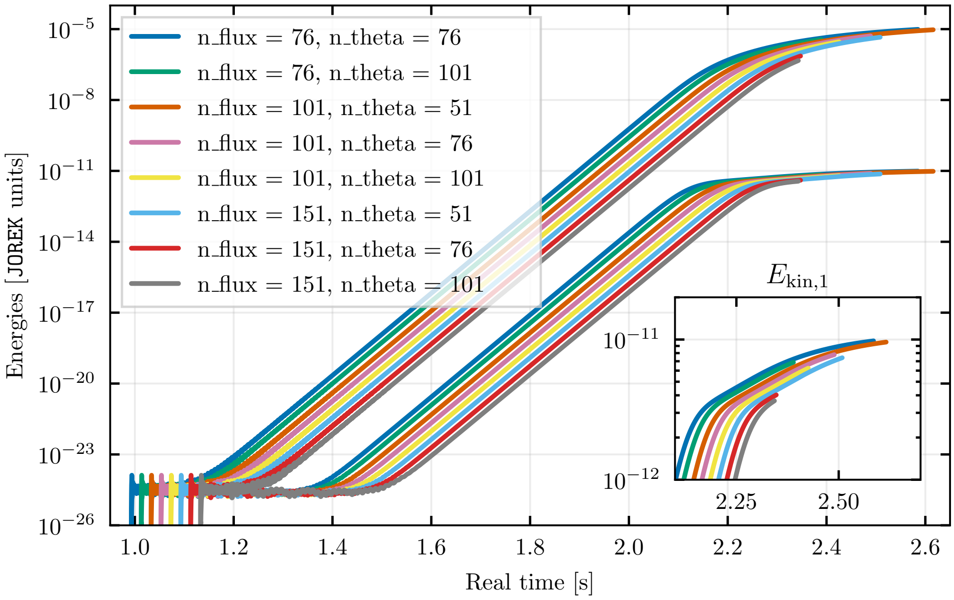

Figure A.3: The magnetic and kinetic energies in the first harmonics $E_{\mathrm{mag},1}$ and $E_{\mathrm{kin},1}$ are plotted for the end of the linear and part of the nonlinear phase, for different number of radial and poloidal elements n_flux and n_theta. The insert shows a closeup of the nonlinear phase of the kinetic energy. The curves show no significant variation during either phase. To improve readability of the figure, each line is shifted 20 ms in time with respect to its neighbor.

A.3 Time step convergence

For parameter settings $n_\mathrm{e} = 0.5 \times 10^{20}$ m^{-3}, $n_\mathrm{Ne}/n_\mathrm{e} = 0.0$ and $T_\mathrm{e} = 50$ eV, the time step in `JOREK` units is varied. The magnetic energy $E_{\mathrm{mag},1}$ is plot in figure A.4. For the tearing mode growth typical time steps of $50 - 500$ are chosen for central temperatures of 50 ev or 500 eV respectively. This is justifiable, because with an increase of T by a factor 10, the resistive timescale increases with a factor $10^{3/2} \approx 30$. For runs with high impurity concentrations and rapidly evolving temperature profiles, the timestep is typically decreased by a factor 10 again.

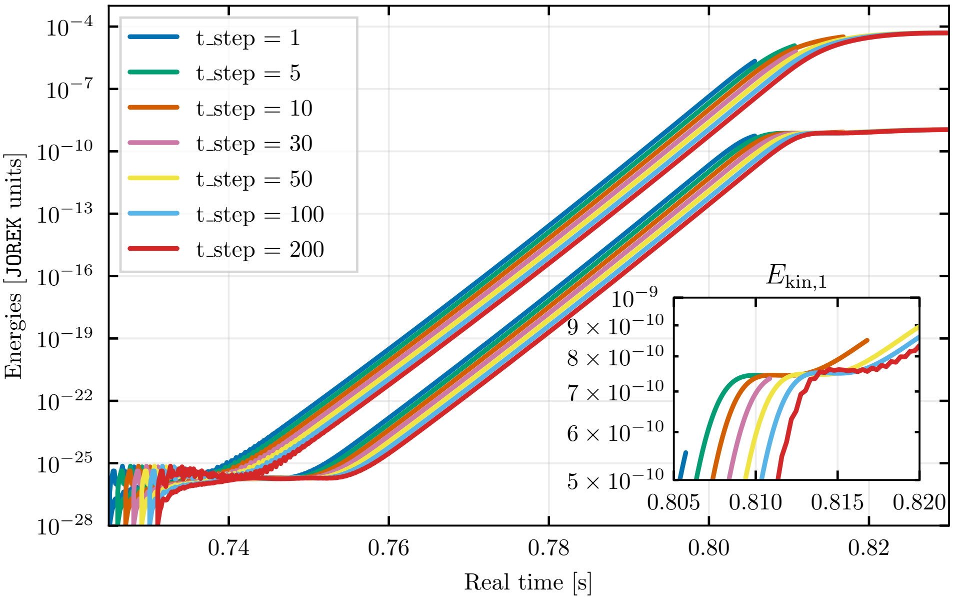

Figure A.4: The magnetic and kinetic energies in the first harmonics $E_{\mathrm{mag},1}$ and $E_{\mathrm{kin},1}$ is plotted for varying `JOREK` time step sizes. The insert shows a closeup of the nonlinear phase of the kinetic energy. The curves show no significant variation during either phase, with the exception of the largest of 200 showing oscillatory behavior. To improve readability of the figure, each line is shifted 1.0 ms in time with respect to its neighbor.

A.4 Comparison with axisymmetric case

The case with localized impurities and lowered boundary temperature from section 4.3.1 is compared with an identical, but axisymmetric setup, i.e. n_tor = 1. Further settings are $n_\mathrm{e} = 0.7 \times 10^{20}$ m^{-3}, $n_\mathrm{Ne}/n_\mathrm{e} = 0.01$ and $T_\mathrm{e} = 100$ eV. The magnetic energy $E_{\mathrm{mag},1}$ is plot in figure A.5. Up to the start of the nonlinear growth phase of the tearing mode, the axisymmetric components of both cases are nearly identical. At the onset of the nonlinear phase, the axisymmetric components (with n_tor = 3) begin to deviate as they are affected by the tearing mode, while the other axisymmetric energies (with n_tor = 1) continue the trend. The sudden jump in kinetic energy at 0.576 s is due to the addition of impurities. Here the total plasma mass instantaneously increases as ρ_imp is made non-zero, while parallel flows are unaltered.

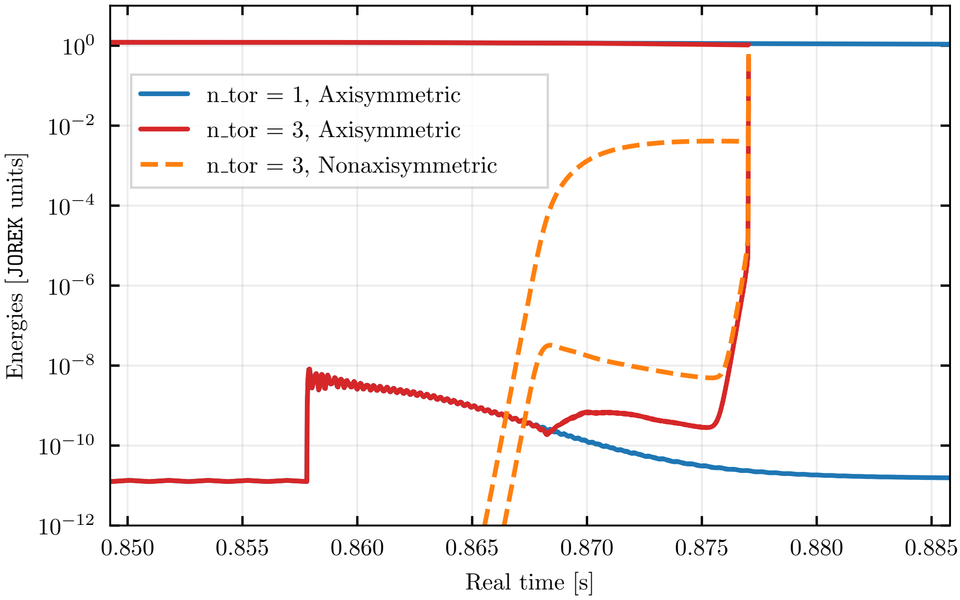

Figure A.5: The energies of simulations with and without included nonlinear components are compared. Until the start of the nonlinear phase, the axisymmetric energies are nearly identical.

B. Island finding routine

This appendix describes the methods used to get from a `JOREK` restart file to (normalized) island width that is used in the results section of this thesis.

B.1 Tracing magnetic fieldlines

First a method is needed to accurately trace magnetic field lines and store their trajectories from the `JOREK` restart file. The majority of this method is written by Daan van Vugt [63]. Closed expressions for the magnetic field $\mathbf{B}$ are not available, only local information at a coordinate can be obtained by interpolation of ψ and its spatial averages. The magnetic field at location $\mathbf{x} = (R, Z, \phi)$ is then obtained from equation (3.1) as

$$\mathbf{B} = (B_R, B_Z, B_\phi) = \left(\frac{1}{R}\frac{\partial\psi}{\partial Z}, -\frac{1}{R}\frac{\partial\psi}{\partial R}, \frac{F_0}{R}\right). \tag{B.1}$$

This expression is normalized to retain only information on directional components like

$$\hat{\mathbf{B}} = \frac{\mathbf{B}}{\|\mathbf{B}\|} = \left(\frac{B_R}{\|\mathbf{B}\|}, \frac{B_Z}{\|\mathbf{B}\|}, \frac{B_\phi}{\|\mathbf{B}\|}\right) = \left(\hat{B}_R, \hat{B}_Z, \hat{B}_\phi\right). \tag{B.2}$$

Based on the single starting point, the tracing routine is set-up using the explicit first-order Euler stepping method, which relates the new location to the old as

$$\mathbf{x}_{\text{new}} = \mathbf{x}_{\text{old}} + \hat{\mathbf{B}}\left(\mathbf{x}_{\text{old}}\right)\Delta x, \tag{B.3}$$

with Δx as step size. For the position in cylindrical coordinates in `JOREK` is implemented as

$$\begin{aligned} R_1 &= \sqrt{\left(R_0 + \hat{B}_{R,0}\Delta x\right)^2 + \left(\hat{B}_{\phi,0}\Delta x\right)^2} \\ Z_1 &= Z_0 + \hat{B}_{Z,0}\Delta x \\ \phi_1 &= \phi_0 + \arcsin\left(\frac{\hat{B}_{R,0}\Delta x}{R_1}\right). \end{aligned} \tag{B.4}$$

With the first two values known, the explicit second-order convergent Adams-Bashforth method will be used for all subsequent steps:

$$\mathbf{x}_{n+2} = \mathbf{x}_{n+1} + \left(\frac{3}{2}\hat{\mathbf{B}}\left(\mathbf{x}_{n+1}\right) - \frac{1}{2}\hat{\mathbf{B}}\left(\mathbf{x}_n\right)\right)\Delta x. \tag{B.5}$$

Again for this system, this translates to

$$\begin{aligned} R_{n+2} &= R_{n+1} + \left(\frac{3}{2}\hat{B}_{R,n+1} - \frac{1}{2}\hat{B}_{R,n}\right)\Delta x \\ Z_{n+2} &= Z_{n+1} + \left(\frac{3}{2}\hat{B}_{Z,n+1} - \frac{1}{2}\hat{B}_{Z,n}\right)\Delta x \\ \phi_{n+2} &= \phi_{n+1} + \left(\frac{3}{2}\hat{B}_{\phi,n+1} - \frac{1}{2}\hat{B}_{\phi,n}\right)\frac{\Delta x}{R_{n+1}}. \end{aligned} \tag{B.6}$$

Whenever the position of intersection at a certain poloidal plane with angle ϕ_{plane} needs to be known, linear interpolation is used between the steps with angles ϕ_{n+1} and

ϕ_n which relate to the position of the plane as $\phi_{n+1} > \phi_{\text{plane}} > \phi_n$. The coordinates on this plane are calculated by:

$$\mathbf{x}_{\text{plane}} = \mathbf{x}_n + (\phi_{\text{plane}} - \phi_n)\frac{\mathbf{x}_{n+1} - \mathbf{x}_n}{\phi_{n+1} - \phi_n}. \tag{B.7}$$

B.1.1 Convergence of fieldline tracer

For an unperturbed magnetic field, the tracer is used around the $q = 2$ surface for 10 toroidal rotations for various step sizes Δx. For a single field line trace, the value of ψ_N is expected to remain constant. The maximum relative difference in the normalized poloidal flux

$$(\Delta\psi_N)_{\max} = \max\left[\frac{\psi_N - \overline{\psi}_N}{\overline{\psi}_N}\right] \tag{B.8}$$

found during such a trace is shown in figure B.1. For values between 1 cm and 10 cm agreement is found with the expected second order scaling. Step sizes of 1 cm are used in this thesis as they show a good trade-off between accuracy and number of steps and thus run time. The plateauing effect can be attributed to the error in other factors such as grid size becoming more important than the error due to the tracer.

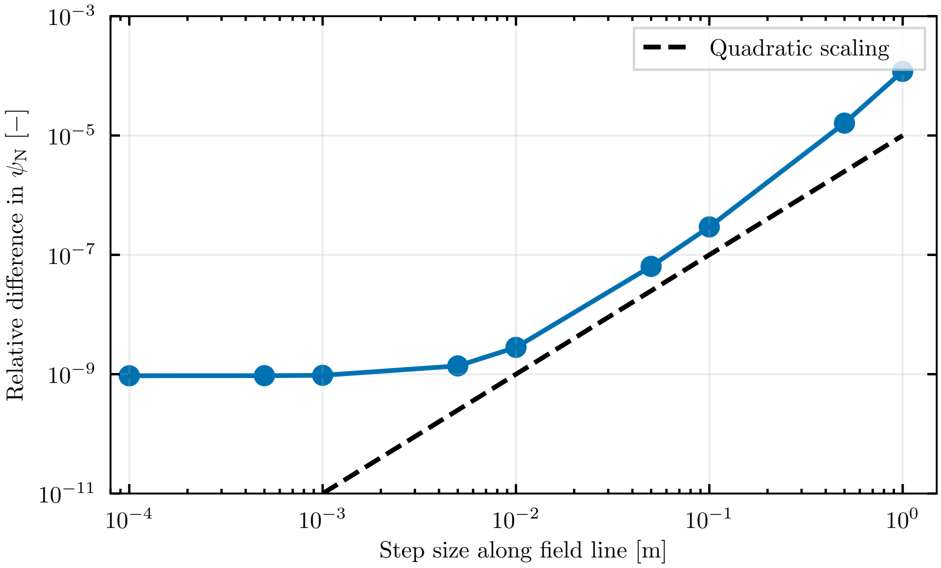

Figure B.1: The maximum relative difference in the normalized poloidal flux, defined in (B.8), shows the expected quadratic scaling, followed by a plateauing effect. There is no need for decreasing the step size beyond 1 cm.

B.2 Locating static points in a poloidal mapping

In an unperturbed ψ-profile a magnetic field line at rational q-surfaces loops back on itself after m toroidal rounds. Magnetic island as a whole share this property, but the field lines on and inside the separatrix do not. Only the X-point and O-point of the islands have the same behavior as the single unperturbed field lines. Moreover, around the X-points of the magnetic islands, the distance between field line crossings in the poloidal plane decreases. This field line stagnation is shown in figure B.2, where the ratio between the magnetic field line components perpendicular and parallel to the poloidal plane are shown around the X-point [45]. The figure shows the existence of a minimum at the X-point, while simultaneously showing the difficulty to exactly locate it, due to the fact that field lines intersect the poloidal plane nearly at a right angle close to the X-point. These observations provided the inspiration to construct a function that gives the distance between the start and ending coordinates of a field line after an integer number of toroidal rotations. Mathematically this is given by

$$F\left(R,Z\right)=\sqrt{\left(R_{\phi}-R_{\phi+2\pi m}\right)^{2}+\left(Z_{\phi}-Z_{\phi+2\pi m}\right)^{2}}, \tag{B.9}$$

for m rotations. The function is shown in figure B.3 in combination with a Poincaré plot of the island at the corresponding time. The function F is smooth over the poloidal plane and has a circular valley in which the X-points and O-points are located. The location of an X-point is estimated using the gradient descent method, extended with a momentum term [77]. This method is not chosen for its efficiency, but rather for its robustness in finding a minimum. Using $\mathbf{r}$ as coordinate in the poloidal plane, new coordinates is found using the iterative scheme

$$\begin{aligned}\mathbf{z}_{n+1}&=\beta\mathbf{z}_{n}+\nabla F(\mathbf{r}_{n})\\ \mathbf{r}_{n+1}&=\mathbf{r}_{n}-\gamma\mathbf{z}_{n+1},\end{aligned} \tag{B.10}$$

in which β indicates the strength of the momentum and γ is a scaling for the step size, which typical value is highly dependent on the function to find a minimum of. For functions that exhibit behavior with a large range of gradients, a single valued γ will either cause overshoots or unreasonably small steps. The addition of momentum allows the solver to retain information of earlier steps and applying it to the current. If similar gradients (mainly directions) are subsequently found, then their effect is enhanced, causing the method to take increasingly large steps downhill. The coordinates visited during a gradient descent run are shown in the bottom of figure B.3. Here can be seen that the number of function evaluations to find the global minimum is over an order of magnitude higher than for finding the circular ring. This is due to the large variation in gradients in and outside the ring. Faster convergence is obtained by increasing β, which causes the radial overshoot, and performing several sequential runs, between which γ is varied.

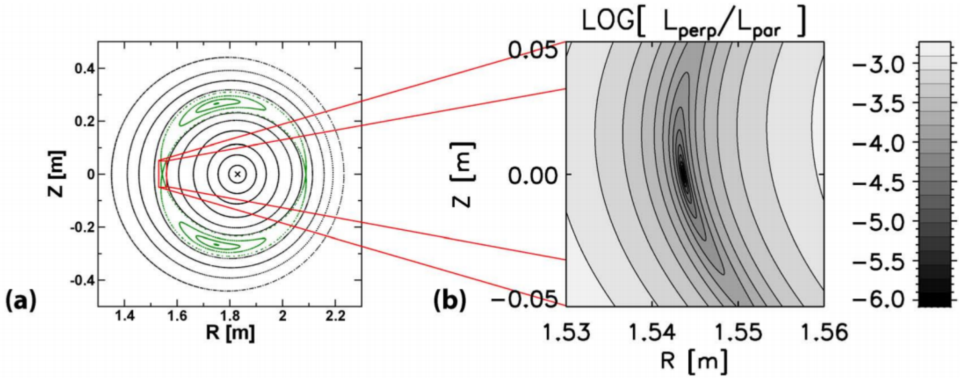

Figure B.2: The difficulty in finding the island X-point shows as the field line components in the poloidal plane L_{perp} decrease rapidly compared to the component in the toroidal direction L_{par}. Adapted from [45].

The function F shows striking resemblance with a classical problem in optimization theory: the Rosenbrock function. This function has a global minimum in a valley that is roughly parabolic, which is generally easy to find. The difficulty lies in finding the global minimum inside this region with small gradients [78]. The Nelder-Mead method is proposed as a better method to be used on problems similar to the Rosenbrock function [79]. For future work it might be beneficial to implement this method as an extra option in the island finding routine as well.

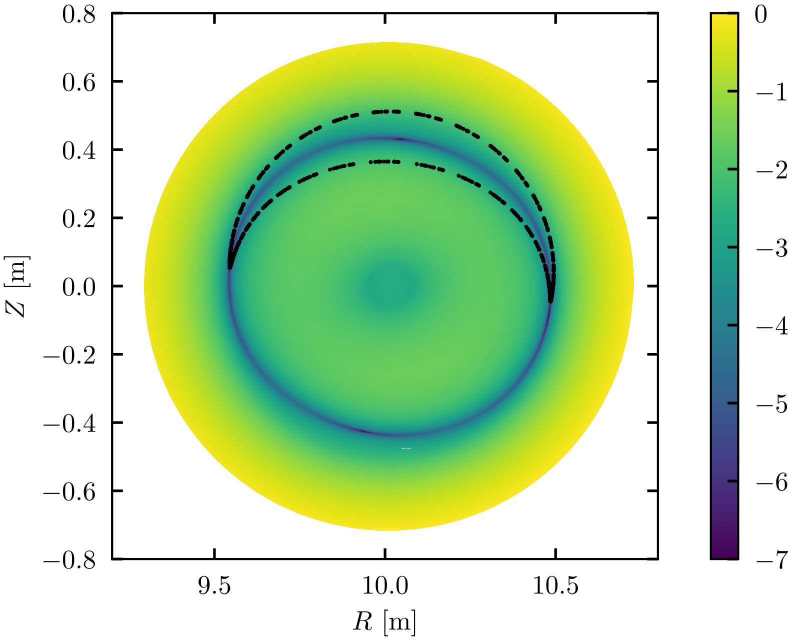

(a) Logscale

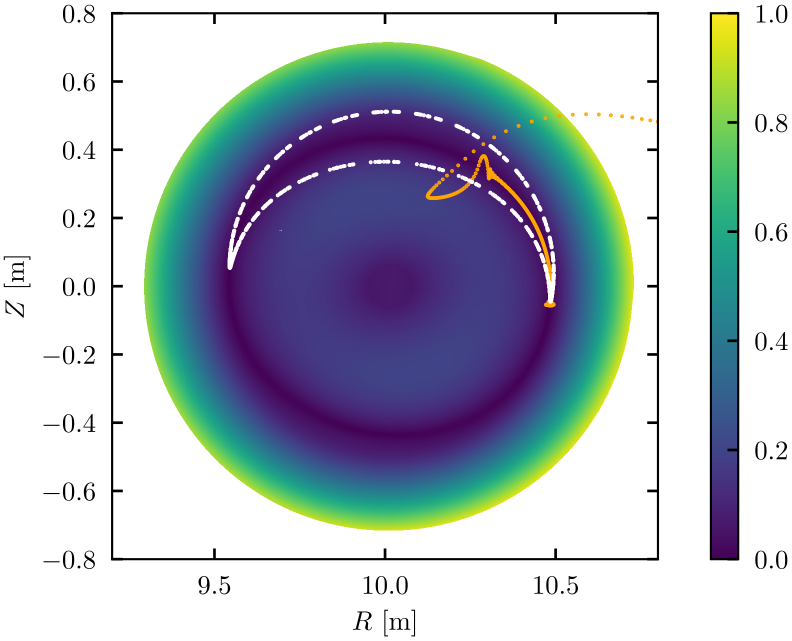

(b) Linear scale

Figure B.3: The function defined in (B.9) is shown for a case with large magnetic islands (Poincaré plots in black and white) on both a logarithmic and linear scale. The top plot is similar to figure B.2. The minima at X- and O-points lie within a circular region that is relatively easy to find. The difficulty lies in finding a global minimum inside this ring, which is apparent from the large number of visited coordinates in the gradient descent method, shown as orange dots.

B.3 Verification of endpoint location

After the gradient descent method has found a minimum within the set tolerance, a confirmation is needed to make sure that the found point is within the separatrix. Only traces of magnetic field lines just within or on the separatrix result in the island structure to become visible in a Poincaré plot. The check makes use of the stagnation around the X-point. An example of the intersections of two series of intersection points is given in figure B.4. Suppose that the red location is found, then the field line will be traced in the forward and backward direction, until the distance between intersections in the poloidal plane is found to increase. These endpoints are shown as white dots. Then the angular distance (in the poloidal plane) of the last two intersection points is determined. If for both the forwards and backwards trace, the angular directions for which stagnation occurs have the same sign, the magnetic field line is inside the separatrix. Oppositely, if the blue location is initially found, stagnation is found once in positive and once in the negative θ direction. This magnetic field line thus lies outside the separatrix of the island.

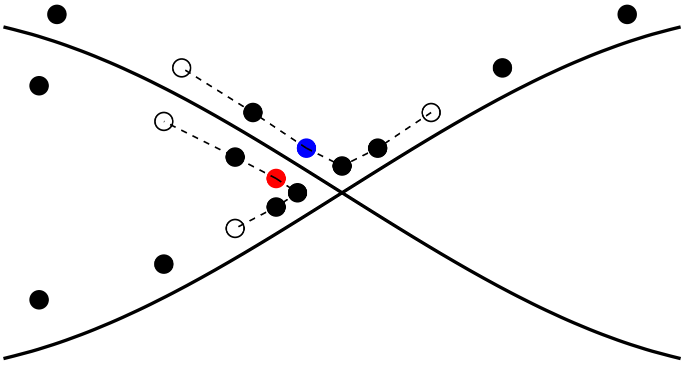

Figure B.4: The separatrix (black line) can be approximately located by the gradient descent method (red and blue dots). Once the distance between intersections (black dots) is found to increase (white dots), the directions in which they move are compared. For the red case, both lines are directed left, while for the blue case two opposing directions are found. In the real island finding routine, the direction (left/right) is replaced by the poloidal angle.

A small step in poloidal direction can be sufficient to cross the separatrix and find coordinates inside the island. This prevents an additional, time-consuming run of the gradient descent. However, the traced magnetic field line will be further away from the separatrix with each poloidal step, as shown in figure B.5. This decreases the maximum island width that can be found. The maximum found island width has a parabolic dependency for small angle sizes, shown in figure B.6. Therefore, the relative error falls to around 0.1% for small step sizes. For total steps of 0.01− 0.5 rad occuring in this thesis, the relative error never exceeds 10%. It will typically remain on the order of a few percent.

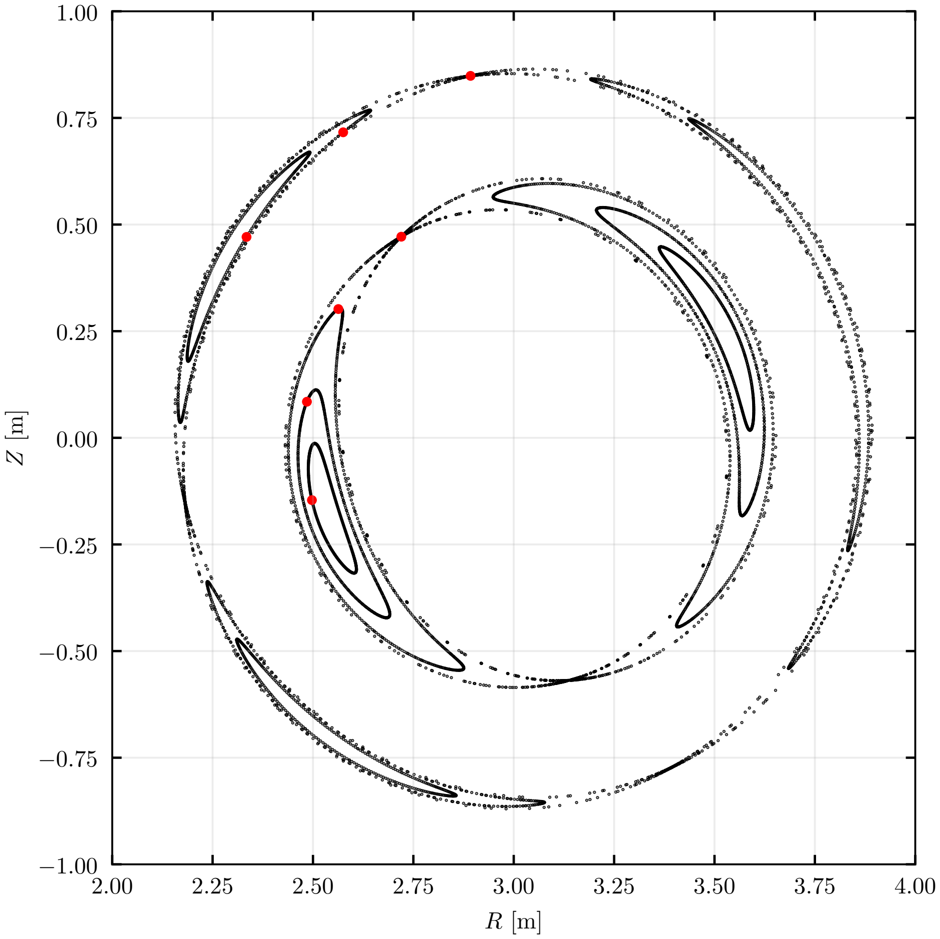

Figure B.5: For both $^2/_1$- and $^3/_1$-islands, taking large poloidal steps away from the X-points still allows for tracing an internal flux structure. The width of these flux structures can still be used to estimate the actual island width, as shown in figure B.6.

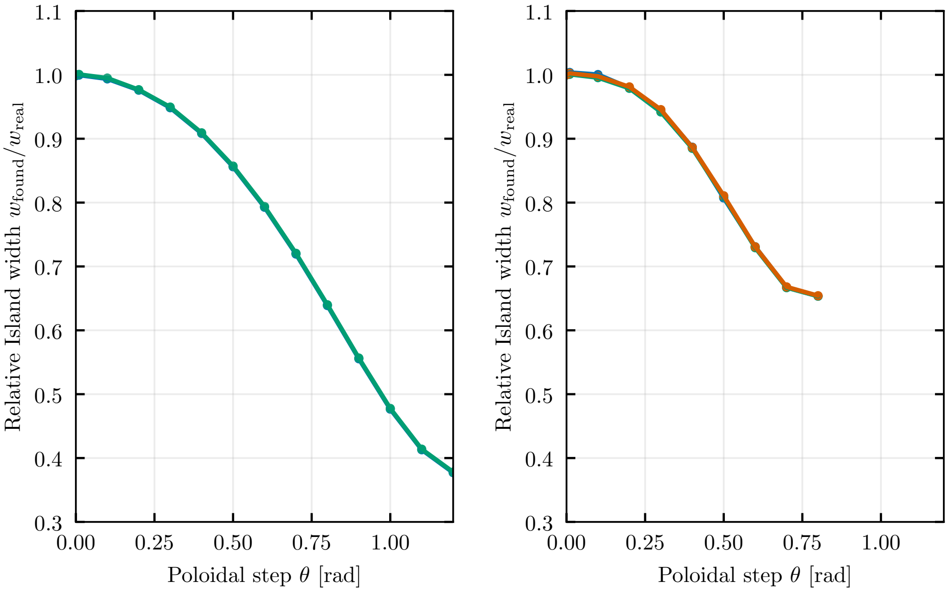

(a) Width of $^2/_1$ islands

(b) Width of $^3/_1$ islands

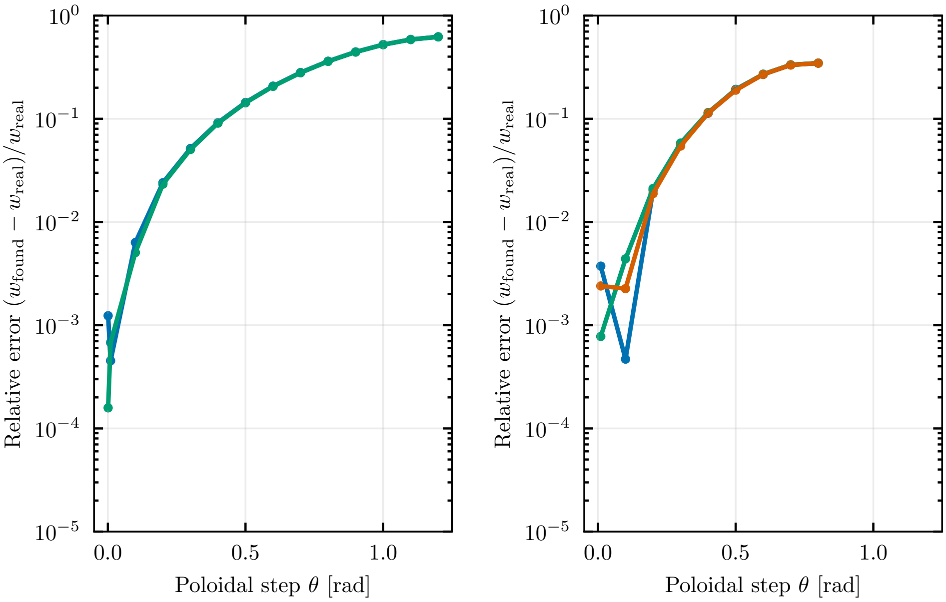

(c) Relative error of $^2/_1$ islands

(d) Relative error of $^3/_1$ islands

Figure B.6: The relative island width (top) and relative errors in these widths (bottom) are plot for the $^2/_1$- and $^3/_1$-islands. The error decreases to the percent range as poloidal steps smaller than 0.5 rad are taken.

B.4 Obtaining the width from the Poincaré plot

To fairly compare the found widths of the magnetic islands when they are found with different orientations in the poloidal plane, an additional mapping is necessary. Instead of locating the spatial width, the maximum and minimum encountered values of ψ_{N} are stored. From `JOREK` the relation between ψ_{N} and r/a at the midplane is obtained, by which the island width can be projected on this plane. The added benefit is that this will work regardless of the shape of the poloidal plane. The spatial width of islands in devices with elongated poloidal planes changes with respect to the poloidal angle. The conversion to the midplane width removes this effect.

B.5 Overview of options

Table B.1: User defined settings in the island finding routine

Option	Typical value	Description
m	2	Number of toroidal rotations island
n	1	Number of poloidal rotations island
Rstart	3.5	Start coordinate of gradient descent
Zstart	0.5	Start coordinate of gradient descent
stepsize	1×10^{-2}	Stepsize for field line tracing
gamma(1)	1×10^{-3}	γ for R-coordinate
gamma(2)	5×10^{-2}	γ for Z-coordinate
momentum	0.85	Strength of momentum term β
tolerance	1×10^{-4}	Tolerance for termination gradient descent method
max_iters	100	Number of iterations in gradient descent method
repetitions	4	Number of times gradient descent method is repeated
gd_stepfactor	20	Multiplication factor for γ between repetitions
thetastep	$[10^{-2} - 10^{-1}]$	Stepsize if endpoint is outside separatrix
datapoints	1000	Number of datapoints in Poincaré plot
filemin	1000	First `JOREK` file to find islands for
filemax	2000	Last `JOREK` file to find islands for
increment	10	Increment in loop over `JOREK` files
heatmap	`.true./.false.`	Option to generate heatmap like B.3
hmr	200	Number of points in radial direction of heatmap
hmth	200	Number of points in poloidal direction of heatmap
hmrmin	0.0	Minimum radial bound for heatmap
hmrmax	1.0	Maximum radial bound for heatmap
hmthmin	0	Minimum angular bound for heatmap
hmthmax	0	Maximum angular bound for heatmap

C. JOREK Normalization

Quantity name	SI units	expressed in `JOREK` quantities
Major radius	R [m]	R
Vertical coordinate	Z [m]	Z
Toroidal angle	ϕ [rad]	ϕ
Time	t [s]	t
Magnetic field vector	$\mathbf{B}$ [T]	$\mathbf{B}$
Electric field vector	$\mathbf{E}$ [Vm^{-1}]	$\mathbf{E}/\sqrt{\mu_0\rho_0}$
Poloidal magnetic flux	Ψ [Tm^{-2}]	Ψ
Velocity vector	$\mathbf{v}$ [ms^{-1}]	$\mathbf{v}/\sqrt{\mu_0\rho_0}$
Parallel velocity component	$v_{\parallel}$ [ms^{-1}]	$\mathbf{v}\cdot\mathbf{B}/\sqrt{\mu_0\rho_0}$
Toroidal vorticity	ω_ϕ [m^{-1}s^{-1}]	$\omega/\sqrt{\mu_0\rho_0}$
Toroidal current density	j_ϕ [Am^{-2}]	$-j/(R\mu_0)$
Particle number density	n [m^{-3}]	ρn_0
Particle mass density	ρ [kgm^{-3}]	$\rho\rho_0$
Impurity number density	n_{imp} [m^{-3}]	$\rho_{\mathrm{imp}} n_0 {}^{m_{\mathrm{D}}}/{}_{m_{\mathrm{imp}}}$
Impurity mass density	ρ_{imp} [kgm^{-3}]	$\rho_{\mathrm{imp}}\rho_0$
Total temperature (electron + ion)	T [eV]	$T/\left(e\mu_0 n_0\right)$
Plasma pressure	p [Nm^{-2}]	$\rho T/mu_0$
Resistivity	η [Ωm]	$\eta\sqrt{\mu_0/\rho_0}$
Dynamic viscosity	μ [ρ_0/μ_0]	$\mu\sqrt{\rho_0/\mu_0}$
Particle diffusivity ($\parallel$ and $\perp$)	D [m^{2}s^{-1}]	$D/\sqrt{\mu_0\rho_0}$
Thermal conductivity ($\parallel$ and $\perp$)	K [kgm^{-1}s^{-1}]	$K\sqrt{\rho_0\mu_0}$
Heat source	S_{H} [Wm^{-3}]	$\frac{3}{2}S_{\mathrm{H}}/\sqrt{\mu_0^3/\rho_0}$
Ionisation energy	E_{ion} [J]	$E_{\mathrm{ion}}/\left({}^2/{}_3\mu_0 n_0\right)$
Radiation rate	L_{rad} [Wm^3]	$L_{\mathrm{rad}}/\left({}^2/{}_3\mu_0\sqrt{\mu_0\rho_0}\,n_0^2\,{}^{m_{\mathrm{D}}}/{}_{m_{\mathrm{imp}}}\right)$
Radiation power density	P_{rad} [Wm^{-3}]	$P_{\mathrm{rad}}/\left({}^2/{}_3\mu_0\sqrt{\mu_0\rho_0}\right)$
With definitions		
	n_0 [m^{-3}]	`central_density` $\cdot 10^{20}$
	ρ_0 [kgm^{-3}]	`central_mass` $\cdot\, n_0 m_{\mathrm{proton}}$